

FACULTY
OF MATHEMATICS
AND PHYSICS
Charles University

MASTER THESIS

Bc. Ondřej Kureš

Analysis of the ocean-induced magnetic field and its sensitivity to ocean models

Department of Geophysics

Supervisor of the master thesis: doc. RNDr. Jakub Velímský, Ph.D.
Study programme: Geophysics and Planetary Science

Prague 2026

I declare that I carried out this master thesis on my own, and only with the cited sources, literature and other professional sources. I understand that my work relates to the rights and obligations under the Act No. 121/2000 Sb., the Copyright Act, as amended, in particular the fact that the Charles University has the right to conclude a license agreement on the use of this work as a school work pursuant to Section 60 subsection 1 of the Copyright Act.

In ..... date ....

Author's signature

This research was supported by the European Space Agency (ESA), Contract No. 4000143627/24/I- EB Swarm for Ocean Dynamics, part of the ESA Solid Earth Magnetic Science Cluster, EO for Society programme.

I would like to start by thanking my supervisor Jakub Velímský, for his guidance, patience, and for all the given opportunities. I never thought I would visit so many interesting places and meet so many unique people.

My next thanks go to my colleagues and friends at the Department of Geophysics for providing the best environment I could have hoped for. Also I would like to thank the emotional support group MŠ KG MFF UK.

And finally, thank you for everything, **my dearest**.

Title: Analysis of the ocean-induced magnetic field and its sensitivity to ocean models

Author: Bc. Ondřej Kureš

Department: Department of Geophysics

Supervisor: doc. RNDr. Jakub Velímský, Ph.D., Department of Geophysics

Abstract: As the oceans play a substantial role in the dynamics of Earth's climate, understanding their physical processes is of great importance. The crucial role in the study of oceans is played by observations, where satellite-based observations are becoming more and more significant. However, the most of the satellite observations are focused on the ocean surface or its shallowest parts. The ocean-induced magnetic field (OIMF), which is generated by interaction of ocean currents with Earth's ambient magnetic field, can in principle provide constraints on the ocean dynamics in the entire depth column. It is primarily governed by the 4-D distribution of ocean flow velocity, and depends only on the ocean temperature and salinity, which determine the seawater electrical conductivity. This thesis focuses on two particular OIMF related topics, which were addressed within the ESA funded Swarm for Ocean Dynamics project. First, it analyses the results of OIMF numerical simulations for different input models by application of the Principal Component Analysis in order to detect and compare the dominant spatio-temporal modes of OIMF. This is followed by the derivation of adjoint method to the electromagnetic induction problem with internal motional forcing, which allows to obtain 4-D adjoint sensitivity kernels. These kernels provide better insight into the problem and mark the first major step towards future data assimilation into ocean models.

Keywords: ocean-induced magnetic field, electromagnetic induction, principal component analysis, adjoint sensitivity kernels

Contents

1 Introduction **7**
- 1.1 Motivation . . . 7
- 1.2 Role of the ocean motion . . . 8
- 1.3 OIMF in global observations of geomagnetic field . . . 9

2 Numerical simulations of OIMF **12**
- 2.1 Forward problem . . . 12
- 2.2 Description of models . . . 13
  - 2.2.1 Ocean Models . . . 13
  - 2.2.2 Electrical conductivity . . . 14
  - 2.2.3 Main field . . . 14
  - 2.2.4 Numerical parameters . . . 15
  - 2.2.5 Canonical run . . . 15

3 Principal Component Analysis **16**
- 3.1 Overview . . . 16
- 3.2 Definition . . . 16
  - 3.2.1 Data matrix . . . 17
  - 3.2.2 Definition of PCA . . . 17
  - 3.2.3 Application of Singular Value Decomposition in PCA . . . 18
  - 3.2.4 Application to OIMF . . . 18
- 3.3 Analysis of different OIMF models . . . 20
  - 3.3.1 Spatio-temporal filtering . . . 20
  - 3.3.2 Sensitivity to ocean models . . . 28
  - 3.3.3 Sensitivity to main field models . . . 28
  - 3.3.4 Lateral resolution . . . 31
  - 3.3.5 Transient switch-on effect . . . 35
  - 3.3.6 Upper-mantle conductivity . . . 35

4 Adjoint Method **39**
- 4.1 Inverse problem . . . 41
- 4.2 Adjoint problem . . . 43
- 4.3 Examples of sensitivity kernels . . . 44
  - 4.3.1 Electrical resistivity . . . 45
  - 4.3.2 Ocean velocities . . . 45

Conclusion **56**

Bibliography **57**

List of Figures **61**

List of Tables **63**

List of Abbreviations **64**

A Attachments **65**
A.1 Spherical harmonic functions 65
A.2 Adjoint problem 66

1 Introduction

1.1 Motivation

The ocean dynamics is one of the most important factors that govern the climate of the Earth. It is therefore not surprising that there is a great effort to monitor the state of the ocean and to understand the physical processes in it (Siedler et al., 2013). One way of monitoring is through in-situ observations. The coastal stations, buoys, autonomous submarines, ships, aerial surveys, or even direct sampling are used to measure flow velocity, temperature, salinity, and other ocean properties. The problem is that the oceans cover a large area and reach considerable depths, so we need a large number of measuring instruments to achieve the necessary spatial coverage. If we wanted to cover large areas through, for example, submarine or ship surveys, we would run into the problem of irregular temporal and spatial coverage. Compensating for these shortcomings is financially and logistically demanding. Satellite observations are therefore becoming increasingly important. Unlike in-situ methods, they offer near-global coverage in days, making them indispensable for monitoring long-term and large-scale ocean dynamics. They also offer us a wide range of data, to name a few: sea surface salinity (SSS, example shown in Figure 1.1), sea surface temperature (SST), sea surface height (SSH), or even information on the concentration of chlorophyll through the colouration of the sea surface (Von Schuckmann et al., 2016). Unfortunately, most of the satellite observations of global oceans are sensitive only to its shallowest part. Thus, one can ask if there is a satellite-observable physical field that is sensitive to the state of the deep ocean.

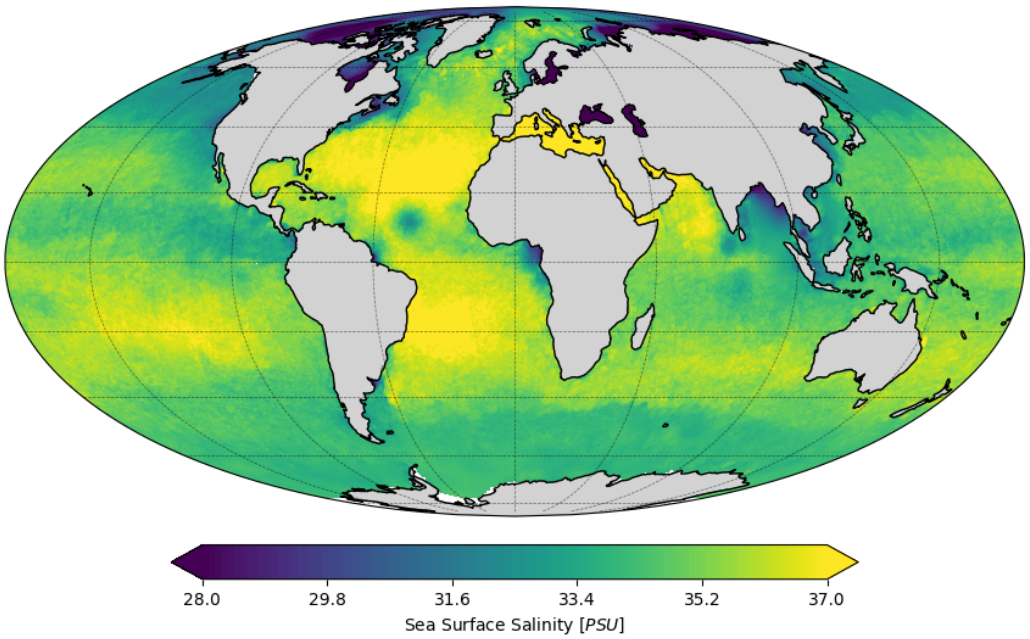


Figure 1.1 Snapshot of Sea Surface Salinity from 15-12-2024. Generated using EU Copernicus Marine Service Information; 10.48670/moi-00051

The ocean is an electrically conductive medium due to the presence of dissoci-

ated salts in the water, the average conductivity is around 3.2 $\mathrm{S\,m^{-1}}$ (Apel, 2013). As a conducting medium moves through an ambient magnetic field, the Lorentz force acts on the charge carriers, which subsequently generate an electric current in the medium in the direction perpendicular both to the flow and the ambient magnetic field. When an electric current begins to flow through a conductor, it generates a magnetic field in turn. We call this process motional induction and denote the resulting magnetic field as the *Ocean-Induced Magnetic Field* (OIMF). It should be taken into account that the OIMF is accompanied by phenomena that influence the overall temporal variations and spatial structures of the OIMF (Velímský et al., 2019; Šachl et al., 2019). One of these is inductive coupling between oceans, sediments, and mantle, which exists due to the electric currents that are induced in the electrically conductive material by the temporally varying magnetic fields. Another phenomenon is galvanic coupling, which exists due to the spatially varying electrical conductivity.

1.2 Role of the ocean motion

The motional induction process is primarily governed by the very existence of ocean flows, their amplitude, and spatio-temporal climatology. We distinguish two general categories of ocean movements: tidal flows and general circulation. The first is a result of the periodic gravitational pull exerted by the Sun and the Moon on the Earth. Due to the lunisolar tidal forcing being nearly independent on the ocean depth (which is negligible with respect to Earth-Sun or Earth-Moon distance), the entire water column moves in unison, and there are almost no vertical variations. Tidal flows are usually mathematically described by two-dimensional shallow water equations in barotropic approximation and solved in the frequency domain for discrete set of lunisolar tidal constituents (frequencies). However, such an approach does not consider non-linearities that can be present in ocean dynamics (e.g. interactions between tides and continental shelves), which leads to generation of compound tides (Einšpigel and Martinec, 2017). Similarly, the OIMF generated by the lunisolar tides (often marked as Tidal Induced Magnetic field or TIMF) is prominent at the same frequencies, which are used both in numerical modelling of the electromagnetic induction (EMI) equation in the frequency domain, and as a prior information allowing the isolation of TIMF signals from observatory and satellite magnetic measurements (from initial processing Tyler et al. (2003) to the latest models Grayver et al. (2024)). In this work, we focus on the second category of ocean flows. By comparison, general circulation has more mechanisms in play than their tidal counterpart. It is driven by winds and buoyancy related mechanisms, with additional effects coming from sea surface processes, the Coriolis force, or the input of freshwater. All this gives rise to structures that have varying horizontal scales in space (from metres up to thousands of kilometres) and time (from days up to centuries).

Circulation in the upper parts of the ocean (up to a depth of hundreds of metres) is greatly influenced by winds and surface processes. Mesoscale eddies and more dominant large-scale gyres form in this part of the ocean. The deeper parts of the ocean are dominated by thermohaline circulation, also known as meridional overturning current (MOC). The density of the ocean is controlled by temperature and salinity. The density differences that arise from this relationship are what

drives the thermohaline circulation. As suggested, this type of circulation plays a crucial role in the transport of water. The hotter ocean water travels pole-ward, where it starts cooling down until it freezes. Frozen water leaves salt behind in non-frozen water, which in turn becomes denser. Colder, denser water then travels back towards the equator. This process results in global-scale circulation, called a *Global Conveyor Belt* (see Figure 1.2 for a simplified scheme). Part of this global system are the Antarctic Circumpolar Current (ACC) or Atlantic Meridional Overturning Circulation (AMOC).

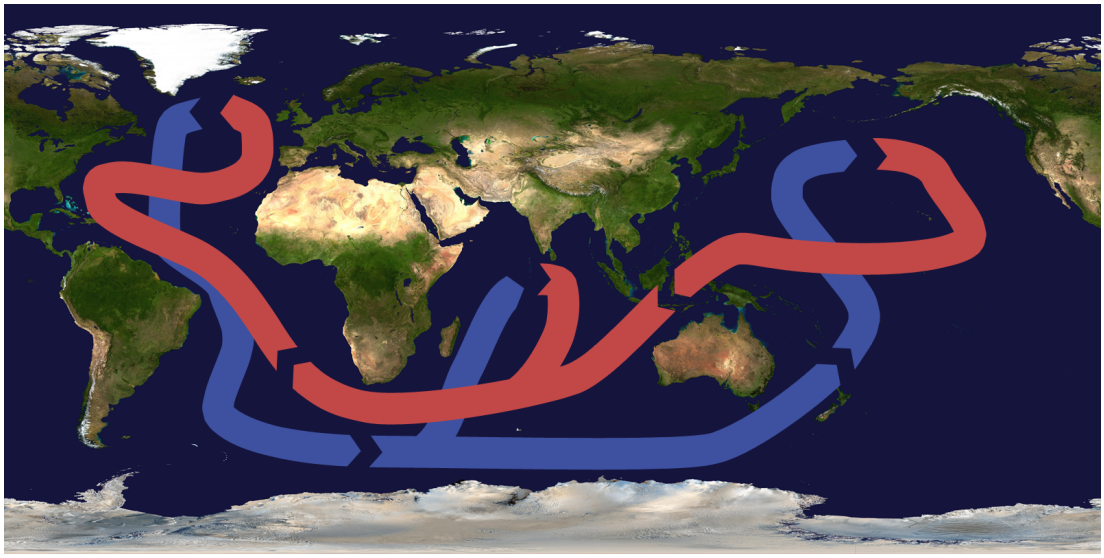


Figure 1.2 A simple scheme of the Global Conveyor Belt. Red indicates warm water and blue indicates cold water. Figure by Brisbane, CC BY-SA 3.0, via Wikimedia Commons.

The basic equations for modelling the global ocean circulation are the Navier-Stokes equations in combination with conservation equations for salinity and temperature (Madec et al., 2026). The Navier-Stokes equations are used in thin-shell approximation in combination with the Boussinesq approximation and assumption of hydrostatic pressure. The Coriolis force is also assumed, but in the most basic form, although in most models additional terms can be added. Small scale features, like vorticity, are added through parameterisation. For the equation of state, the density is dependent on pressure, salinity, and temperature. For practical applications, the numerical models are combined with observations using data assimilation methods (Martin et al., 2024). The most used data are surface observations of the physical processes (e.g. SSS, SST, SSH), although processes related to the biosphere or cryosphere can be incorporated too in modern variants. Assimilation is done using the 3-D Var or 4-D Var methodology.

1.3 OIMF in global observations of geomagnetic field

The geomagnetic field observable at or above the Earth's surface is generated by several different physical processes in the Earth's interior and magnetosphere,

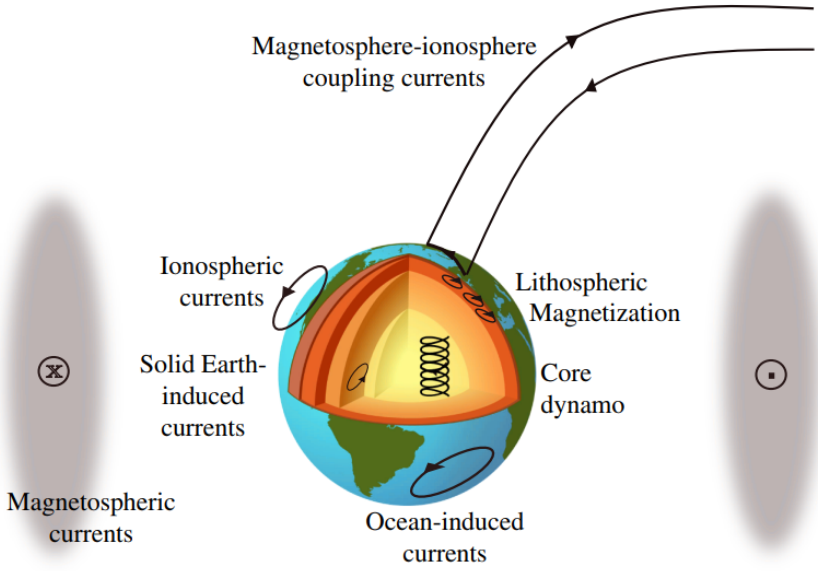


Figure 1.3 A simplified, not to scale, cartoon depicting major near-Earth electrical current systems that contribute to Earth's magnetic field. Taken from Finlay et al. (2024).

including ionosphere (Finlay et al., 2024). An overview is illustrated in Figure 1.3 and summarised in Table 1.1.

By far the strongest magnetic field is the main field generated by the core dynamo. It is primarily dipolar, but large-scale features still overshadow other fields. Due to distance from the source region, amplitudes of small-scale features at the core-mantle boundary are strongly dampened in the observations on the surface or at the low orbit. Also, it is rather slow phenomenon, as temporal variations occur on timescales from years to millennia and beyond. In upper layers of the Earth (crust and lithosphere), where temperature drops below Curie temperature, materials can retain their magnetisation and are therefore the source of the so called crustal (lithospheric) magnetic field. Although this field is weaker than the one produced in the core, the crustal magnetic field starts to overshadow the core field on a regional scale. Temporal variations of the crustal magnetic field are negligible, and therefore it can be considered static. Similarly to the crustal field, OIMF starts to dominate the core field on a regional scale. However, it has the weakest signal and the only way to distinguish it from crustal field is by temporal variations ranging from months to years. The ionospheric field originates in parts of the atmosphere where gases are ionised by solar radiation. Its spatial patterns vary greatly with the latitude, with day-side to night-side contrast. The very important feature of this field is its high temporal variability, ranging from minutes to days, with noticeable seasonal variations. The magnetospheric field is created by the interactions of the core field with the solar winds. In terms of the spatial patterns it is a large scale field, dominated by the dipolar structure corresponding to the equatorial ring current. As temporal variations are guided by solar activity, there is an extreme difference between quiet periods and events of the geomagnetic storms, during which the magnetospheric field reaches its peak and its axial symmetry is significantly weakened.

The existence of TIMF on distinct short periods can be utilised in the noise

Source	**Amplitude** [nT]	**Spatial scales** [km]	**Time scales**
Core	$\approx 10^4$	Large to Global ($> 10^3$)	Years to Millennia and beyond
Crust	$\approx 10^1$	Small to Regional ($\approx 10^2$ to 10^3)	Static
Oceans	≈ 1	Small to Regional ($\approx 10^2$ to 10^3)	Months to Years
Ionosphere	$\approx 10^1$ to 10^2	Large ($\approx 10^3$ to 10^4)	Minutes to Seasons
Magnetosphere	$\approx 10^1$ to 10^2 (storms $\geq 10^2$)	Global ($> 10^4$)	Hours to Weeks

Table 1.1 Overview of characteristics of various geomagnetic fields.

reduction/frequency amplification process, which is very similar to the signal stacking. As the general circulation OIMF signal lacks specific frequencies, detection is much harder. Although isolating a subtle signal from the substantial background presents a difficult task, it is not impossible with the proper methodology, based on thorough analysis of the magnetic fields.

The ESA funded project *Swarm for Ocean Dynamics* (SfOD) was established with the main goal of retrieving OIMF from 10 years of collected data from the Swarm mission. With the newly created methodology, SfOD was partially successful in extracting OIMF from satellite data, even though this signal is currently highly limited in both time and space, due to insufficient spatio-temporal coverage and restrictions imposed by other magnetic fields (Finlay et al., 2024; Finlay et al., 2026, submitted) The former problem can be solved in the future by including other satellite missions such as MSS-1, CHAMP, or planned NanoMagSat. The solution of the latter problem requires better models of the various magnetic fields of the Earth.

This thesis is based on my contributions to the SfOD project. Chapter 2 contains a concise description of the forward EMI problem, following the methodology of Velímský (2025), and provides an overview of the OIMF simulations carried out within the project framework; they are described in detail by Ucekajová (2025). In Chapter 3 I discuss my application of the Principal Component Analysis (PCA) method to simulated OIMF. It provides the dominant spatial and temporal modes of OIMF. The principal modes have two basic uses. They allow to analyse consistent spatio-temporal features in OIMF across a selection of ocean models, as discussed in the following pages. Moreover, they can be used as a reduced model-space base in attempts to isolate the OIMF signal from satellite magnetic measurements (see an initial application by Grüne, 2026). In Chapter 4 I address the key question of the OIMF ability to provide useful constraints to ocean models. This topic has been recently approached by Trossman et al. (2024), who developed a synthetic assimilation scheme of OIMF into the ECCO family of ocean models via depth-integrated conductivity (conductance) and depth-integrated conductivity-weighted velocity. Here, I focus instead on the development and testing of the adjoint sensitivity approach, which aims to future 4-D Var assimilations of OIMF into the ocean models.

2 Numerical simulations of OIMF

In this Chapter, I introduce the EMI equation for numerical simulations of OIMF, and give a concise overview of individual simulations obtained by my colleagues in the SfOD project. Details on the modelling of the forward problem can be found in Velímský (2025). An in depth description and analysis of parameters used in simulations and their outputs are provided in Ucekajová (2025).

2.1 Forward problem

The leading equation of these simulations is the EMI equation with internal forcing,

$$\frac{\partial \mathbf{B}}{\partial t} + \frac{1}{\mu_0} \nabla \times \left(\frac{1}{\sigma} \nabla \times \mathbf{B} \right) = \nabla \times (\mathbf{v} \times \mathbf{B}_C), \tag{2.1}$$

where $\mathbf{B}(\mathbf{r}, t)$ is the OIMF, $\mu_0 = 4\pi \times 10^{-7}$ H m^{-1} is the magnetic permeability, $\sigma = \sigma(\mathbf{r}, t)$ is the electrical conductivity of oceans and solid Earth, $\mathbf{v} = \mathbf{v}(\mathbf{r}, t)$ is the ocean flow velocity, and $\mathbf{B}_C = \mathbf{B}_C(\mathbf{r}, t)$ is the ambient magnetic field generated by the dynamo process in the Earth's core.

The chosen initial condition must satisfy Gauss's law,

$$\nabla \cdot \mathbf{B} = 0. \tag{2.2}$$

The EMI equation (2.1) is solved in a spherical domain $\mathbf{r} = (r, \vartheta, \varphi)$ of radius a=6371.2 km. It is surrounded by an insulating atmosphere, where the OIMF can be described by a scalar magnetic potential $U(\mathbf{r}, t)$. This allows us to define the boundary condition as

$$\mathbf{B} = -\nabla U \text{ on } r = a, \tag{2.3}$$

$$\Delta U = 0 \text{ for } r \geq a. \tag{2.4}$$

The solution of 2.4 expressed by a spherical harmonic series,

$$U(\mathbf{r}, t) = a \sum_{j=1}^{\infty} \sum_{m=-j}^{j} \left[\left(\frac{a}{r} \right)^{j+1} G_{jm}^{(i)}(t) + \left(\frac{r}{a} \right)^{j} G_{jm}^{(e)}(t) \right] Y_{jm}(\Omega), \tag{2.5}$$

where $G_{jm}^{(i)}(t), G_{jm}^{(e)}(t)$ are the Gauss coefficients corresponding to the internal and external fields, and $Y_{jm}(\Omega)$ are the fully normalised scalar spherical harmonic functions (Varshalovich, 1989; some details in Appendix A.1). In the forward model of OIMF, external fields are assumed to be non-existent. This leads to a decreasing potential

$$U = \mathcal{O}(r^{-2}) \text{ as } r \to \infty, \tag{2.6}$$

which in turn function as a boundary condition for Equation 2.5 that is satisfied by setting $G_{jm}^{(e)}(t) = 0$ for all j, m.

The numerical solver used for the simulations is **elmgTD_mpi**. It is a time-domain solver, where the magnetic field is spatially discretised using piecewise-linear finite elements in the radial direction, and vector spherical harmonic functions in the lateral direction. The spherical grid is divided into layers with differing thicknesses, with higher radial resolution reserved for layers that correspond to the oceans increasing layer thickness with depth. The longitudinal direction is resolved by an equidistant grid, and the latitudinal grid conforms to the roots of Gauss-Legendre polynomials for efficient and accurate quadrature approximation of integrals. Time integration follows the Crank-Nicholson scheme with the uniform time step.

2.2 Description of models

A total of 12 models of the OIMF were computed, each with different model parameters (Table 2.1) and numerical parameters (Table 2.2). The model parameters are categorised into 3 groups: main field, ocean velocities, and electrical conductivity. The electrical conductivity models are divided into seawater, sediments, and mantle.

RUN	Ocean Model	Mantle	Main Field
1	CMEMS mean	MIN_1DM_501	**IGRF13 static**
2	**ECCO2**	MIN_1DM_501	IGRF13
3	**CMEMS-cglo**	MIN_1DM_501	IGRF13
4	**CMEMS-glor**	MIN_1DM_501	IGRF13
5	**CMEMS-oras**	MIN_1DM_501	IGRF13
6	CMEMS mean	MIN_1DM_501	IGRF13
7	CMEMS mean	MIN_1DM_501	**CHAOS-7.18**
8	CMEMS mean	MIN_1DM_501	IGRF13
9	CMEMS mean	MIN_1DM_501	IGRF13
10	CMEMS mean **+SSS-CCI**	MIN_1DM_501	IGRF13
11	CMEMS mean	MIN_1DM_501 **+ WINTERC-emax**	IGRF13
12	**ECCOv4r4**	MIN_1DM_501	IGRF13

Table 2.1 Run configurations: Ocean Model, Sediments, Mantle, and Main Field. All model parameteres are described in their respective subsections.

2.2.1 Ocean Models

One set of models comes from the Copernicus Marine Environment Monitoring Service (CMEMS), where the modelling is based on Nucleus for European Modelling of the Ocean (NEMO; Madec et al., 2026). Specifically, CMEMS Global Ocean Reanalyses (CMEMS., 2024; Desportes et al., 2023) are used, which describe the physical state of the ocean created with numerical ocean simulations. In order to be as close as possible to the observations of the real ocean, these

models are constrained with data assimilation of satellite and in situ observations data. Part of the reanalyses are four models: GLORYS2V4 from Mercator Ocean (Fr); ORAS5 from ECMWF; GloSea5 from Met Office (UK); and C-GLORSv7 from CMCC (It). All of these models are then processed into one ensemble mean, which is called the CMEMS mean. In addition to the ocean model CMEMS mean, three other models are used, each based on the variant used in the ensemble mean: CMEMS-cglo (Storto et al., 2016), CMEMS-glor (Lellouche et al., 2013) and CMEMS-oras (Zuo et al., 2017). All CMEMS models have a time span from 1993.0 to 2023.0 with 1 day time step.

The second set of models comes from the Estimating the Circulation and Climate of the Ocean (ECCO), where two models are used. First, ECCO2 (Menemenlis et al., 2008) estimates the state of the ocean using Green's function approach (Menemenlis et al., 2005) and is constrained by data from various satellite missions (e.g., GRACE or TOPEX/Poseidon). Second, ECCOv4r4 (Forget et al., 2015) uses a more traditional 4-D Var methodology for data assimilation. ECCO2 has a time span of 1992.0 to 2025.0 and ECCOv4r4 has a time span of only 1992.0 to 2018.0, both with a time step of 1 day. Due to only partial overlap of ECCOv4r4 with the Swarm satellite mission, its use in the comparisons is limited.

2.2.2 Electrical conductivity

Electrical conductivity in oceans is determined by 4-D temperature and salinity climatologies $\sigma(\mathbf{r}, t) = \sigma(T(\mathbf{r}, t), S(\mathbf{r}, t))$. Both fields are included in the ocean models, and the 4-D electrical conductivity model, consistent with the ocean model, can be derived by using the thermodynamic equation of water, in particular the GSW implementation of TEOS-10 (Ioc et al., 2010; Millero et al., 2008; Millero, 2010).

In one simulation, an alternative model of seawater salinity is used, The ESA Sea Surface Salinity Climate Change Initiative (SSS-CCI) (Boutin et al., 2024), which describes the first upper 5 metres of the global ocean. Note that this introduces a minor inconsistency between the conductivity and velocity inputs into the modelling.

The 3-D model of electrical conductivity of seafloor sediments is obtained from a compaction and thermal gradient model constrained by real observations (Grayver, 2021) and is used consistently across all runs.

The 1-D conductivity model of the mantle MIN_1DM_0501 is constrained by the joint inversion of the tidal and magnetosphere-driven induction responses obtained from the Swarm data (Grayver et al., 2017). In one simulation, it is replaced in the upper mantle by a 3-D conductivity model WINTERC-e (Martinec et al., 2021), which is in term derived from the thermochemical model WINTERC-G (Fullea et al., 2021), constrained by independent geophysical datasets.

2.2.3 Main field

The main field is represented by two models: the 13th generation International Geomagnetic Reference Field (IGRF13; Alken et al., 2021) and CHAOS-7.18 (Finlay et al., 2020).

IGRF13 is based on observations from various sources (satellite mission, geomagnetic observatories, etc.) and spans from 1900 to 2020. It is described by a set of spherical harmonic coefficients up to a degree 13, with secular variations up to a degree 8 (only 2020.0 - 2025.0) parameterized by piecewise-linear temporal base. In the modelling setup, both variants, with and without secular variations, are used.

CHAOS-7.18 is based on the satellite missions Swarm, CryoSat-2, CHAMP, SAC-C, and Ørsted and spans from 1999 to 2020. It is also described by a set of spherical harmonic coefficients up to a degree 20. Temporal parameterisation is provided by the 6th-order B-splines.

2.2.4 Numerical parameters

To complete the description of forward simulation, numerical parameters of individual runs are shown in Table 2.2. Here, $\mathbf{N}_\vartheta$ and $\mathbf{N}_\varphi$ are the numbers of grid points in the latitudinal and longitudinal directions, $\mathbf{j_{max}}$ is the spherical-harmonic truncation degree of simulation. The model layers are ordered from bottom to top, with $\mathbf{k_{max}}$ representing the total number of layers, $\mathbf{k_{max1d}}$ are the layers representing spherically symmetric conductivity of the core and mantle, while the layers above it span the heterogeneous sediment and ocean layers, and, in case of run 11, also the uppermost mantle. The index $\mathbf{k_{maxl}}$ then denotes the lowermost ocean layer where internal forcing is present. **dt** is the time step of the time integration scheme, set to 1 day in all runs.

RUN	$\mathbf{N}_\vartheta$	$\mathbf{N}_\varphi$	$\mathbf{j_{max}}$	$\mathbf{k_{max}}$	$\mathbf{k_{maxl}}$	$\mathbf{k_{max1d}}$	**time span**
1	360	720	240	177	103	52	2013.0–2023.0
2	360	720	240	**125**	**76**	52	2013.0–2024.0
3	360	720	240	177	103	52	2013.0–2023.0
4	360	720	240	177	103	52	2013.0–2023.0
5	360	720	240	177	103	52	2013.0–2023.0
6	360	720	240	177	103	52	2013.0–2023.0
7	360	720	240	177	103	52	2013.0–2023.0
8	**720**	**1440**	**480**	177	103	52	**2013.0–2014.5**
9	360	720	240	177	103	52	**1993.0–2023.0**
10	360	720	240	177	103	52	2013.0–2023.0
11	360	720	240	**199**	**125**	**37**	2013.0–2023.0
12	360	720	240	**125**	**76**	52	**2008.0–2018.0**

Table 2.2 Run configurations: numerical parameters and time spans.

2.2.5 Canonical run

Run 6 is designated as the *canonical* run for all comparisons. This choice is made because the ocean model CMEMS mean is a multi-model ensemble. As it aggregates information from other CMEMS configurations, it retains the robust features common to them while averaging run-specific variability. The results of other runs are then directly compared to the canonical run.

3 Principal Component Analysis

3.1 Overview

Principal Component Analysis (PCA) is used as a multivariate statistical tool for high-dimensional (in the sense of a large number of variables) datasets (Pearson, 1901). In the field of geophysics and meteorology it is also known as Empirical Orthogonal Function (EOF) analysis (Lorenz et al., 1956). The core idea behind PCA is that the distribution of data can be described with the base along whose axes the data are located, these axes coincide with the directions of various levels of variance. These directions are eigenvectors of the covariance matrix, where eigenvalues give us information on how much variance is described in the direction of their associated eigenvector. These eigenvectors are called EOFs and their eigenvalues are just variances. Principal components (PCs) are obtained by projecting data onto EOFs. They represent behavior of data in the direction of EOF. Each combination of EOF and respective PC and variance will be called modes. As data can be reconstructed back from from EOFs and PCs, weighted by variances, PCA can be viewed also as method of decomposition.

With that, we are coming to different applications of PCA:

- Dimension reduction can be achieved by projecting data from low variance directions to high variance directions. By this datasets can be described by fewer features without a significant loss of information.
- As EOFs and PCs hold information on relations between variables in data, PCA acts as a method of explorative data analysis.
- For similar reasons, there is possible use of PCA as a way of parameterisation using existing relations inside data (Grüne, 2026).

In this thesis, PCA was mainly used as an explorative method and I am going to focus mainly on that.

PCA have some shortcomings. One of the major problems lies in linearity. PCA assumes linear relations between variables, so it falls short in strongly nonlinear cases. The second major problem is its data-driven nature. When working with physics-based data, features found by PCA may not have a physical explanation. The third major problem is the possible 'leakage' of information between the modes, which can manifest itself in merging of structures. These problems should not work as deterrence from using PCA, but one should be cautious when interpreting the results.

3.2 Definition

In this thesis, we follow the definitions and formulations presented in Hannachi et al. (2007).

3.2.1 Data matrix

Assume a spatio-temporal field $A(\mathbf{x}, t)$. For the gridded variant of this field we have data, where each point on the grid corresponds to the value of A at a specific time t and spatial position $\mathbf{x}$. Let us denote this value a_{ij}, where $i = 1, \ldots, n$ is the discrete time index t_i, and $j = 1, \ldots, p$ the spatial point index x_j. The data matrix A can be constructed as

$$A = (\mathbf{a}_1, \mathbf{a}_2, \ldots, \mathbf{a}_n)^T = \begin{pmatrix} a_{11} & a_{12} & \cdots & a_{1p} \\ a_{21} & a_{22} & \cdots & a_{2p} \\ \vdots & \vdots & \ddots & \vdots \\ a_{n1} & a_{n2} & \cdots & a_{np} \end{pmatrix}, \tag{3.1}$$

where $\mathbf{a}_i$ are values of the spatial grid at time t_i. As we are mostly interested in variations of the field, we define the time average as column average

$$\bar{a}_j = \frac{1}{n} \sum_{k=1}^{n} a_{kj}, \tag{3.2}$$

and then we subtract it from every component of the matrix A,

$$\tilde{a}_{ij} = a_{ij} - \bar{a}_j \tag{3.3}$$

to obtain the anomaly matrix $\tilde{A}$. From now on, we will omit the tilde and denote the anomaly matrix simply by A.

3.2.2 Definition of PCA

We use the anomaly matrix A to construct the covariance matrix, defined as

$$C_A = \frac{1}{n} A^T A. \tag{3.4}$$

We are looking for unit vectors $\mathbf{v}$ that maximise the variance in their direction, which corresponds to maximising $\mathbf{v}^T C_A \mathbf{v}$ with constraint $\mathbf{v}^T \mathbf{v} = 1$. The solution to this problem can be obtained by solving the eigenvalue problem,

$$C_A \mathbf{v}_i = \lambda \mathbf{v}_i. \tag{3.5}$$

The obtained eigenvectors $\mathbf{v}_i$ are then called *Empirical orthogonal functions* (EOFs), and eigenvalues λ_i give the measure of variance in the direction of EOFs. After finding all eigenvalues of the covariance matrix C_A, they are sorted in decreasing order. The fraction of total variance described by i-th EOF can be computed as the ratio of the i-th eigenvalue and the sum of all eigenvalues

$$\frac{\lambda_i}{\sum_j \lambda_j}.$$

By projecting anomaly field onto EOFs,

$$\mathbf{u}_i = A\mathbf{v}_i, \tag{3.6}$$

Principal components (PCs) are obtained. As EOFs are orthogonal by design, we can then decompose the anomaly matrix A into the matrices composed of all PCs and EOFs,

$$A = U_{pc} V_{eof}^T, \tag{3.7}$$

where

$$U_{pc} = (\mathbf{u}_1, \cdots, \mathbf{u}_n), \tag{3.8}$$
$$V_{eof} = (\mathbf{v}_1, \cdots, \mathbf{v}_n). \tag{3.9}$$
$$\tag{3.10}$$

3.2.3 Application of Singular Value Decomposition in PCA

The computational cost of assembling the covariance matrix and then solving its eigenvalue problem is often very high in practice. We need a more efficient method to perform PCA. This can be done by using the *Singular Value Decomposition* (SVD) of the anomaly matrix A. SVD states that any $n \times p$ matrix A can be decomposed into

$$A = U \Sigma V^T, \tag{3.11}$$

where U is the matrix of the singular vectors on the left, Σ is the diagonal matrix with singular values σ, and V is the matrix of the singular vectors on the right. For U, V holds that $U^T U = V^T V = I$. If we apply SVD on the anomaly matrix and then proceed to multiply by itself, we get the following

$$A^T A = V \Sigma U^T U \Sigma V^T = V \Sigma^2 V^T. \tag{3.12}$$

This is very similar to the rearranged eigenvalue problem (3.5) in matrix form,

$$C_A = V_{eof} \Lambda V_{eof}^T.$$

If we identify eigenvalues (variances) with singular values as

$$\Lambda = n\Sigma^2, \tag{3.13}$$

eigenvectors (EOFs) with right singular vectors,

$$V_{eof} = V, \tag{3.14}$$

we can skip the whole process of computing the covariance matrix C_A. As PCs are obtained by projecting anomaly matrix onto EOFs, we can see that

$$AV = U\Sigma = U_{pc}.$$

The left singular vectors correspond to PCs, just scaled to the unit variance.

3.2.4 Application to OIMF

PCA applied on some spatial-temporal field yields EOFs that represent spatial structures present in the field. The PCs then represent a set of uncorrelated time series, which describe the temporal variability of each spatial structure. The field studied in our case is OIMF, more specifically, results of numerical simulations

that are briefly introduced in Chapter 2. Let us denote it by $\mathbf{B}(t, \mathbf{r})$ and then the decomposition takes the form

$$\mathbf{B}(\mathbf{r}, t) = \sum_{k=1}^{K} \mathbf{B}_k(\mathbf{r}) c_k(t), \tag{3.15}$$

where $\mathbf{B}_k(\mathbf{r})$ corresponds to EOF and $c_k(t)$ to PC and K is the number of used modes. Data formatting follows the steps performed in 3.2.1.

If OIMF is outside the source region in the insulating atmosphere, it can be expressed as the gradient of the magnetic potential

$$\mathbf{B} = -\nabla U = -\left(\partial_r U, \frac{1}{r}\partial_\vartheta U, \frac{1}{r\sin\vartheta}\partial_\varphi U\right).$$

This potential can then be expressed by the series of spherical harmonic (SH) functions

$$U(\mathbf{r}, t) = a \sum_{jm} G_{jm}^{(i)}(t) \left(\frac{a}{r}\right)^{j+1} Y_{jm}(\Omega), \tag{3.16}$$

where we have already left out the external field contribution as prescribed in the OIMF simulations. Although we define PCA with the space-time field in mind, it is not difficult to apply it on different variables, as long as the data matrix follows the same format as in Subsection 3.2.1. In the case of Gauss coefficients $G_{jm}^{(i)}(t)$, each column would be a time series of one coefficient, and the row would be all coefficients at time t_i

$$A_G = \begin{pmatrix} \tilde{G}_{10}^{(i)}(t_1) & \tilde{G}_{11}^{(i)}(t_1) & \tilde{G}_{1-1}^{(i)}(t_1) & \cdots & \tilde{G}_{JJ}^{(i)}(t_1) & \tilde{G}_{J-J}^{(i)}(t_1) \\ \tilde{G}_{10}^{(i)}(t_2) & \tilde{G}_{11}^{(i)}(t_2) & \tilde{G}_{1-1}^{(i)}(t_2) & \cdots & \tilde{G}_{JJ}^{(i)}(t_2) & \tilde{G}_{J-J}^{(i)}(t_2) \\ \vdots & \vdots & \vdots & & \vdots & \vdots \\ \tilde{G}_{10}^{(i)}(t_n) & \tilde{G}_{11}^{(i)}(t_n) & \tilde{G}_{1-1}^{(i)}(t_n) & \cdots & \tilde{G}_{JJ}^{(i)}(t_n) & \tilde{G}_{J-J}^{(i)}(t_n) \end{pmatrix}, \tag{3.17}$$

where $\tilde{G}_{jm}^{(i)}(t_i)$ is the internal Gauss coefficient of degree j and order m at time t_i after subtracting the average of time, and J is the highest degree included in PCA.

The decomposition for each coefficient would be expressed as

$$G_{jm}^{(i)}(t) = \sum_{k=1}^{K} c_k(t) G_{jm,k}^{(i)}. \tag{3.18}$$

Although EOF $G_{jm,k}^{(i)}$ does not represent directly spatial structure, the corresponding mode in the field can be reconstructed by the SH summation and then applying gradient

$$\mathbf{B}_k = -\nabla U_k = -\left(\partial_r U_k, \frac{1}{r}\partial_\vartheta U_k, \frac{1}{r\sin\vartheta}\partial_\varphi U_k\right).$$

Also, this is a more convenient form to work with as it is much easier to analyse. Firstly, data matrix of Gauss coefficients has smaller dimensions than the one of the full vector field. Secondly, as the field can be represented by Gauss coefficients, important information is already in them, and analysis of the full field would only bring redundant information.

The calculations of PCA were done with package *eofs* in Python. Details of the implementation are described in Dawson (2016).

3.3 Analysis of different OIMF models

The main task of the analysis was to understand the general behaviour related to the different setups of the models. We ask ourselves the following questions:

1. If we apply spatial or temporal filtering, what happens to the data from the perspective of PCA?
2. How does the choice of ocean model affect OIMF?
3. How does the choice of the main field model affect OIMF?
4. What new information brings higher lateral resolution?
5. What is the influence of the transient switch-on effect on OIMF?
6. What is the influence of laterally varying upper-mantle conductivity on OIMF?

3.3.1 Spatio-temporal filtering

As we remove some information from the data, this is going to affect the variances of the modes. As EOFs and PCs carry spatial and temporal information, it is clear that filtering one information will, in turn, affect their respective counterpart in PCA. But it is interesting that the influence of filter will be seen also in the other one. The *canonical* run is chosen to showcase the effect of different filters on EOFs and PCs. In the case of spatial filtering, we are only interested in PCs, and in the case of temporal filtering, interest shifts to EOFs.

To quantify the similarity between the corresponding modes of two decompositions, cross-correlation is applied to either the EOFs or the PCs, depending on which representation is being compared. Defining the cross-correlation between two vectors $\mathbf{X}, \mathbf{Y}$ of size N as

$$R_{\mathbf{XY}} = \frac{\sum_{i=0}^{N}(X_i - \bar{X})(Y_i - \bar{Y})}{\sqrt{\sum_{i=0}^{N}(X_i - \bar{X})^2 \sum_{i=0}^{N}(Y_i - \bar{Y})^2}}, \tag{3.19}$$

where $\bar{X}, \bar{Y}$ are mean values of their corresponding vectors, defined as

$$\bar{X} = \frac{1}{N}\sum_{i=0}^{N} X_i. \tag{3.20}$$

Spatial filtering

Spatial filtering is applied in the spherical harmonic domain. The full SH series of the unfiltered *canonical run* has a total of 240 harmonic degrees (range of 1 - 240). We want to determine how much information is lost by truncating the SH series. Table 3.1 shows the cross-correlations for the cases of degree ranges (1 - 60) and (1 - 30). As the main field overshadows the OIMF up to degree 19, we divide range (1 - 30) into ranges (1 - 19) and (19 - 30).

We can see from Figure 3.1 that the variance of the first mode increases with higher SH degrees filtered and if we leave out lower SH degrees (range 19 - 30),

Mode	SH range			
	1-60	1-30	1-19	19-30
1	0.99	0.99	0.99	0.41
2	0.98	0.85	0.74	0.25
3	0.59	0.31	0.7	0.57
4	0.59	0.25	0.61	0.33
5	0.37	0.13	0.05	0.23

Table 3.1 Cross-correlation between PCs of coefficients with full range of degrees (1 - 240) and PCs of coefficients with various ranges of degrees. Used modes are numbered in the first column and SH degree ranges are in the first row. Comparing the overall variances of other ranges with the range of 1 - 240: (1 - 60) has 78% of the original total variance, (1 - 30) has 60%, (1 - 19) has 48%, and (19 - 30) has only 12%.

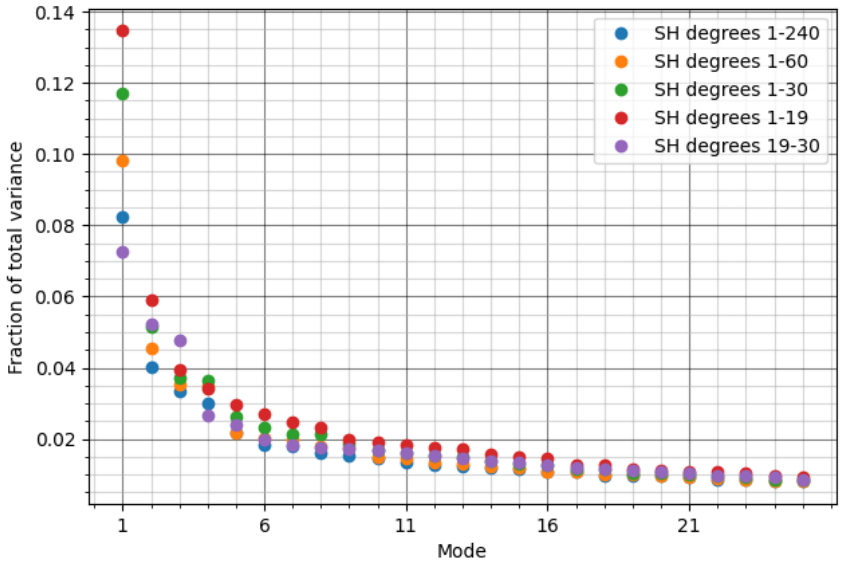


Figure 3.1 Fraction of total variance described by each mode. Shown for the SH degree range of 1 - 240, 1 - 60, 1 - 30, 1 - 19, and 19 - 30.

the described variance drops. Thus, lower SH degrees contribute to the variance described by the first mode. In the second and third modes, higher SH degrees contribute to the variance, as (range 19 - 30) now describes a higher fraction of total variance than most of the other ranges. For the rest of modes, it holds that one of the ranges in (1 - 30) describes the higher fraction of total variance than the rest. Higher SH degrees contribute to the variance of the higher modes. When we look at the overall described variance (summation of all modes variances) by modes for each range, it is decreasing, as we are excluding more and more SH degrees. It makes sense that the overall variances decrease with more filtered data, but we can see that higher SH degrees do not contribute as much variance as lower degrees.

Now we compare PCs of each range. The PCs in first mode (Figure 3.2; (a), (c), (e), (g), and (i)) are very similar to each other, apart from the PC in the range (19 - 30). The second mode PCs (Figure 3.2; (b), (d), (f), (h), and (j)) differ

more. By cross-correlating same mode PCs of range 1 - 240 with other ranges (Table 3.1), we can get information on how much they are similar to the original data.

Temporal filtering

The temporal filtering is done with the use of band pass filter that is based on a time-domain convolution with a second-order Butterworth filter (Butterworth et al., 1930). The zero phase filter is obtained by the combined action of forward-backward filter. The forward filter is applied

$$G^f_{jm}(t) = \int_{-\infty}^{\infty} B_2(t-\tau) G_{jm}(\tau) d\tau, \tag{3.21}$$

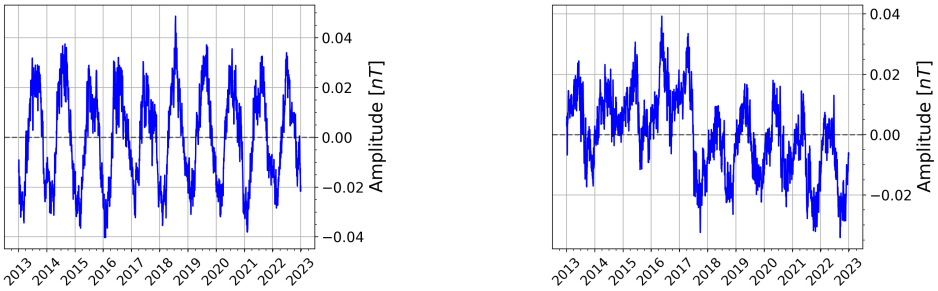
where $G^f_{jm}(t)$ is a forward filtered time series and $B_2(t)$ is an impulse function for the second-order Butterworth filter. The backward filter is then performed by convolution of the forward filter output $G^f_{jm}(t)$ with a time-reversed version of $B_2(t)$. Discrete versions of these operations are implemented in Python package *scipy.signal* as functions **filtfilt** and **butter**.

The first group of bands are [0, 30], [30, 1800], and [1800, 5400] days. The choice of these bands is determined by the other geomagnetic fields. OIMF is nearly impossible to extract on bands [0, 30] days, due to ionospheric and magnetospheric sources, and [1800, 5400] days, due to main field and litospheric/mantle sources. The [30, 1800] day band is the main band for the detection of OIMF. The second group of bands focuses on the main band, where it is divided into 4 different bands: [30, 120], [120, 240], [240, 540], and [540, 1800] days. The power spectrum of different bands, including the unfiltered signal, is presented in Figure 3.3.

From Figure 3.4a we can immediately see that filtering high frequencies significantly increases the variance of the first mode. If we look in Table 3.2, the band [1800, 5400] lost almost all the information in the filtration. Although the modes of the band [0, 30] describe fewer total variances, they still carry much information on the original data. From Figure 3.5 we see that the first mode of no bandpass data and band [30, 1800] are quite similar, and the rest focus on localised structures. Higher modes of EOFs become more different. This can also be seen in the cross-correlation Table 3.2.

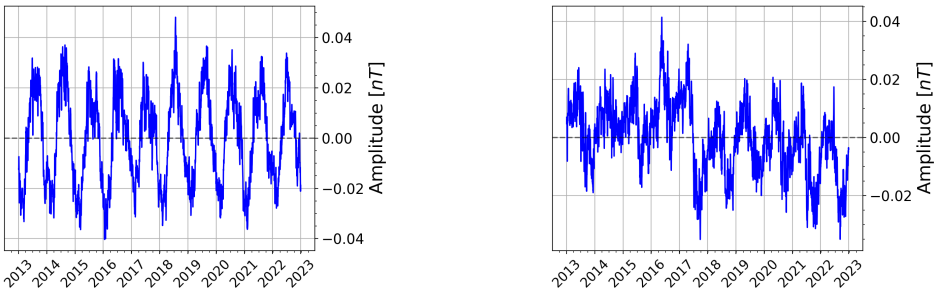
Mode	**Band (days)**		
	[0, 30]	**[30, 1800]**	**[1800, 5400]**
1	0.32	0.91	0.00
2	0.48	0.41	0.19
3	0.14	0.30	0.25
4	0.07	0.39	0.15
5	0.03	0.15	0.03

Table 3.2 Cross-correlation between EOFs of coefficients with no bandpass applied and EOFs of coefficients with various bands. Used modes are numbered in the first column and used bands are in the first row. Comparing the overall variances of other bands with no band: band [0, 30] days has 38% of original total variance, band [30, 1800] has 59%, and [1800, 5400] has only 6%.



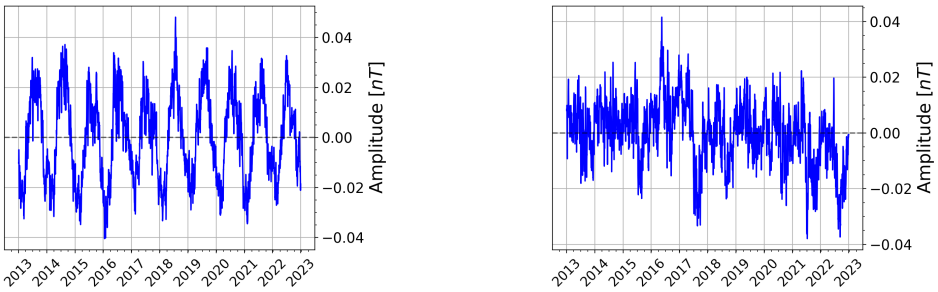
(a) 1 - 240: PC 1

(b) 1 - 240: PC 2



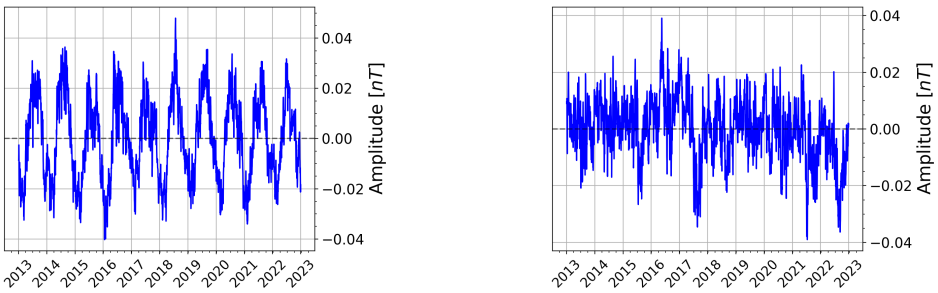
(c) 1 - 60: PC 1

(d) 1 - 60: PC 2



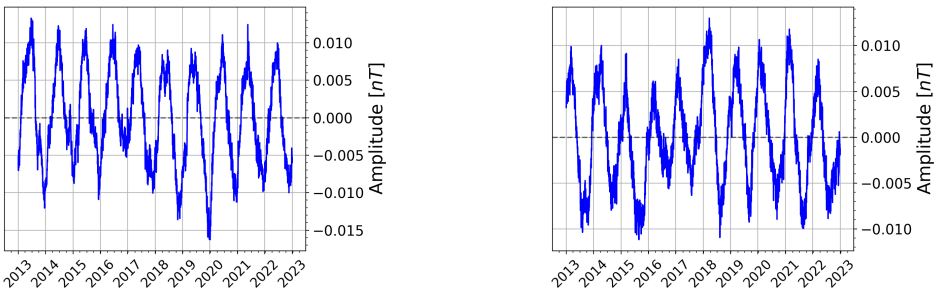
(e) 1 - 30: PC 1

(f) 1 - 30: PC 2



(g) 1 - 19: PC 1

(h) 1 - 19: PC 2



(i) 19 - 30: PC 1

(j) 19 - 30: PC 2

Figure 3.2 PCs of all used SH degree ranges.

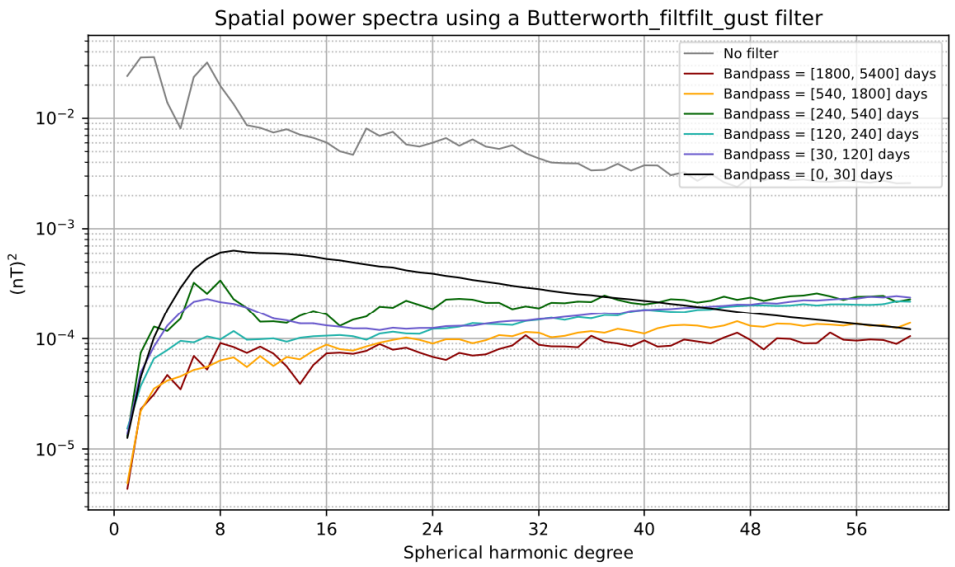


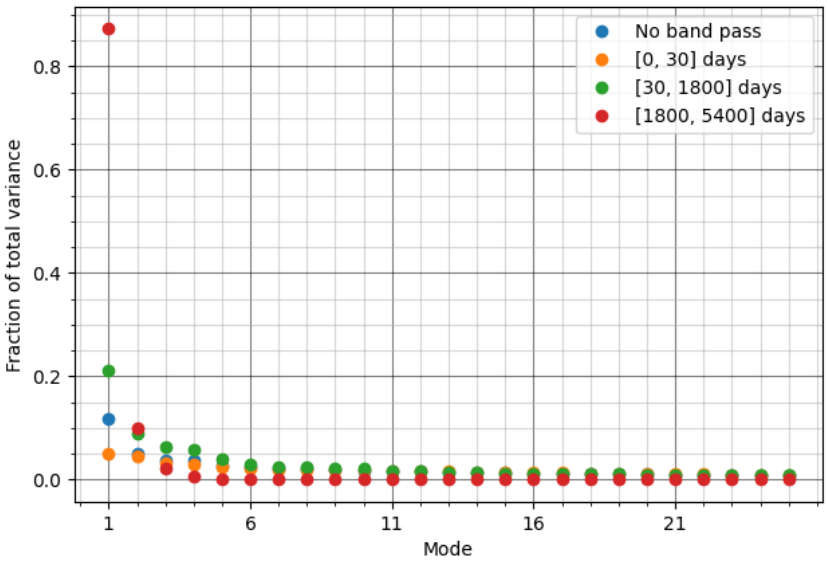
Figure 3.3 Lowes-Mauersberger power spectrum for unfiltered signal and bandpass-filtered signal at selected periods.

In Figure 3.4b we have more information on the band [30, 1800]. The first mode of the band [240, 540] describes substantially more of the total variance than the rest. The second mode of the band [240, 540] still describes the highest fraction of total variance, but the second mode of the band [540, 1800] describes almost the same fraction.

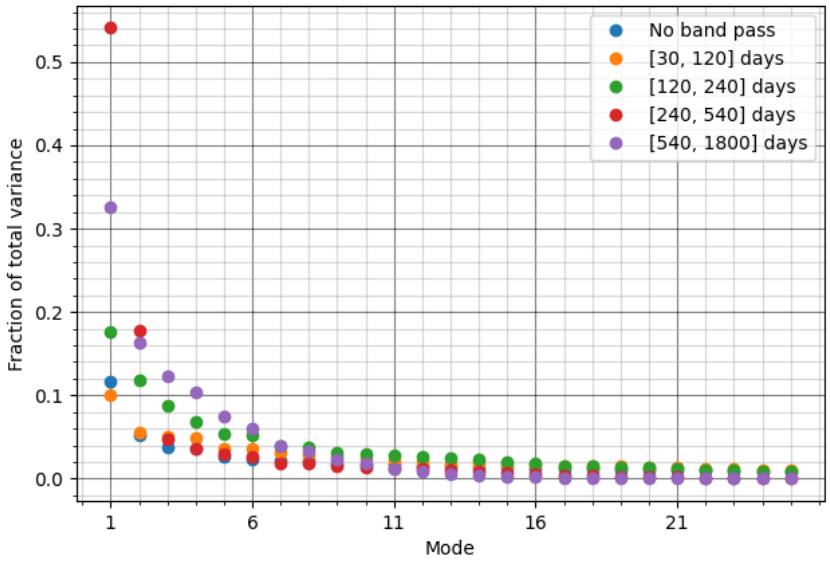
The first mode EOFs of the no band pass data and band [240, 540] share the most similarities (Figure 3.6) and the other bands concentrate more on localised features. For higher modes, they share only some features with the original data. The cross-correlations are shown in Table 3.3. The dominance of signals from band [240, 540] can be also seen in Figure 3.2, where the first PC is dominated by the annual period, which is consistent with spectral analysis of the OIMF signal (Ucekajová, 2025) and denotes the importance of seasonal variations in the temporal behaviour of OIMF.

Mode	**Band (days)**			
	[30, 120]	**[120, 240]**	**[240, 540]**	**[540, 1800]**
1	0.59	0.49	0.97	0.05
2	0.38	0.12	0.38	0.57
3	0.08	0.18	0.04	0.28
4	0.09	0.09	0.08	0.01
5	0.23	0.01	0.12	0.00

Table 3.3 Cross-correlation between EOFs of coefficients with no bandpass applied and EOFs of coefficients with various bands. Used modes are numbered in the first column and used bands are in the first row. Comparing the overall variances of other bands with no band: band [30, 120] has 15%, band [120, 240] has 9%, band [240, 540] has 17% and [540, 1800] has 7%.

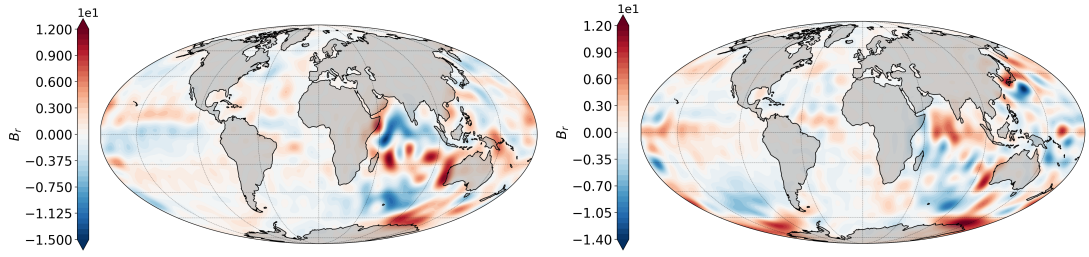


(a) No bandpass and bands of [0, 30], [30, 1800], and [1800, 5400] days.



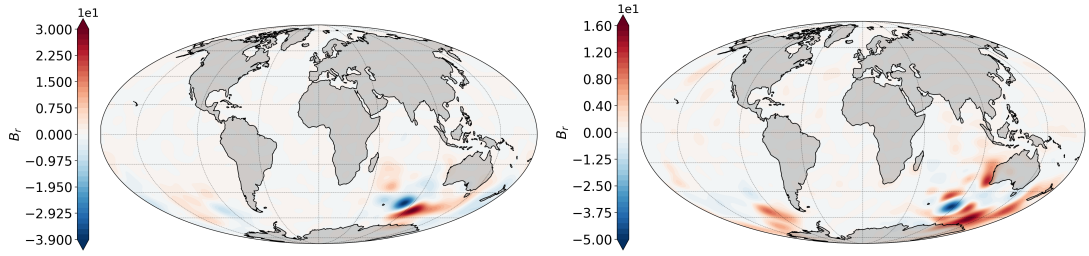
(b) No bandpass and bands of [30, 120], [120, 240], [240, 540], and [540, 1800] days.

Figure 3.4 Fraction of total variance described by each mode.



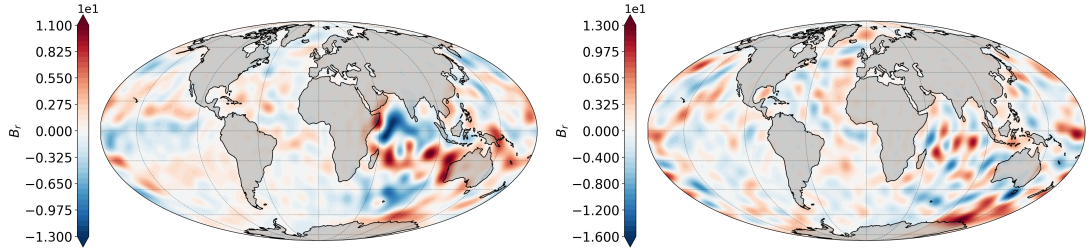
(a) No band pass: EOF 1

(b) No band pass: EOF 2



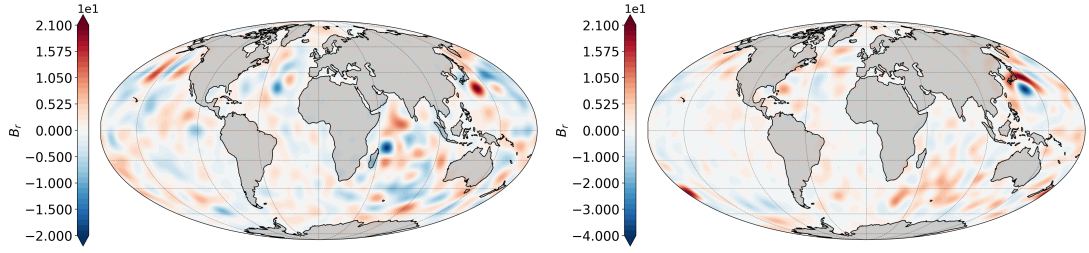
(c) [0, 30] days: EOF 1

(d) [0, 30] days: EOF 2



(e) [30, 1800] days: EOF 1

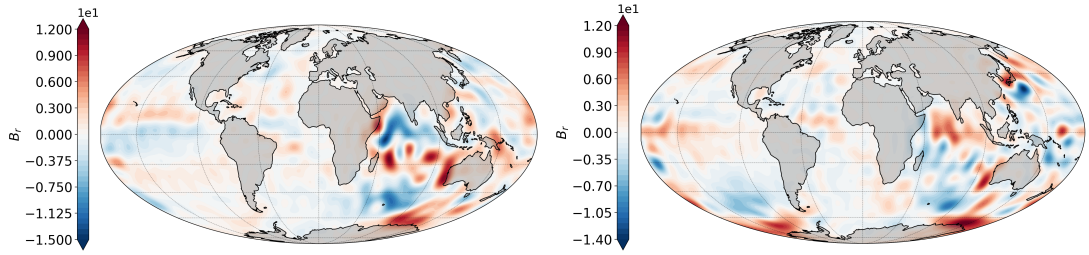
(f) [30, 1800] days: EOF 2



(g) [1800, 5400] days: EOF 1

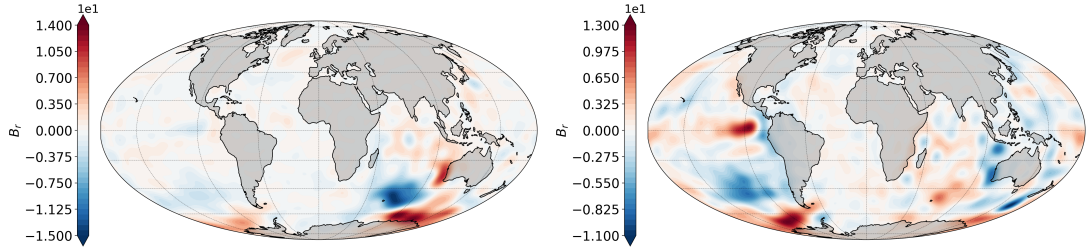
(h) [1800, 5400] days: EOF 2

Figure 3.5 EOFs for the first group of bands.



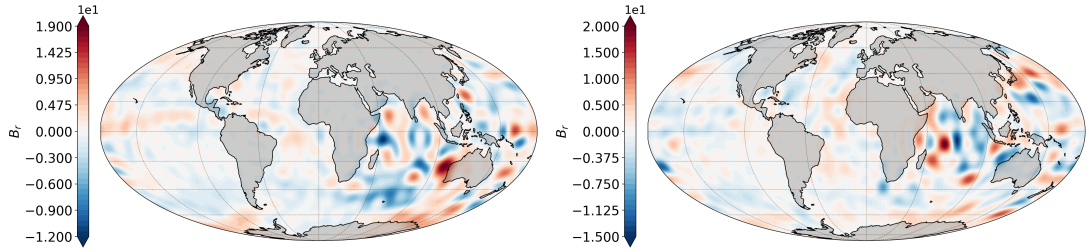
(a) No band pass: EOF 1

(b) No band pass: EOF 2



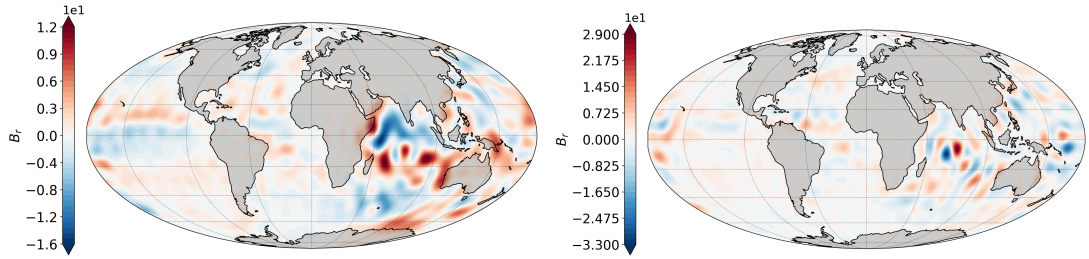
(c) [30, 120] days: EOF 1

(d) [30, 120] days: EOF 2



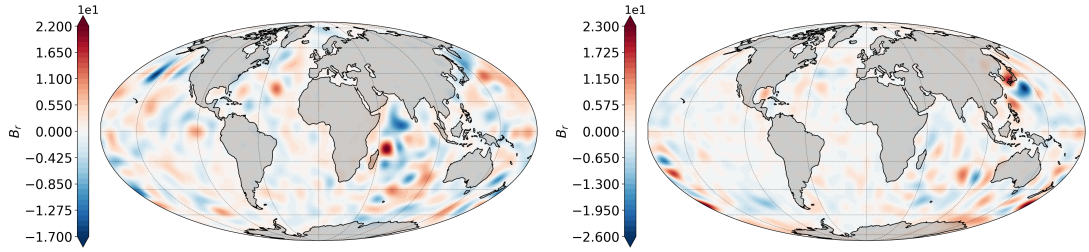
(e) [120, 240] days: EOF 1

(f) [120, 240] days: EOF 2



(g) [240, 540] days: EOF 1

(h) [240, 540] days: EOF 2



(i) [540, 1800] days: EOF 1

(j) [540, 1800] days: EOF 2

Figure 3.6 EOFs for the second group of bands.

3.3.2 Sensitivity to ocean models

The runs with different ocean models are compared to *the canonical run*: run 2, run 3, run 4, and run 5 (see Subsection 2.2.1). Only SH coefficients of degrees 1 to 30 are used with applied temporal low-pass filter for periods over 1 month.

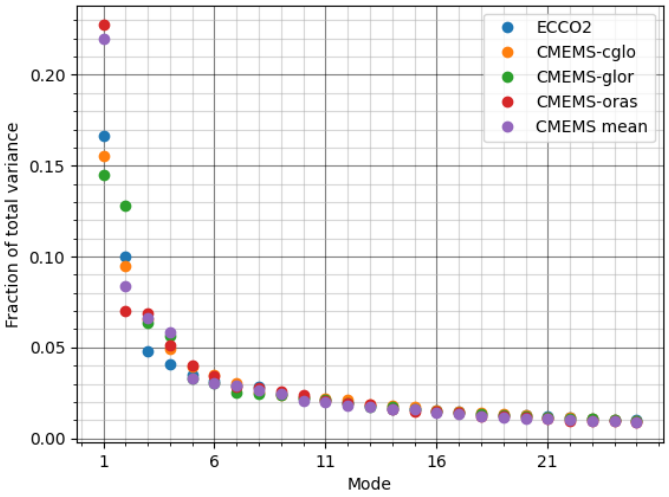


Figure 3.7 Fraction of total variance described by each mode, ocean runs.

The fraction of total variance described by the first mode of all runs is between 14% and 23% (Figure 3.7). There is a clear distinction between the CMEMS and ECCO groups. EOFs and PCs of the CMEMS group show almost the same behaviour: focus on the Indian Ocean with clearly periodic temporal variations, and ECCO focuses on the Kuroshio current near Japan with more complex variations (Figure 3.8).

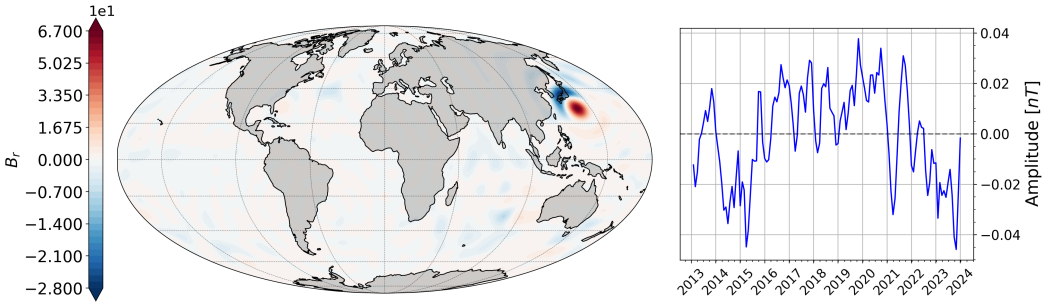
The fraction of total variance described by the second mode of all runs drops to values between 7% and 13%. Now we can see the distinctions between all runs. Run 2 has shifted its focus to the Indian ocean with periodic variations, and runs 3 and 4 have shifted their focus to the Kuroshio current with more complex variations. Run 5 still focuses on the Indian Ocean with periodic variations. Run 6 has now highlighted both the regions of the Indian Ocean and the Kuroshio current, but its variations are still periodic (Figure 3.9).

With increasing mode, the described fraction of the total variance decreases, but so does the deviation. Higher mode EOFs still show structures with features greatly varying in spatial scales. Temporal variations of higher mode PCs do not show pronounced periods as the lower ones.

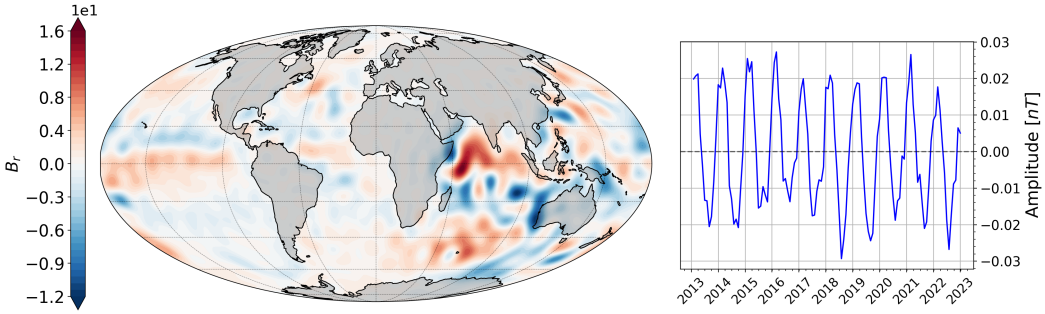
Based on this information, the OIMF is definitely sensitive to the choice of the ocean model, but we can see from the showcased modes that they describe similar structures. There are also interesting differences between models in the CMEMS group (runs 3 to 5).

3.3.3 Sensitivity to main field models

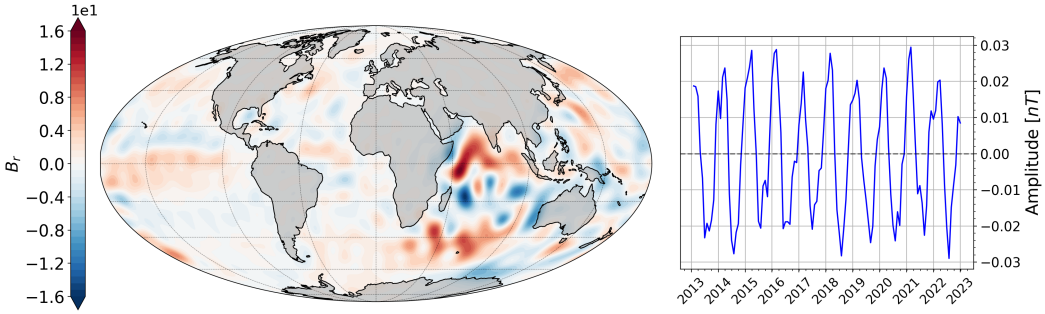
The runs with the different main field models are compared to *the canonical run*: runs 1 and 7 (see Subsection 2.2.3). Similarly to previous group, only SH



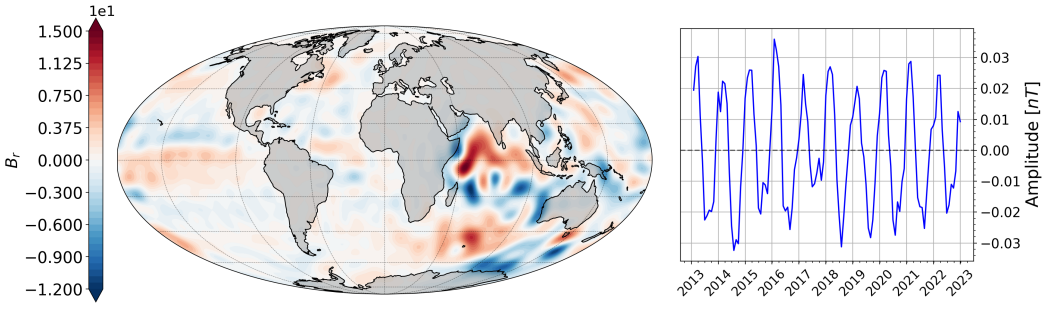
(a) ECCO2: EOF **(b)** ECCO2: PC



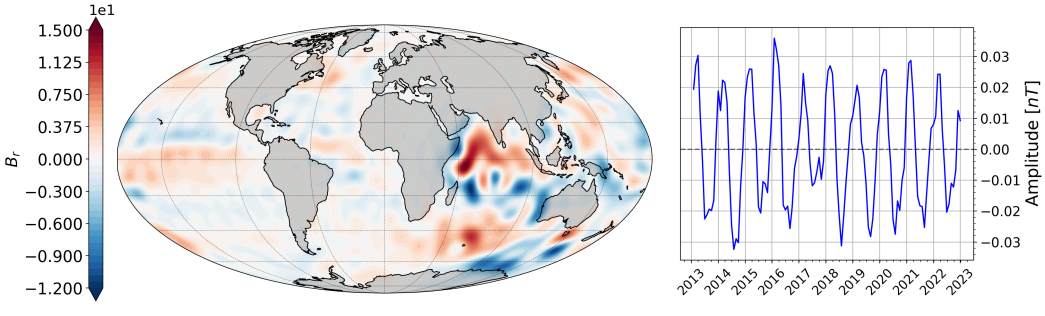
(c) CMEMS-cglo: EOF **(d)** CMEMS-cglo: PC



(e) CMEMS-glor: EOF **(f)** CMEMS-glor: PC

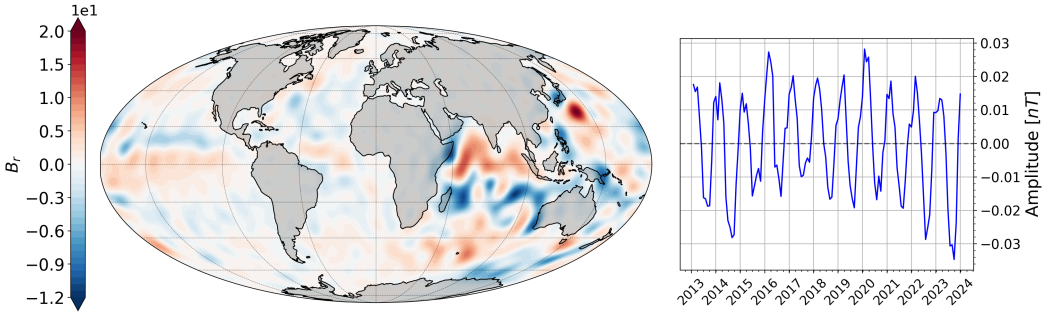


(g) CMEMS-oras: EOF **(h)** CMEMS-oras: PC

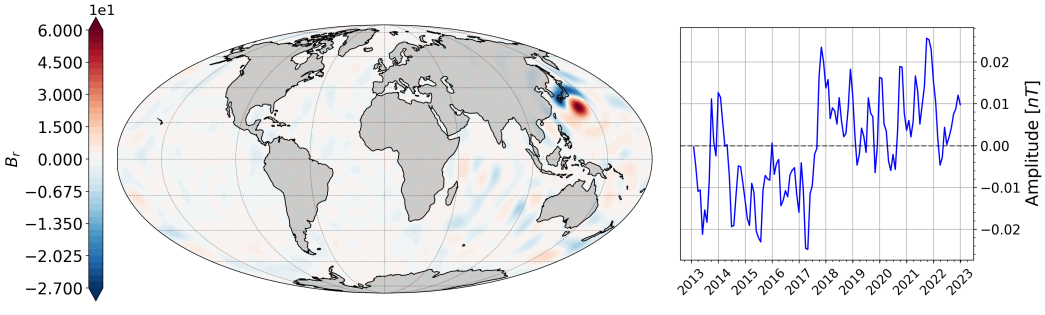


(i) CMEMS mean: EOF **(j)** CMEMS mean: PC

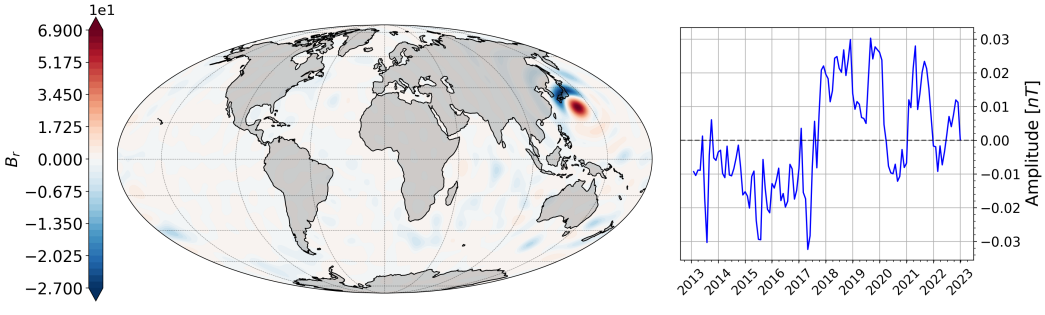
Figure 3.8 First modes of runs with different ocean models.



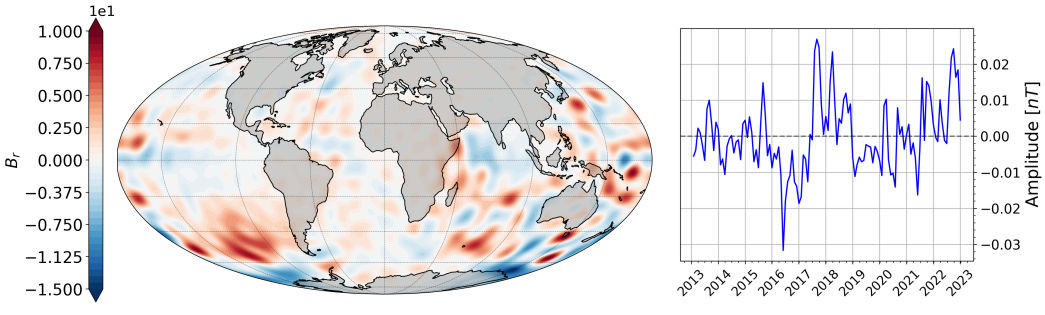
(a) ECCO2: EOF **(b)** ECCO2: PC



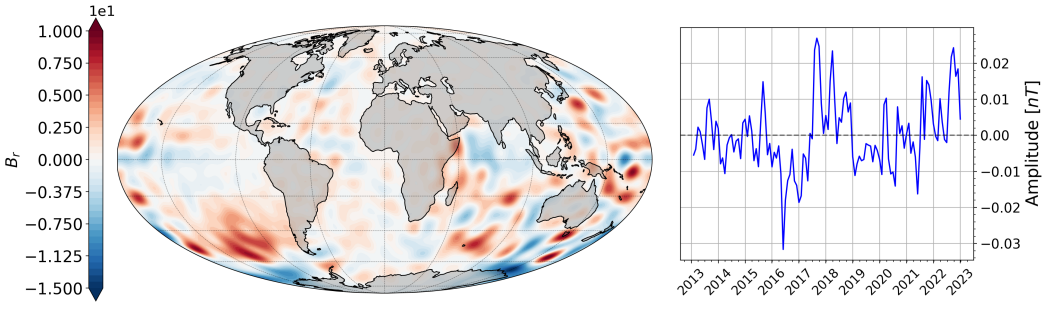
(c) CMEMS-cglo: EOF **(d)** CMEMS-cglo: PC



(e) CMEMS-glor: EOF **(f)** CMEMS-glor: PC



(g) CMEMS-oras: EOF **(h)** CMEMS-oras: PC



(i) CMEMS mean: EOF **(j)** CMEMS mean: PC

Figure 3.9 Second modes of runs with different ocean models.

coefficients of degrees 1 to 30 are kept with applied temporal low-pass filter for periods over 1 month.

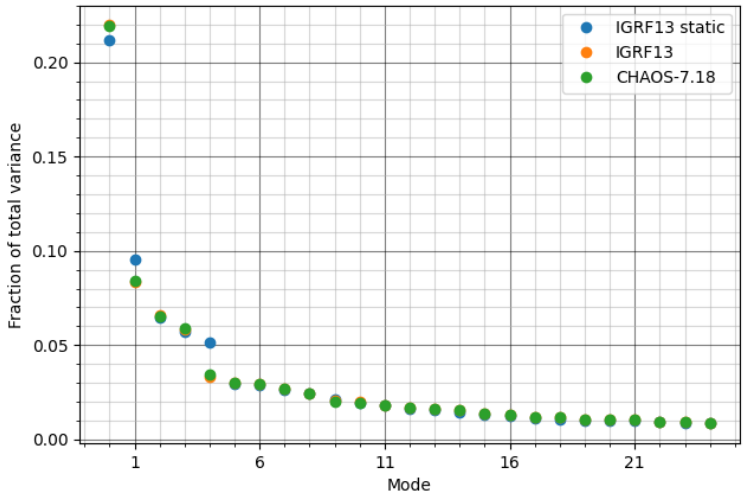


Figure 3.10 Fraction of total variance described by each mode, main field runs.

The first modes of *canonical run* and run 7 describe the same fraction of total variance that is slightly higher than the fraction of total variance described by the first mode of run 1 (Figure 3.10). There are no major differences in EOFs and PCs, with some minor exceptions that can be seen in temporal variations (Figure 3.11).

The trend of similarity between the modes of *canonical run* and run 7 continues in the higher modes (Figure 3.12). Although some higher modes of run 1 describe a higher fraction of total variance than the ones of runs 6 and 7, EOFs and PCs do not show any interesting differences.

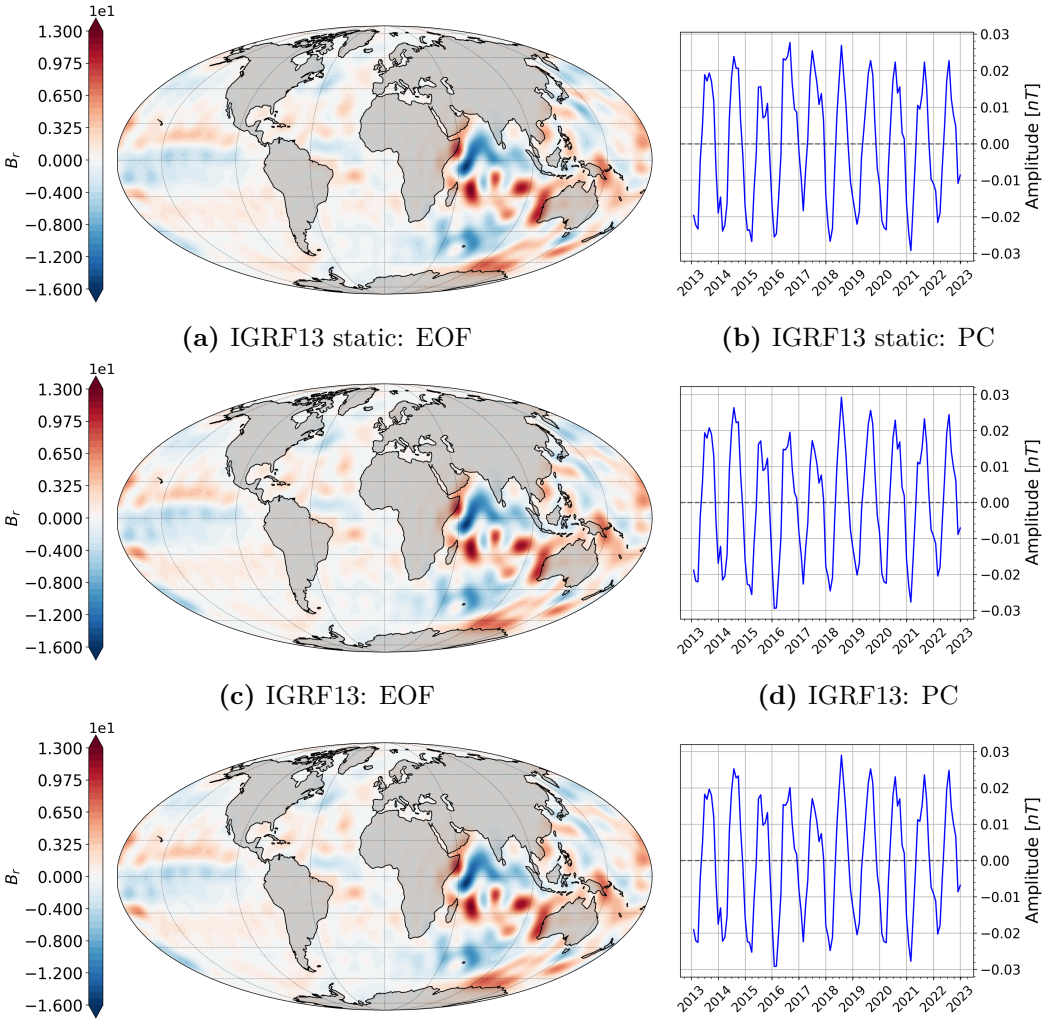
The main field models do not affect as strongly as the ocean models the final output of the OIMF. The static IGRF13 differs from the IGRF13 and CHAOS-7.18, but this is due to the absence of secular variations. As they are important to realistic description of the main field, and the IGRF13 and CHAOS-7.18 differ only little, choice of the main field model is arbitrary.

3.3.4 Lateral resolution

The lateral step of the *canonical run* is approximately 0.5°. Run 8 achieves the size of the lateral step around 0.25° for the price of the shorter time span of 1.5 years (see Table 2.1). Only SH coefficients of degrees 1 to 30 are used without any temporal filtering.

The modes of run 8 generally describe a higher fraction of total variance than those of *canonical run* (Figure 3.13). Apart from the finer details, the EOFs share similar features. PCs are harder to compare due to the shorter available time series (Figures 3.14 and 3.15).

Although OIMF with higher spatial resolution offers us finer details on already present features in *the canonical run*, to resolve important small-scale features in the oceans, we need much higher resolution (around the lateral step of 0.1°). The

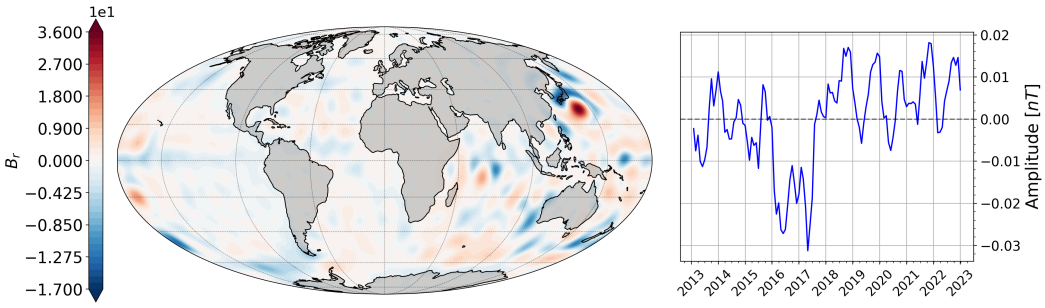


(a) IGRF13 static: EOF **(b)** IGRF13 static: PC

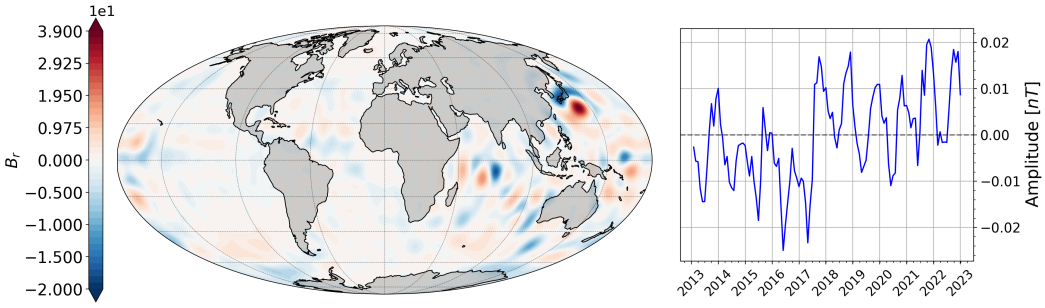
(c) IGRF13: EOF **(d)** IGRF13: PC

(e) CHAOS-7.18: EOF **(f)** CHAOS-7.18: PC

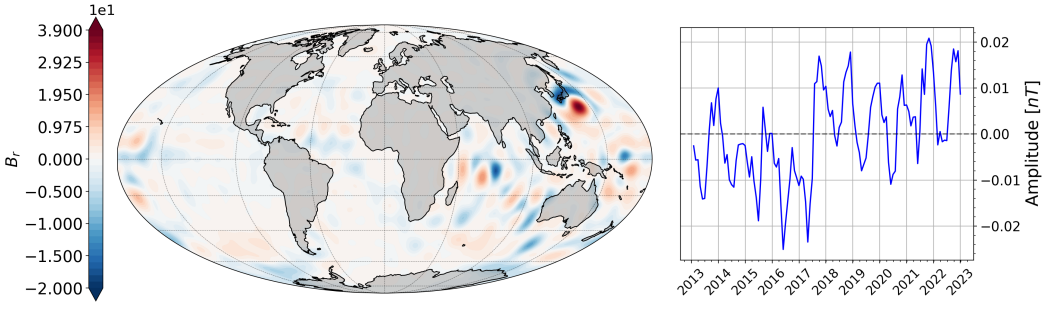
Figure 3.11 First modes of runs with different main field models.



(a) IGRF13 static: EOF **(b)** IGRF13 static: PC



(c) IGRF13: EOF **(d)** IGRF13: PC



(e) CHAOS-7.18: EOF **(f)** CHAOS-7.18: PC

Figure 3.12 Second modes of runs with different main field models.

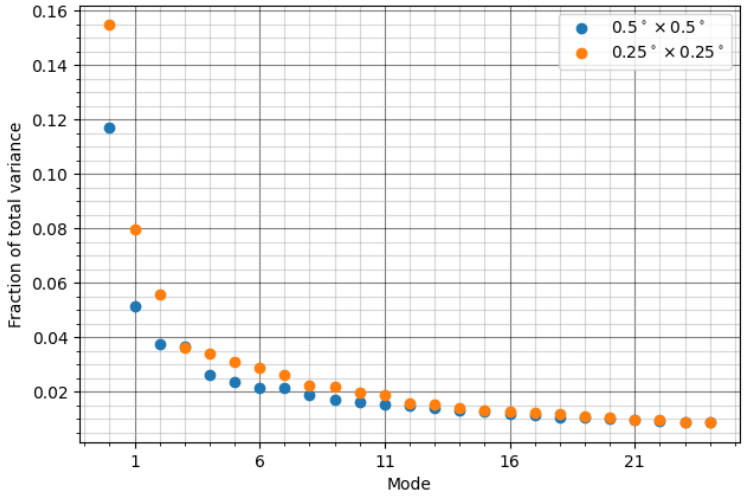
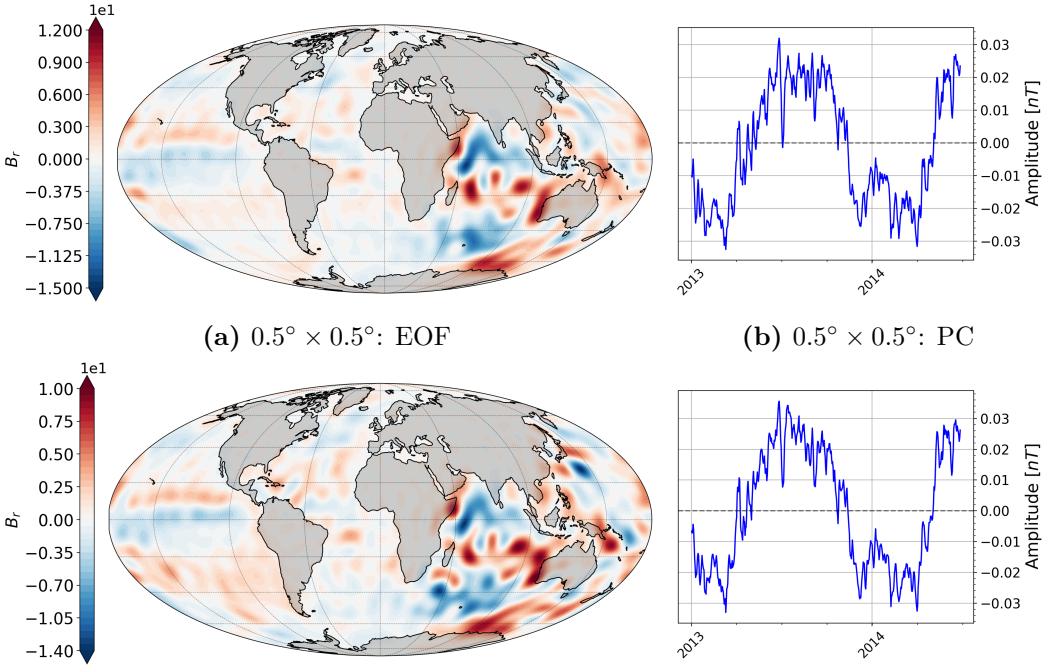


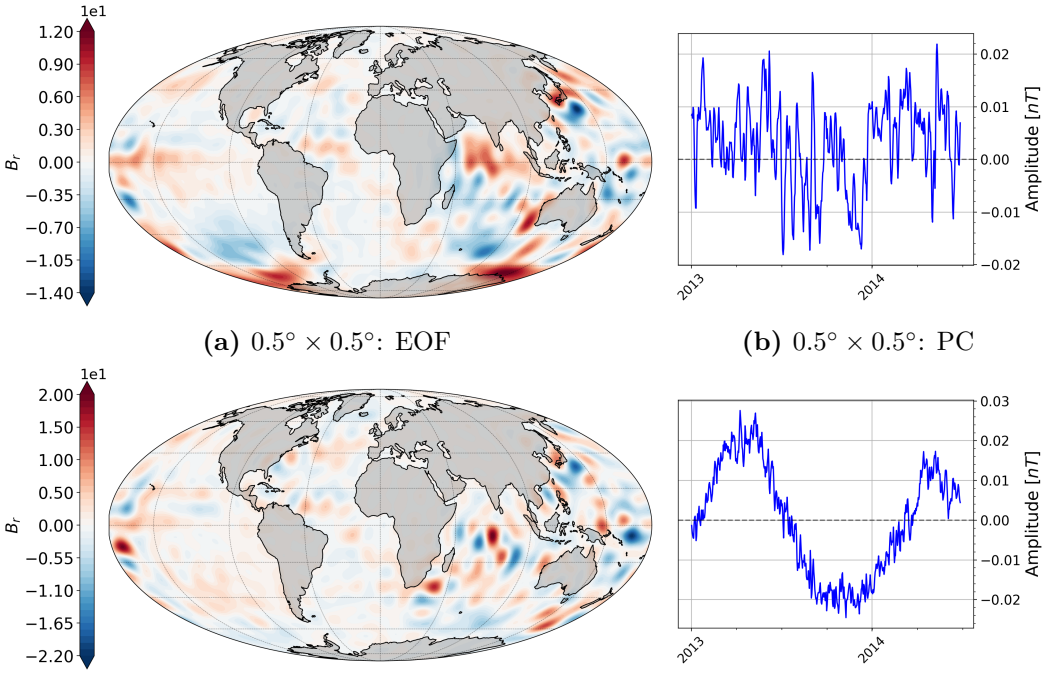
Figure 3.13 Fraction of total variance described by each mode, comparison of lateral resolution.



(a) 0.5° × 0.5°: EOF **(b)** 0.5° × 0.5°: PC

(c) 0.25° × 0.25°: EOF **(d)** 0.25° × 0.25°: PC

Figure 3.14 First modes of runs with different lateral resolution.



(a) 0.5° × 0.5°: EOF **(b)** 0.5° × 0.5°: PC

(c) 0.25° × 0.25°: EOF **(d)** 0.25° × 0.25°: PC

Figure 3.15 Second modes of runs with different lateral resolution.

resolution of run 8, even at shorter time span, required significant computation costs compared to other runs, therefore achieving higher lateral resolution was beyond of our capabilities.

3.3.5 Transient switch-on effect

In order to determine effect of initial conditions on the solution, a model with longer time series was made. Due to the time coverage of the data from the CMEMS mean, run 9 spans 30 years (1993.0 - 2023.0) compared to *the canonical run* which spans only 10 years (2013.0 - 2023.0) (see Table 2.1). Again, only SH coefficients of degrees 1 to 30 are used without the temporal filtering.

EOFs of both runs are not compared here as there is no major difference between them. In contrast to EOFs, the effect of initial conditions can be seen in PCs (Figure 3.16). The first mode shows an almost perfect fit of both runs. This is not the case for the higher modes. In second and third modes one can see some static shift of temporal variations and fourth modes are phase shifted.

3.3.6 Upper-mantle conductivity

Included mantle conductivities in *the canonical run* are only depth dependent, but interaction of oceans with the underlying layers is complex and lateral variations of mantle do play an important role. This is fixed in run 11, in which a 3-D model of mantle conductivities is included (see Subsection 2.2.2). Only SH coefficients of degrees 1 to 30 are used with applied temporal low-pass filter for periods over 1 month.

From the perspective of PCA, there is a minor difference in the fraction of total variance described by some modes (Figure 3.17). The differences between EOFs and PCs in both runs are also small (Figures 3.18 and 3.19).

Although inclusion of 3-D mantle conductivities creates a more realistic picture of OIMF, most of the differences from the 1-D mantle conductivities will be overshadowed by the main field.

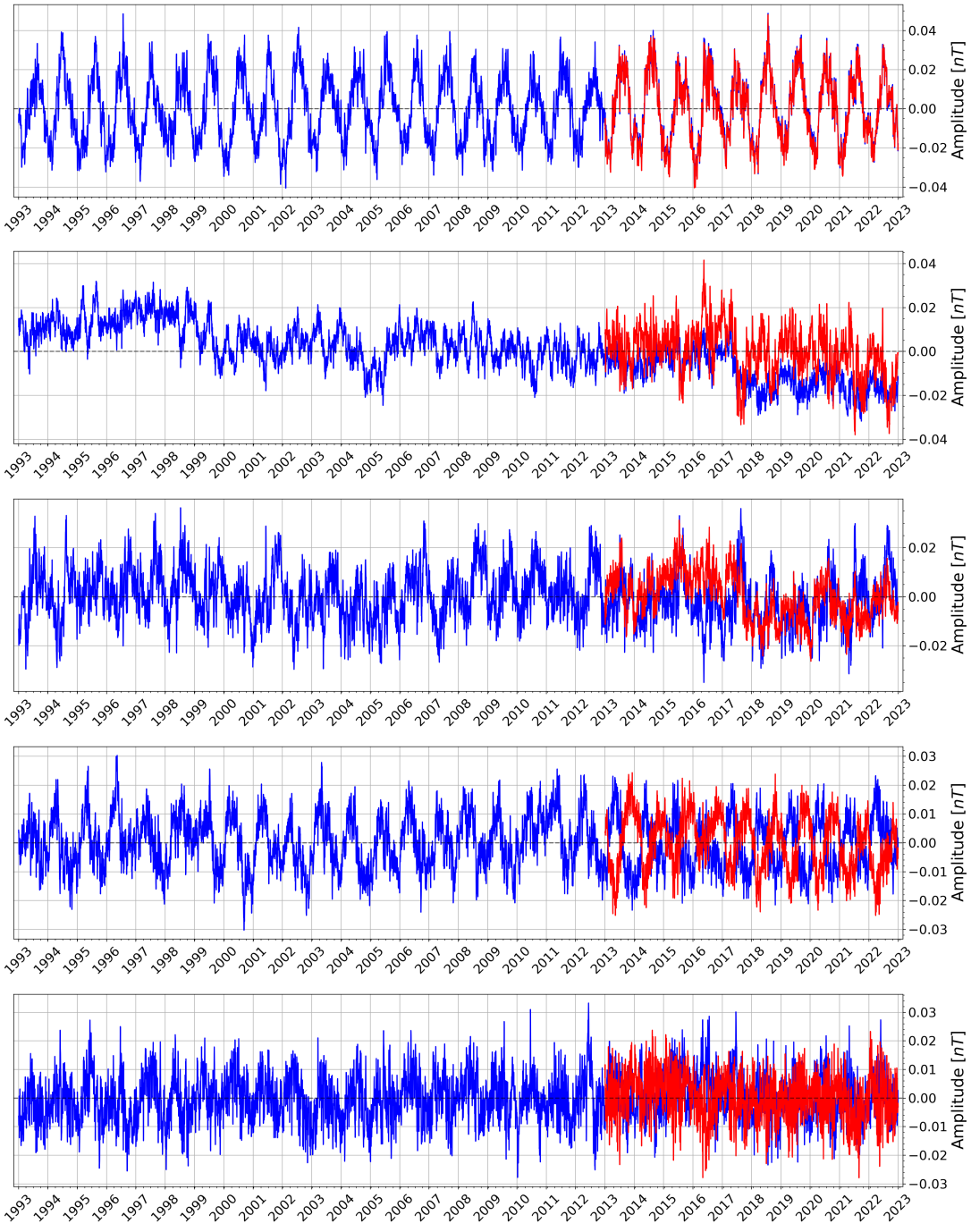


Figure 3.16 First five PCs comparing run 6 and run 9

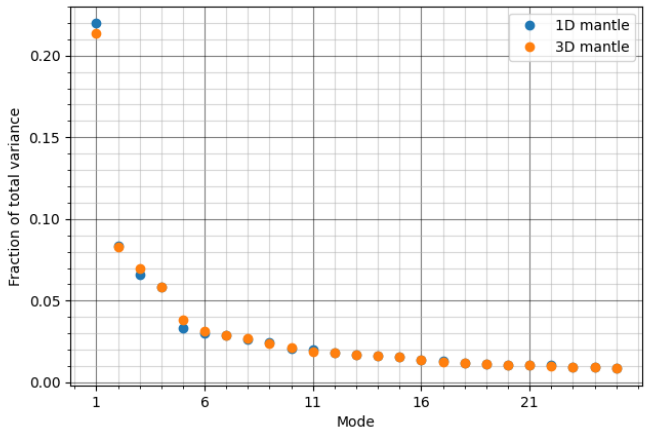
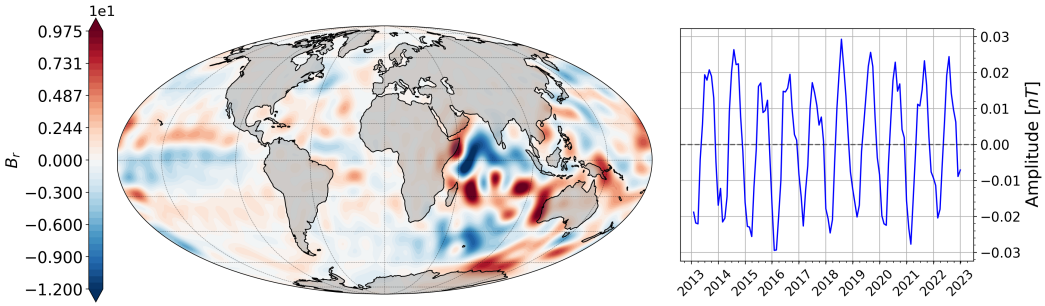
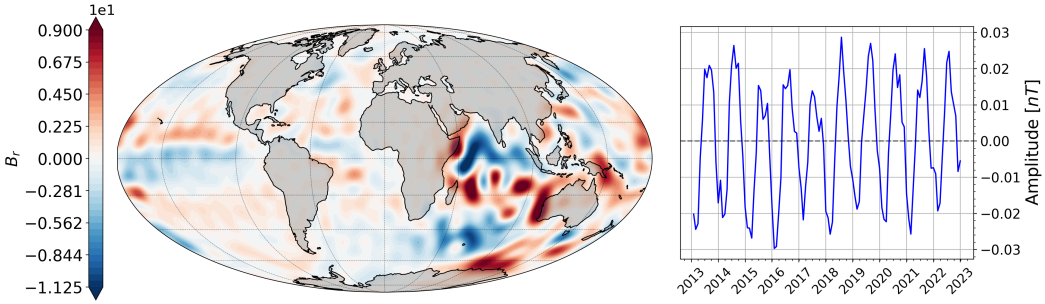


Figure 3.17 Fraction of total variance described by each mode, mantle runs.

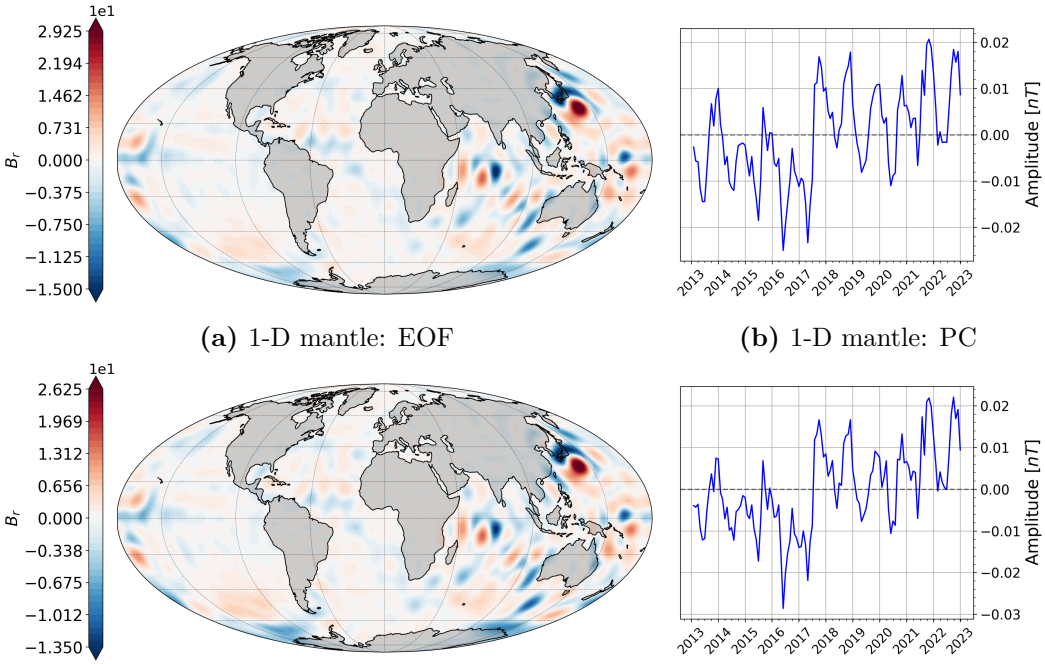


(a) 1-D mantle: EOF **(b)** 1-D mantle: PC



(c) 3-D mantle: EOF **(d)** 3-D mantle: PC

Figure 3.18 First modes of runs with different mantle models.



(a) 1-D mantle: EOF **(b)** 1-D mantle: PC

(c) 3-D mantle: EOF **(d)** 3-D mantle: PC

Figure 3.19 Second modes of runs with different mantle models.

4 Adjoint Method

One of the most straightforward ways to study an object of interest is to create a mathematical model. Equations based on physical theory are used to describe relationships in the system; initial and boundary conditions are determined if needed, and some initial parameters are prescribed. The output of the model then shows us the desired quantities. With such a tool, measurements can be predicted. This is called the *forward problem* , and an example is already mentioned in chapter 2. The predicted measurements can then be compared to actual real measurements of the system, so that the true values of the parameters can be identified. This is called the *inverse problem* (Tarantola, 2005). To summarise using OIMF:

- In the forward problem, 4-D model parameters, the ocean velocities $\mathbf{v}(\mathbf{r}, t)$ and the electrical conductivity $\sigma(\mathbf{r}, t)$, are perfectly known, and the prediction of the ocean magnetic signal is being searched for.
- In the inverse problem, the observed ocean magnetic signal is known, and the model parameters $\mathbf{v}(\mathbf{r}, t)$ and $\sigma(\mathbf{r}, t)$ that best match this signal are sought.

Following Tarantola (2005), let us define the space of all possible realisations of the model parameters $\mathbb{M}$, simply called the model space, where each point $\mathbf{m} \in \mathbb{M}$ corresponds to one realisation of the model parameters. For discrete spaces $\mathbb{M}$, the dimension would be dictated by the parameterisation of the chosen model parameters. In the case of the OIMF, this can be a complete 4-D climatology of a scalar ocean electrical conductivity and a vector velocity field with the combined dimension of $\dim(\mathbb{M}) = N_\vartheta \times N_\varphi \times (k_{max} - k_{maxl}) \times (3+1)$. For the *canonical* run this would be $360 \times 720 \times (177 - 103) \times (3 + 1) = 76\ 723\ 200$. The same is defined for the observable quantities: data space (i.e., space of all possible observations) $\mathbb{D}$ with points $\mathbf{d} \in \mathbb{D}$. In case of OIMF, these would be either spatio-temporal discretization of the magnetic induction vector $\mathbf{B}$ or the Gauss coefficients. In the general case, the forward problem can be expressed as

$$\mathbf{d} = \mathbf{g}(\mathbf{m}), \tag{4.1}$$

where the mapping $\mathbf{g} : \mathbf{m} \to \mathbf{d}$ represents the mathematical model. Solving the inverse problem would correspond to finding an inverse mapping of $\mathbf{g}$ that projects from data space to model space $\mathbf{g}^{inv} : \mathbf{d} \to \mathbf{m}$.

In practice, this is easier said than done. The first issue arises from the fact that such mapping does not have to exist at all. Finding the model parameters is often done by different means. We will return to this. The second issue is related to the uniqueness of the solution. The (deterministic) forward problem always has a unique solution that corresponds to the chosen conditions and parameters. This does not hold for the inverse problem, as there can be many various realisations of the model parameters that would fit the observations. In order to narrow down the searched area, some *a priori* information can be established through experiments, e.g. determining electrical conductivity from the properties of ocean water, or different observations, e.g. satellite observations of wave height.

If there are two realisations of the model parameters, how do we decide that one of them better describes the observations than the other? For that, some measure needs to be defined that would quantify how close the model is to reality. This role can be taken by the misfit function, for example from the least squares method (also found in Tarantola (2005)), defined as

$$\chi(\mathbf{m}) = \frac{1}{2}||\mathbf{d}_{obs} - \mathbf{g}(\mathbf{m})||^2_{\mathbb{D}} + \frac{1}{2}||\mathbf{m} - \mathbf{m_0}||^2_{\mathbb{M}}, \tag{4.2}$$

where $\mathbf{d}_{obs}$ is the vector of real observations and $\mathbf{m_0}$ is an *a priori* estimate of the model parameters. If the misfit function equals zero, the perfect match is found. It is only natural to try minimising this function, which leads us to another way to find the ideal model parameters: the optimisation problem. Minimum can be find, for example, by Newton's method,

$$\mathbf{m}_{i+1} = \mathbf{m}_i - \chi(\mathbf{m}_i)\left[D_{\mathbf{m}}\chi(\mathbf{m})|_{\mathbf{m}=\mathbf{m}_i}\right]^{-1}, \tag{4.3}$$

where $D_{\mathbf{m}}\chi(\mathbf{m})$ is the gradient of the misfit function with respect to the model parameters

$$D_{\mathbf{m}}\chi(\mathbf{m}) = \frac{d\chi(\mathbf{m})}{d\mathbf{m}} = \left(\frac{\partial\chi(\mathbf{m})}{\partial m_1}, \cdots, \frac{\partial\chi(\mathbf{m})}{\partial m_N}\right)^T. \tag{4.4}$$

The misfit gradient can be used in the more advanced methods as the Biconjugate gradient method or the variable metrics. Although there exist other methods that do not need the first derivative to find the minimum, it is one of the most efficient ways to do that. The new issue arises from the computation of the first derivative. As the model space $\mathbb{M}$ can be enormous, numerically evaluating the derivative would be a very demanding task, in principle requiring to solve $\approx \dim(\mathbb{M})$ forward problems. The use of the adjoint method can significantly reduce the computational burden (Fichtner, 2010).

The core idea behind the adjoint method is that instead of running many simulations to determine the values of the misfit gradient, only two simulations are performed. The first simulation corresponds to the original forward problem and the second one follows with simulation of the problem that is adjoint to the forward problem. The outputs of both simulations are then combined to receive a misfit gradient. For a large class of physical problems, including the EMI, the adjoint problem is mathematically similar to the forward problem, and the tools developed for its solution can be reused efficiently. The solution of the adjoint problem allows us to construct the sensitivity kernels, also known as Fréchet kernels, which carry information on how much their respective parameter influences the misfit gradient. The values of the sensitivity kernels generally depend on the spatial and temporal position, which can help identify areas of the greatest influence.

The adjoint method was already derived for the electromagnetic induction in the time-domain with forcing by the external sources and having only spatially varying electrical conductivity $\sigma(\mathbf{r})$ (Maksimov and Velímský, 2017)

$$\frac{\partial\mathbf{B}}{\partial t} + \frac{1}{\mu_0}\nabla\times\left(\frac{1}{\sigma}\nabla\times\mathbf{B}\right) = \mathbf{0}, \tag{4.5}$$

with the boundary condition defined as in (2.3 - 2.4), where external part of the magnetic potential (2.5) is prescribed as

$$G^{(e)}_{jm}(t) = G^{(e,obs)}_{jm}(t). \tag{4.6}$$

In this thesis, I further extend the derivations by adding the internal forcing and deriving the expression of the misfit gradient not only with respect to 4-D electrical conductivities $\sigma(\mathbf{r}, t)$ but also with respect to ocean velocities $\mathbf{v}(\mathbf{r}, t)$. While in Chapter 3, the sensitivity of OIMF on various parameters was studied as a whole, the following derived sensitivity kernels provide us with the spatial-temporal sensitivity of OIMF on electrical conductivity and ocean velocities. Implementation of these kernels marks the first step towards the data assimilation of OIMF into ocean models, which is however far beyond the scope of this work.

4.1 Inverse problem

Establishing the inverse problem requires the identification of parameters that belong to the data space $\mathbb{D}$ or the model space $\mathbb{M}$. As it was mentioned in the previous section, the observable quantity of the OIMF is the magnetic induction $\mathbf{B}$, but since we are focusing on satellite measurements, the magnetic field in the insulating atmosphere can be described by the potential, which in turn can be described by the coefficients of the spherical harmonic decomposition. These coefficients are the Gauss coefficients, which are more convenient to use than potential or field. So, our data space $\mathbb{D}$ is made up of all possible realisations of Gauss coefficients.

Our model parameters of interest are the electrical conductivity and ocean velocities. The electrical conductivity is not directly used and is replaced by its reciprocal value electrical resistivity

$$\rho(\mathbf{r}, t) = \frac{1}{\sigma(\mathbf{r}, t)}. \tag{4.7}$$

The reciprocity of these values (being strictly non-negative) must be taken into account in the parameterisation and is treated with the use of decadic logarithm

$$\mathbf{m}_\alpha = \{[(\rho_{ikln})]\} \tag{4.8}$$

$$\log(\rho(\mathbf{r}, \mathbf{m}_\rho; t)/\rho_0) = \sum_{n=0}^{N_t} \sum_{i=0}^{N_\vartheta} \sum_{l=0}^{N_\varphi} \sum_{k=0}^{N_r} \rho_{ikln} \gamma_n(t) \xi_{ikl}(\mathbf{r}), \tag{4.9}$$

where $\rho_0 = const.$ is the scaling constant for electrical resistivity with units $\Omega\,\mathrm{m}$, $\xi_{ijkl}(\mathbf{r})$ is a piece-wise constant function defined as

$$\xi_{ikl}(r, \vartheta, \varphi) = \begin{cases} 1, & r_k < r < r_{k+1},\ \vartheta_i < \vartheta < \vartheta_{i+1},\ \varphi_l < \varphi < \varphi_{l+1}, \\ 0, & \text{otherwise}, \end{cases} \tag{4.10}$$

and $\gamma_n(t)$ is a piece-wise constant function defined as

$$\gamma_n(t) = \begin{cases} 1, & t_n < t < t_{n+1}, \\ 0, & \text{otherwise}. \end{cases} \tag{4.11}$$

The ocean velocities can be parameterised with the use of the spherical harmonic functions

$$\mathbf{m}_\beta = \left\{ \left[\left(v^\lambda_{jmkn} \right) \right] \right\}, \tag{4.12}$$

$$\mathbf{v}(\mathbf{r}, \mathbf{m}; t)/v_0 = \sum_{n=0}^{N_t} \sum_{j=0}^{j_{max}} \sum_{m=-j}^{j} \sum_{\lambda=-1}^{1} \sum_{k=0}^{N_r} v^{(\lambda)}_{jmkn} \gamma_n(t) \zeta_k(r) \mathbf{S}^{(\lambda)}_{jm}(\vartheta, \varphi), \tag{4.13}$$

where $v_0 = const.$ is scaling constant for the ocean velocities with units $\mathrm{m\,s^{-1}}$ and $\zeta_k(r)$ is a piece-wise constant function

$$\zeta_k(r) = \begin{cases} 1, & r_k < r < r_{k+1}, \\ 0, & \text{otherwise.} \end{cases} \tag{4.14}$$

For ocean velocities, the divergence-free condition must be satisfied. This can be enforced by application of regularisation, method of Lagrange multipliers, or enforced by the chosen parameterisation. If ocean velocities have zero vertical component, the divergence-free condition can be satisfied by assuming a purely toroidal velocity field for $\lambda = 0$, where the toroidal spherical harmonics implicitly satisfy

$$\nabla \cdot [f(r)\mathbf{S}^{(0)}_{jm}(\vartheta, \varphi)] = 0. \tag{4.15}$$

The point in the model space $\mathbb{M}$ can then be expressed as

$$\mathbf{m} = \{\mathbf{m}_\alpha, \mathbf{m}_\beta\}. \tag{4.16}$$

As the external Gauss coefficients are set to zero in OIMF modelling (see Chapter 2), the data misfit function, defined in Velímský (2013), can be expressed as

$$\chi^2(\mathbf{m}) = \sum_{jm} \frac{(2j+1)(j+1)}{8\pi t_1} \int_0^{t_1} \left(\frac{G^{(i)}_{jm}(\mathbf{m}, t) - G^{(i,obs)}_{jm}(t)}{\delta^{(i)}_{jm}(t)} \right)^2 dt, \tag{4.17}$$

where t_1 is the simulation time span in seconds, $G^{(i)}_{jm}(\mathbf{m}, t)$ are the predicted internal coefficients, $G^{(i,obs)}_{jm}(t)$ are the observed internal coefficients, and $\delta^{(i)}_{jm}(t)$ are the uncertainties of their respective observed coefficients. Note that the model regularisation part of the misfit is not included here, since in the future assimilation applications, it will be provided by the ocean forward model and its adjoint, outside of scope of this derivation.

The first derivative with respect to the model parameters (i.e. parameter gradient) has the following form

$$D_{\mathbf{m}} = D_{\mathbf{m}_\alpha} + D_{\mathbf{m}_\beta}, \tag{4.18}$$

which can be viewed as the form of orthogonal decomposition of vector $D_{\mathbf{m}}$. Gradient of each model parameter has the analytical expression as

$$D_{\mathbf{m}}\rho = D_{\mathbf{m}_\alpha}\rho = -\ln 10 \rho \gamma_n \xi_{ikl}, \tag{4.19}$$

$$D_{\mathbf{m}}\mathbf{v} = D_{\mathbf{m}_\beta}\mathbf{v} = v_0 \gamma_n \zeta_k \mathbf{S}^{(\lambda)}_{jm}, \tag{4.20}$$

where $\alpha = \{i, k, l, n\}$ and $\beta = \{j, m, \lambda, k, n\}$ are multi indices.

The parameter gradient applied in 4.17 then yields

$$D_{\mathbf{m}}\chi^2(\mathbf{m}) = \sum_{jm} \frac{(2j+1)(j+1)}{4\pi t_1} \int_0^{t_1} \frac{G^{(i)}_{jm}(\mathbf{m}, t) - G^{(i,obs)}_{jm}(t)}{[\delta^{(i)}_{jm}(t)]^2} D_{\mathbf{m}} G^{(i)}_{jm}(\mathbf{m}, t) dt. \tag{4.21}$$

4.2 Adjoint problem

The EMI equation 2.1 is valid for $\mathbf{r} \in G$, where the domain G is the spherical domain with the outer boundary ∂G at the radius $a = 6371.2$ km, and for $t \in T = [0, t_1]$. The adjoint problem shares the same spatial domain and boundary, and only time t is replaced with the adjoint time

$$\hat{t} = t_1 - t, \tag{4.22}$$

where $\hat{t} \in \hat{T} = [\hat{0}, \hat{t}_1] = [t_1, 0]$. The derivation of the adjoint problem can be found in Appendix A.2.

The adjoint problem to the forward problem of the OIMF takes the form

$$\frac{\partial \hat{\mathbf{B}}}{\partial \hat{t}} + \frac{1}{\mu_0} \nabla \times \left(\hat{\rho} \nabla \times \hat{\mathbf{B}} \right) = \mathbf{0}, \tag{4.23}$$

where $\hat{\mathbf{B}}(\mathbf{r}, \hat{t})$ is the adjoint OIMF and $\hat{\rho}(\mathbf{r}, \hat{t}) = \rho(\mathbf{r}, t_1 - \hat{t})$ simply relates the resistivity expressed in normal and adjoint time. The adjoint EMI equation has the external forcing applied in the form of weighted residuals from the forward problem

$$\hat{G}_{jm}^{(e,obs)}(\hat{t}) = -\frac{j+1}{t_1} \int_{\hat{0}}^{\hat{t}} \frac{G_{jm}^{(i)}(\mathbf{m}; t_1 - \hat{\tau}) - G_{jm}^{(i,obs)}(\mathbf{m}; t_1 - \hat{\tau})}{\left[\delta_{jm}^{(i)}(t_1 - \hat{\tau}) \right]^2} d\hat{\tau}, \tag{4.24}$$

where $\hat{G}_{jm}^{(e,obs)}(\hat{t})$ are the external coefficients of the adjoint magnetic potential. These coefficients are precomputed from the difference of observed and predicted internal coefficients.

The initial conditions are set to zero

$$\hat{\mathbf{B}}(t_1) = \hat{\mathbf{B}}(\hat{0}) = \mathbf{0}, \tag{4.25}$$

and the boundary conditions are equivalent to the ones in the forward problem. In the derivation of the adjoint problem, the initial conditions of the forward problem are assumed to be independent of the model parameters

$$D_{\mathbf{m}} \mathbf{B}_0(\mathbf{r}) = \mathbf{0}, \tag{4.26}$$

which is equivalent to the Dirichlet initial condition that is obtained from the simulation earlier starting point. This simplifies the solution of the adjoint problem, since the case of parameter-dependent initial conditions would require the solution of an additional adjoint problem.

Note that the adjoint EMI equation and the adjoint external forcing are identical to those derived by Maksimov and Velímský (2017). Also note that the forward EMI equation 2.1 for the OIMF is driven purely by internal forcing and assumes zero external fields. The adjoint EMI equation 4.23, on the other hand, has no internal forcing. It is driven by the adjoint (or virtual) external field model, which depends linearly on the integrated residual between forward prediction and observation of the OIMF signal.

The misfit gradient can be calculated by

$$D_{\mathbf{m}} \chi^2(\mathbf{m}) = \int_0^{t_1} \int_G [D_{\mathbf{m}_\rho} \rho \; \mathcal{K}_\rho + (D_{\mathbf{m}_\mathbf{v}} \mathbf{v}) \cdot \mathcal{K}_\mathbf{v}] dV dt, \tag{4.27}$$

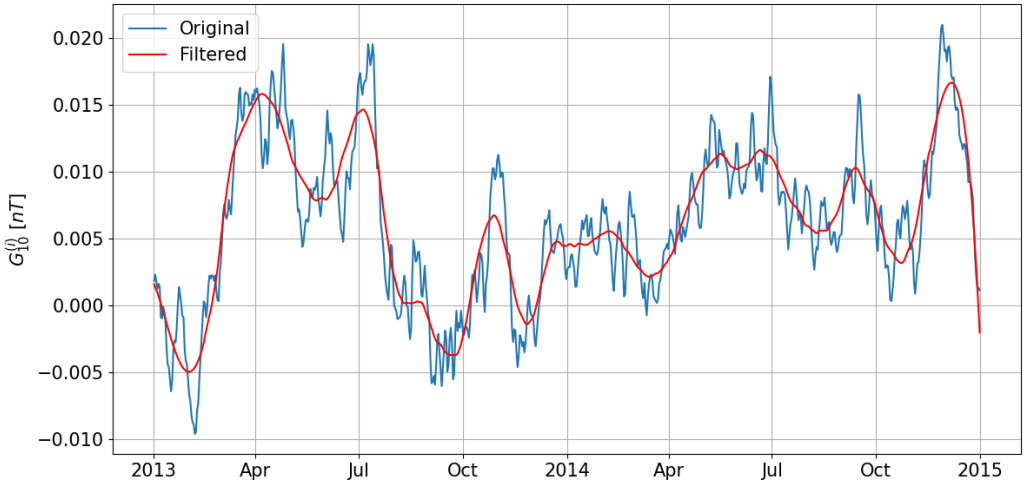


Figure 4.1 Original Gauss coefficients and their filtered variant, $j = 1$ and $m = 0$.

where $\mathcal{K}_\rho(\mathbf{r}, t)$ and $\mathcal{K}_\mathbf{v}(\mathbf{r}, t)$ are the sensitivity kernels for electrical conductivity and ocean velocities, defined as

$$\mathcal{K}_\rho = \frac{1}{4\pi a^3 \mu_0} \left(\nabla \times \hat{\mathbf{B}}(\mathbf{r}, \hat{t})\right) \cdot \left(\nabla \times \mathbf{B}(\mathbf{r}, t)\right), \tag{4.28}$$

$$\mathcal{K}_\mathbf{v} = \frac{1}{4\pi a^3} \left(\nabla \times \hat{\mathbf{B}}(\mathbf{r}, \hat{t})\right) \times \mathbf{B}_C(\mathbf{r}, t). \tag{4.29}$$

The kernel $\mathcal{K}_\rho$ is a scalar field with units $\Omega^{-1}{\cdot}\mathrm{m}^{-4}{\cdot}\mathrm{s}^{-1}$ and the kernel $\mathcal{K}_\mathbf{v}$ is a vector field with units m^{-4}.

4.3 Examples of sensitivity kernels

Here I demonstrate the application of the adjoint method to calculate the resistivity and velocity sensitivity kernels in a simplified, synthetic setup. For this purpose, I first establish a simplified forward run, based on run 11 (CMEMS ocean model, 3-D upper mantle), but with reduced spatial resolution to 90 latitude nodes and 180 longitude nodes, and a spherical harmonic expansion truncated at $j_{max} = 60$. The time span is limited to two years, from 2013.0 to 2015.0. This simulation is denoted a run 13.

The spherical harmonic coefficients from run 13 are then low-pass filtered using the Savitzky–Golay filter (Savitzky and Golay, 1964; implementation from *scipy.signal* as function **savgol_filter**) to suppress periods below 3 months. This simulates the inability of satellite-based measurements to recover short-period OIMF variations. An example of the filter application to the dipole coefficient is shown in Figure 4.1. The residua between the filtered and unfiltered coefficients are then used to force the adjoint problem 4.23, in particular to calculate the adjoint external boundary condition 4.24.

The resistivity and velocity kernels are then shown as time-averaged maps at selected depth, by means of longitude-time and latitude-time plots at selected depth, or as depth-time cross-sections at five selected locations, shown in Figure 4.2,

1. Atlantic ocean (Gulf stream); 38° N and 54° W,

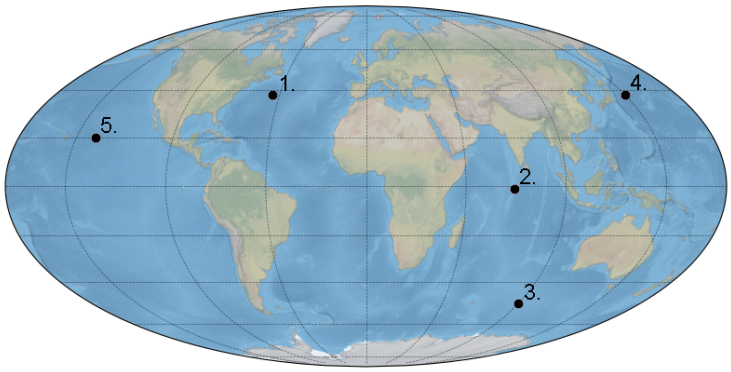


Figure 4.2 Chosen locations to showcase figures at the specific geographical coordinates.

2. Indian ocean; 1° S and 74° E,
3. Indian ocean (Antarctic circumpolar current); 50°S and 100°E,
4. Pacific ocean (Kuroshio current near Japan); 38°N and 150°E,
5. Pacific ocean; 20°N and 140°W.

4.3.1 Electrical resistivity

The sensitivity kernel $\mathcal{K}_\rho$ has the highest values at depths of around 100 metres with negligible sensitivities outside of them (Figure 4.3). From the latitude-longitude map at depth 102.31 m (Figure 4.4) it can be seen that there are two areas of significant sensitivity that correspond to the Gulf stream and the Antarctic circumpolar current (ACC). Fixing the longitude coordinate and looking at the time evolution of the sensitivities along the meridians, apart from the Gulf stream and the ACC, some faint signatures can be seen in the Indian ocean (Figure 4.5). This also holds for the time evolution of sensitivity along some parallels (Figure 4.6).

4.3.2 Ocean velocities

The radial component of the sensitivity kernel $\mathcal{K}_\mathbf{v}$ is not shown, due to the absence of the radial component of ocean velocities from the ocean model CMEMS mean.

Similarly to the kernel $\mathcal{K}_\rho$, the sensitivity kernel $\mathcal{K}_\mathbf{v}$ has the highest values at depths of around 100 metres, but now the values from the greater depth are less dampened (Figures 4.7 and 4.8). There are also non-negligible near-surface sensitivities. Following with the latitude-longitude plots (Figures 4.9a and 4.9b) the major areas of sensitivity of the Gulf stream and ACC are more pronounced than of the kernel $\mathcal{K}_\rho$, also new areas of sensitivity can be seen in the Indian ocean and weak patches in the Pacific ocean (Kuroshio current and near the west coast of USA). The time evolution of the sensitivity along the meridians does not show any new areas (Figures 4.10 and 4.11). The evolution of time along parallels reveals some sensitivities in the Atlantic ocean around the Equator (Figure 4.12).

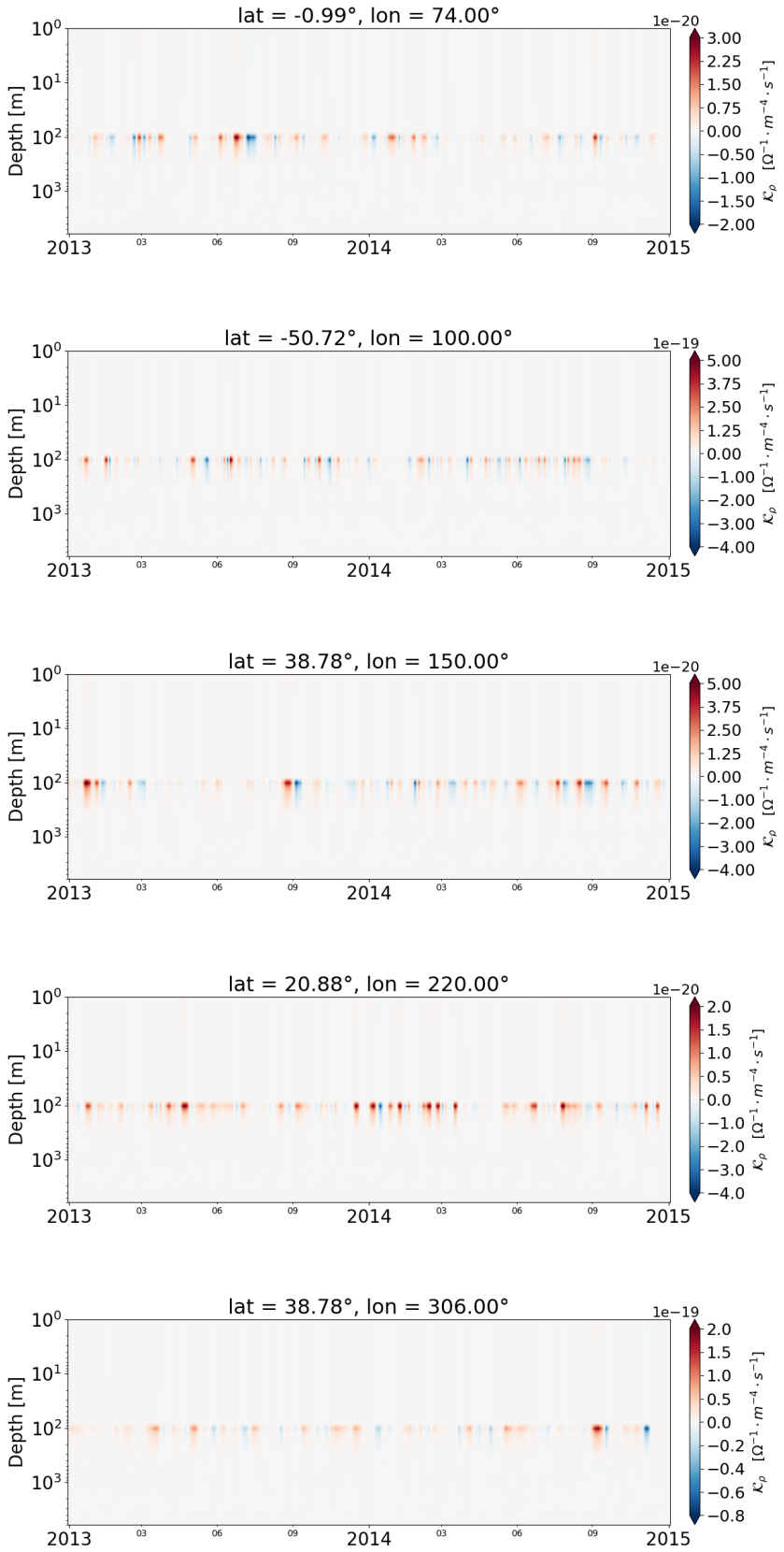


Figure 4.3 Depth-time plot of sensitivity kernel $\mathcal{K}_\rho$ at various geographical points.

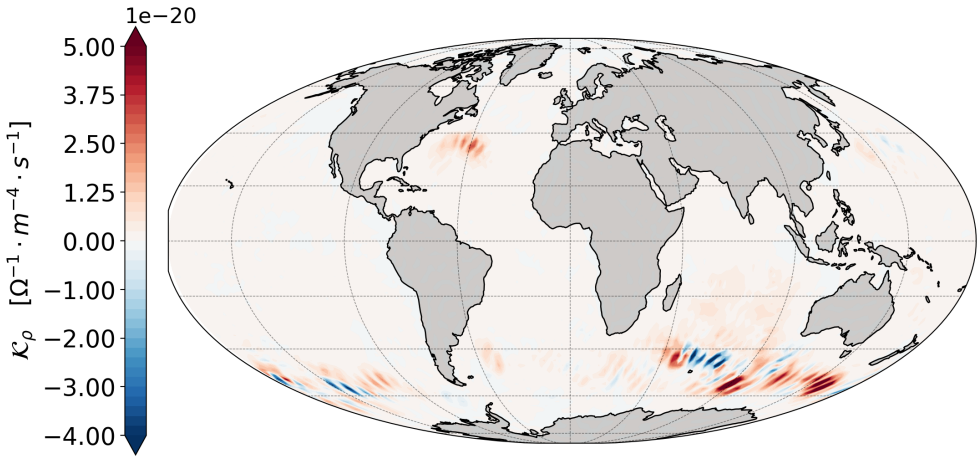


Figure 4.4 Time average of the sensitivity kernel $\mathcal{K}_\rho$ at depth 102.31 m.

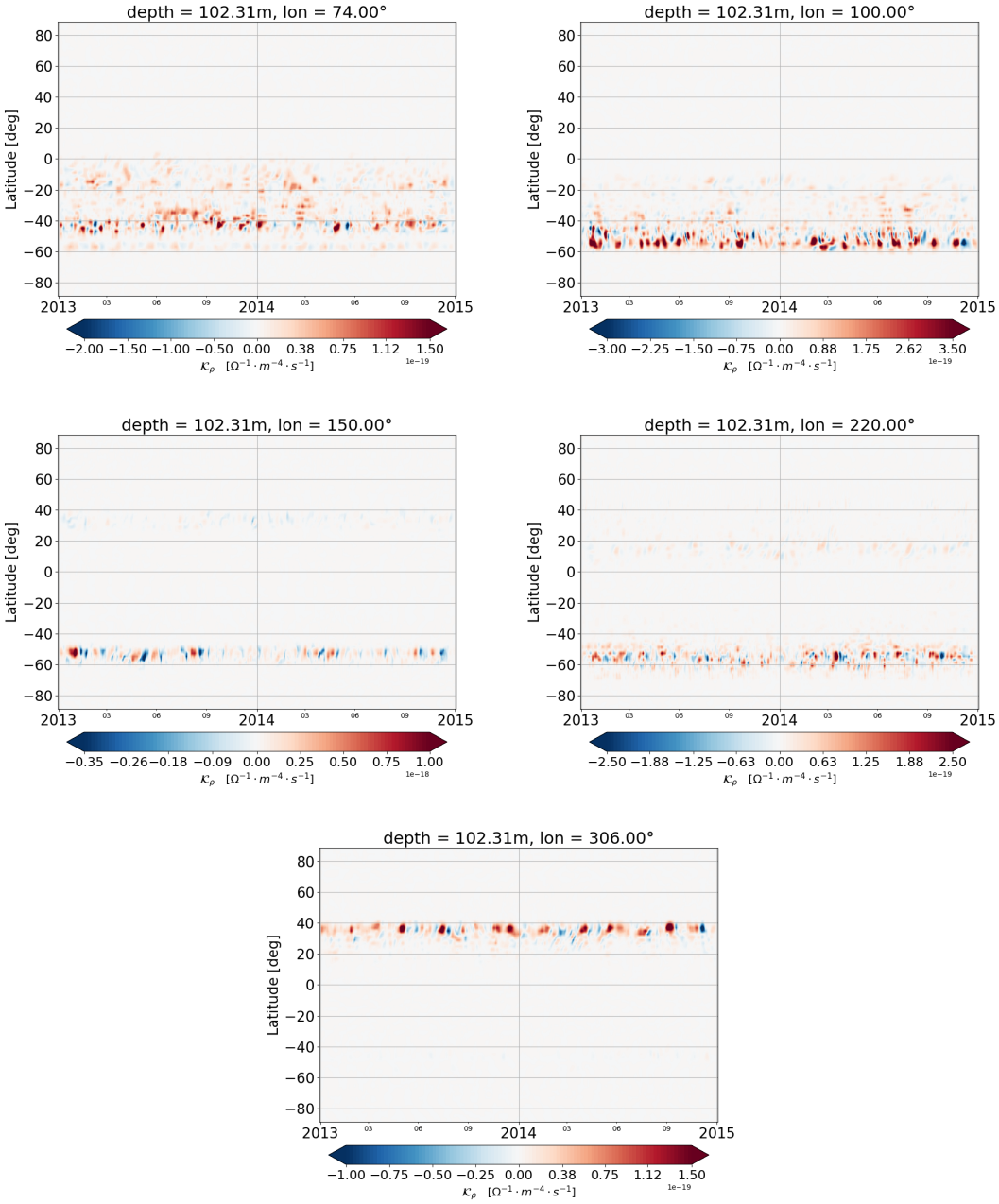


Figure 4.5 Latitude-time plot of sensitivity kernel $\mathcal{K}_\rho$ at depth 102.31 m at various longitudes.

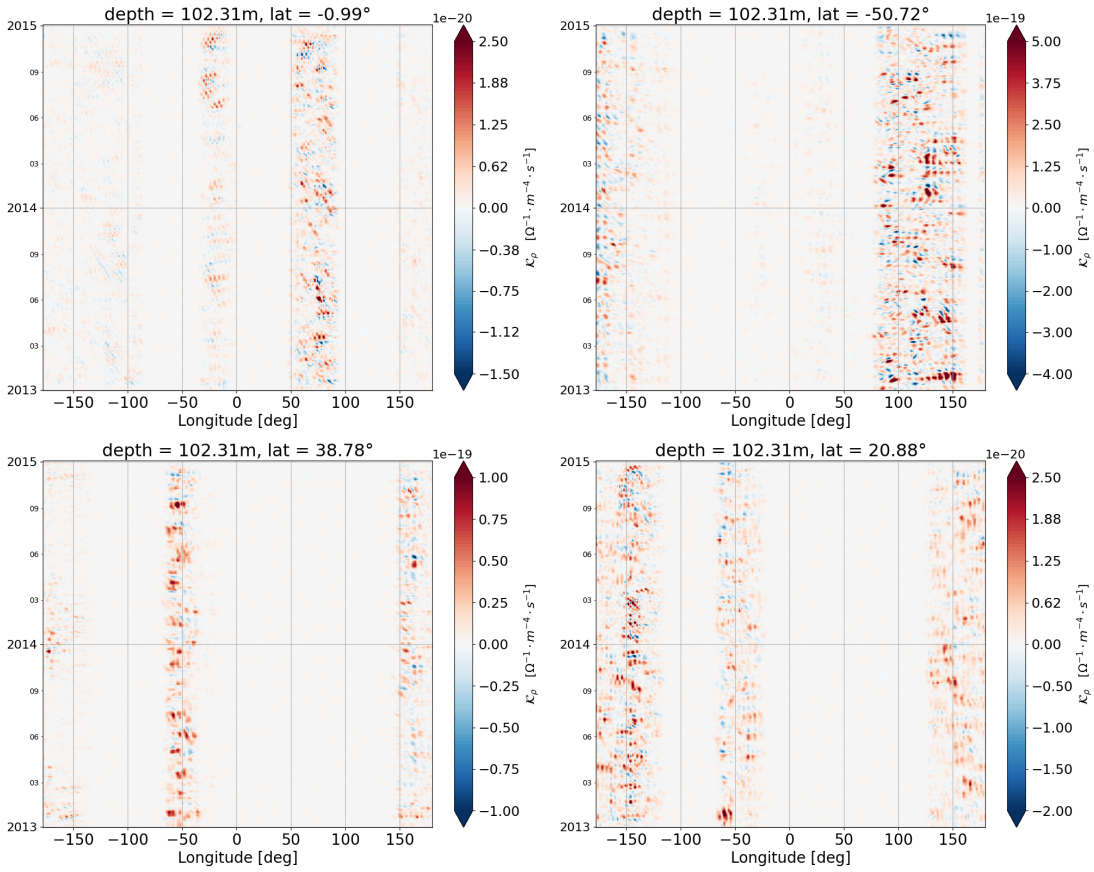


Figure 4.6 Longitude-time plot of sensitivity kernel $\mathcal{K}_\rho$ at depth 102.31 m at various latitudes.

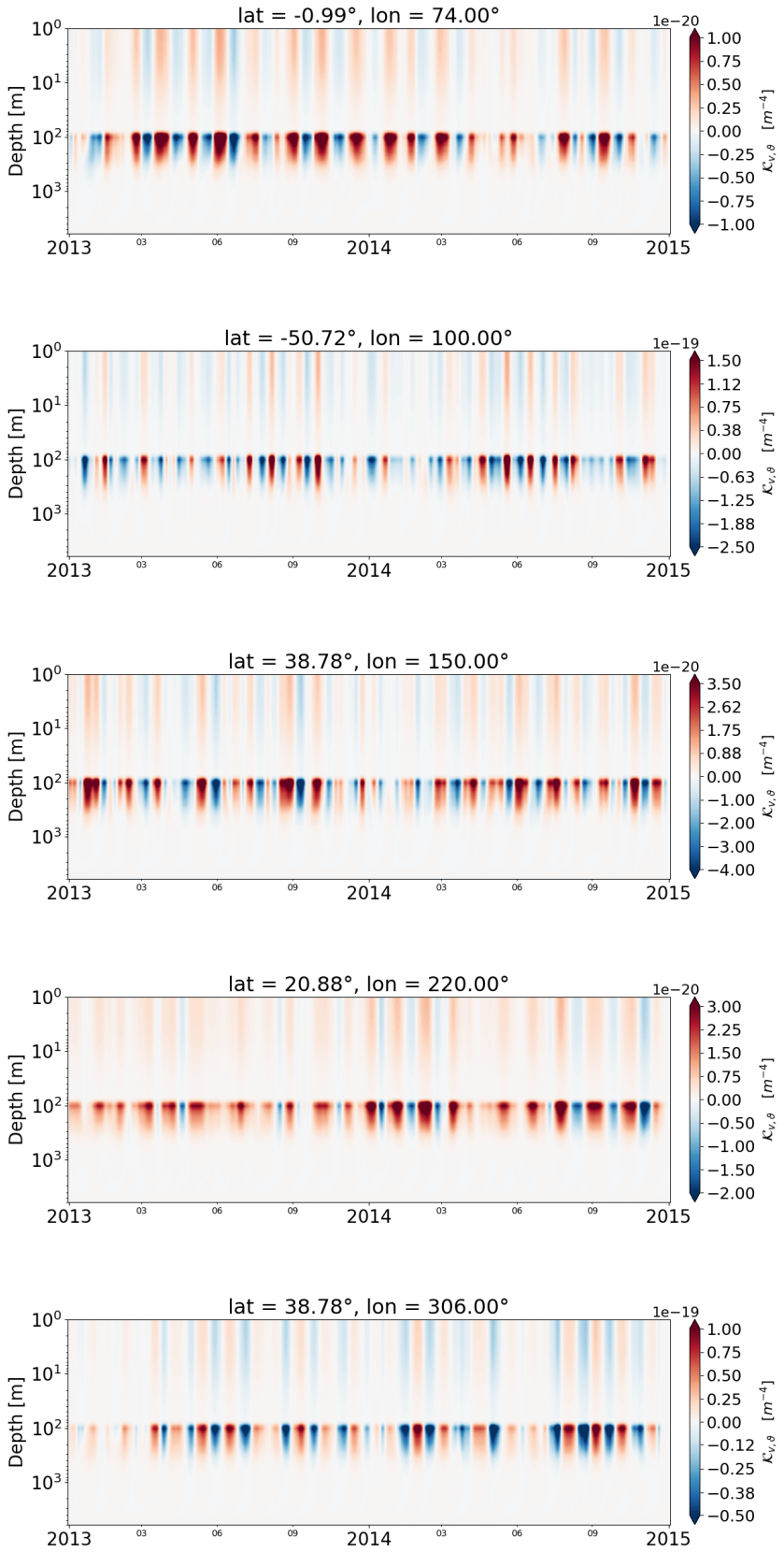


Figure 4.7 Depth-time plot of sensitivity kernel $\mathcal{K}_{\mathbf{v}}$ at various geographical points, ϑ component.

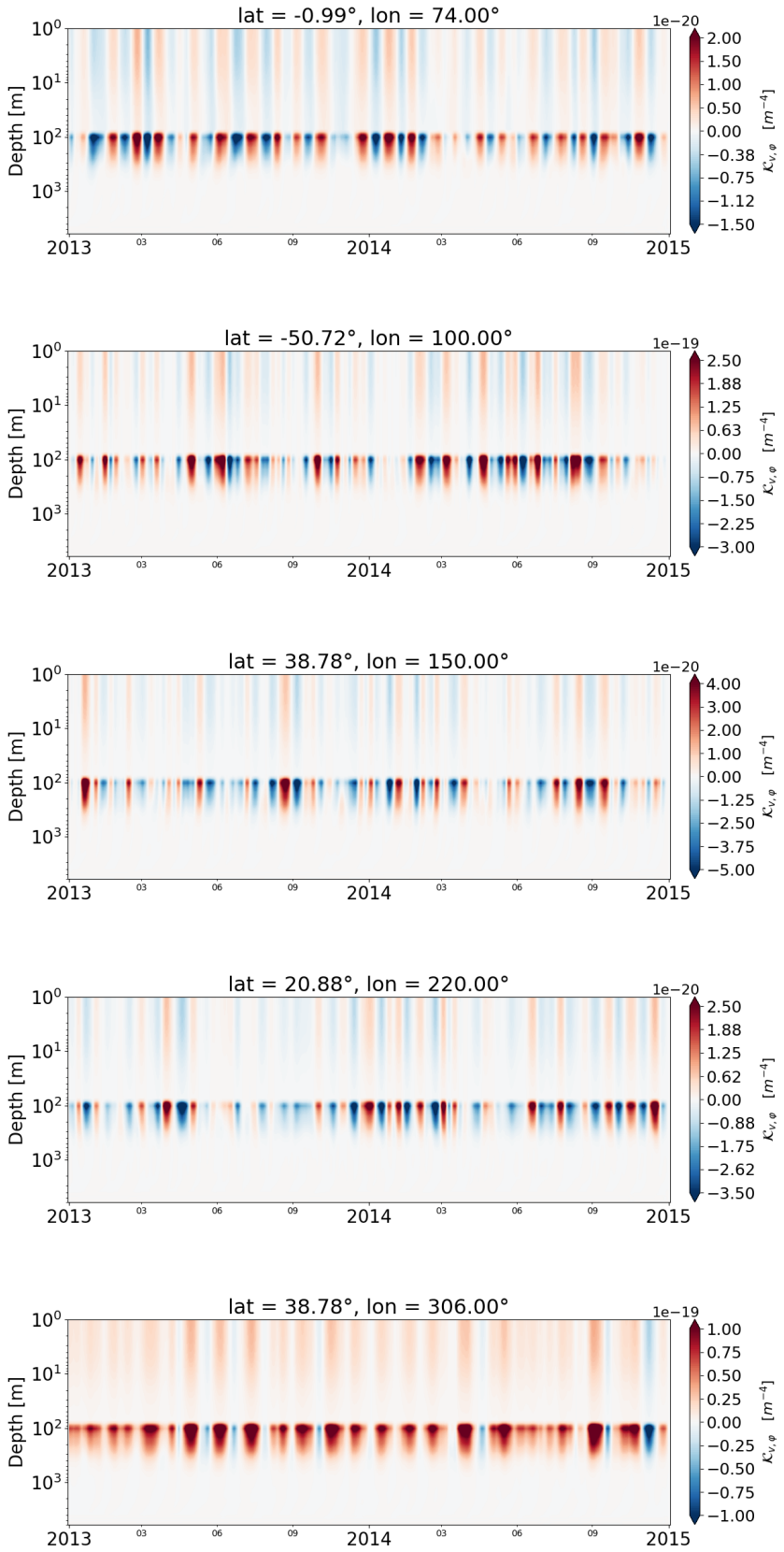
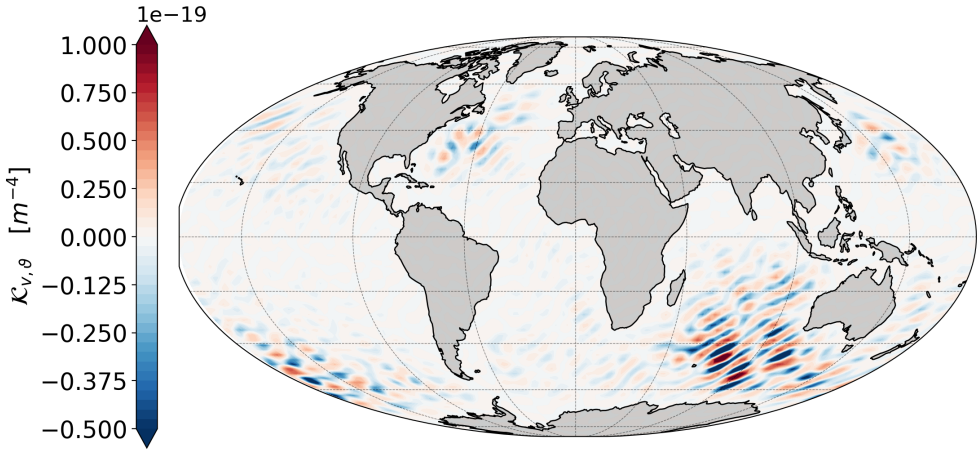
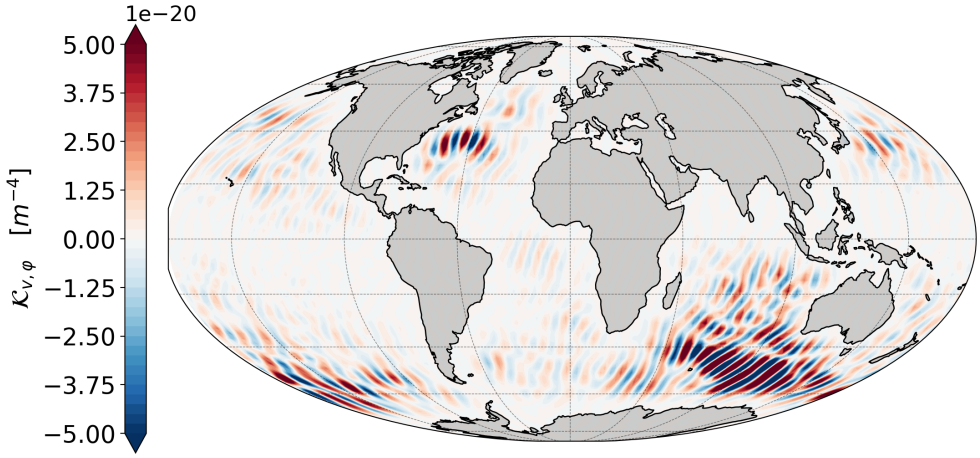


Figure 4.8 Depth-time plot of sensitivity kernel $\mathcal{K}_{\mathbf{v}}$ at various geographical points, φ component.



(a) ϑ component of $\mathcal{K}_{\mathbf{v}}$



(b) φ component of $\mathcal{K}_{\mathbf{v}}$

Figure 4.9 Time average of the sensitivity kernel $\mathcal{K}_{\mathbf{v}}$ at depth 102.31 m.

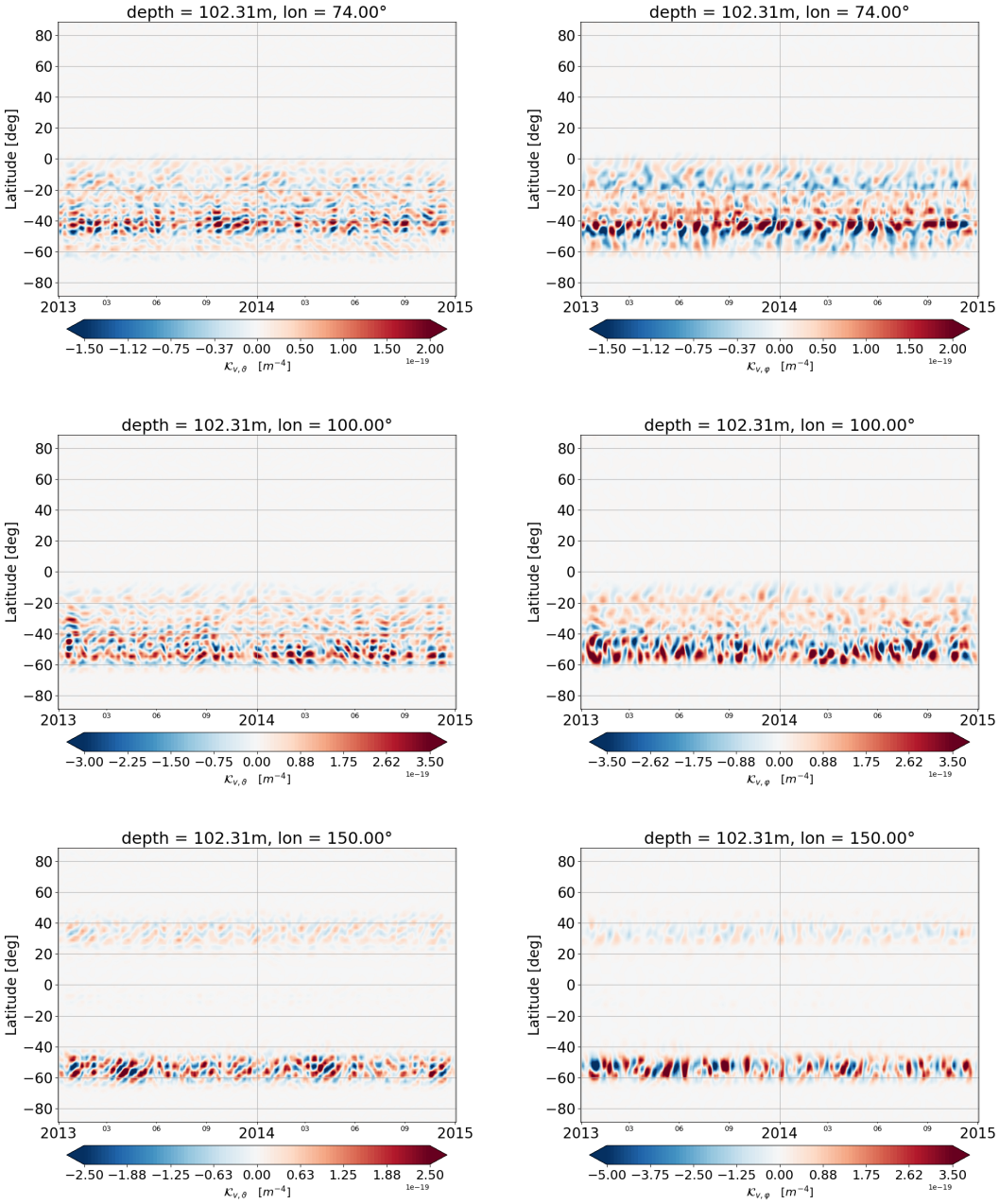


Figure 4.10 Latitude-time plot of sensitivity kernel $\mathcal{K}_{\mathbf{v}}$ at various longitudes, first part, left column is ϑ component and right column is φ component.

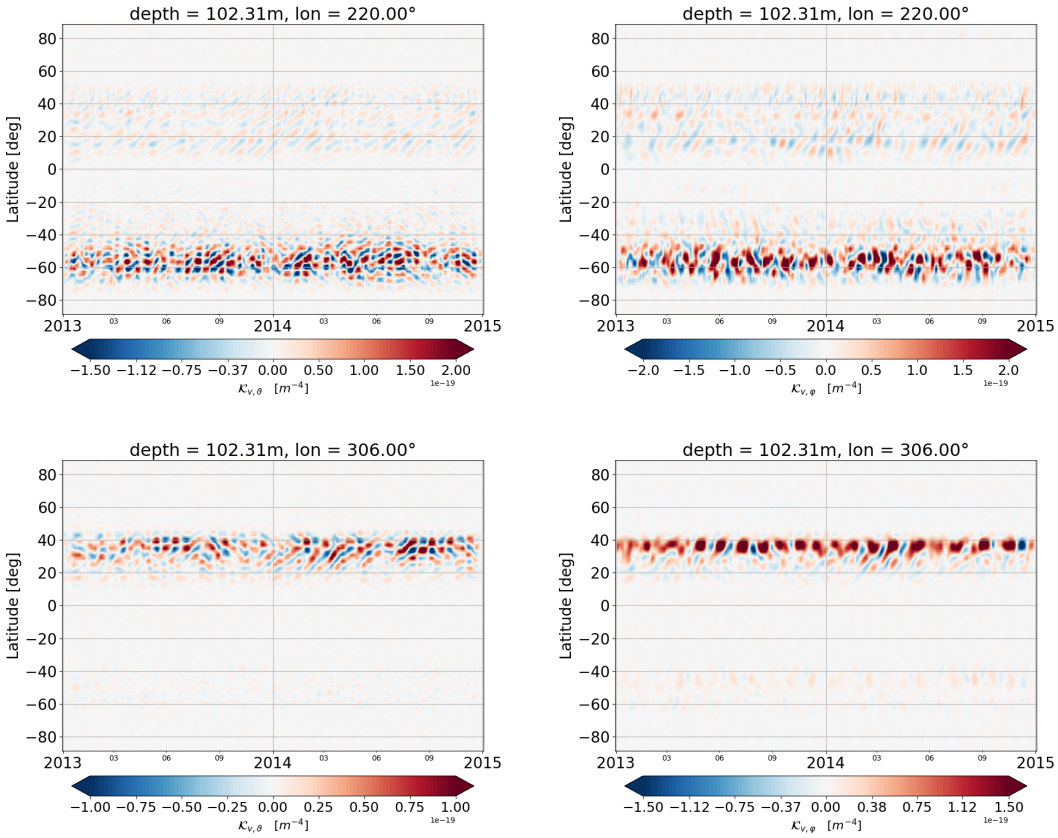


Figure 4.11 Latitude-time plot of sensitivity kernel $\mathcal{K}_{\mathbf{v}}$ at various longitudes, second part, left column is ϑ component and right column is φ component.

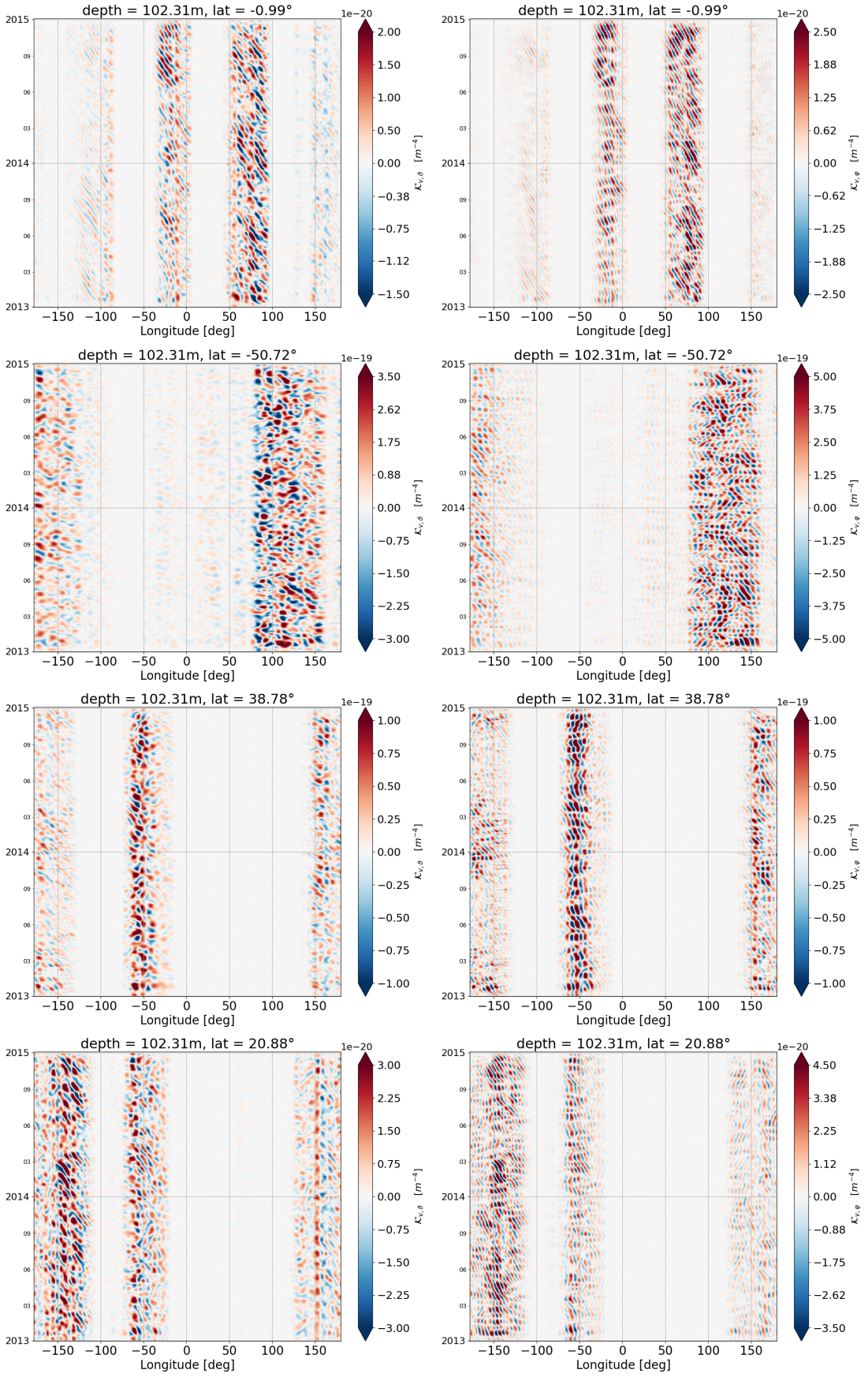


Figure 4.12 Longitude-time plot of sensitivity kernel $\mathcal{K}_{\mathbf{v}}$ at various latitudes, left column is ϑ component and right column is φ component.

Conclusion

The first task of this thesis was to understand the behaviour of the OIMF with the use of the PCA statistical tool in combination with the spatial and temporal filters. Even before the analysis itself, a *canonical* run was used to illustrate how filtering affects the data from a PCA perspective. This shows that, when filters are used appropriately, it is possible to highlight the features with the highest information content while suppressing those with low information content. Subsequently, these findings were used in an exploratory analysis of five comparison groups, which were selected to demonstrate how sensitive the OIMF model is to different model settings. Based on that, it was determined that ocean models, which incorporate both the ocean velocities and electrical conductivity, have the greatest impact on the final field, while the choice of the main field model is mostly arbitrary, as there is no noticeable difference between models. Inclusion of the laterally varying mantle conductivities also shows no major difference. In addition to explorative analysis, PCA can also used as an effective tool of parameterisation (Grüne, 2026). Seasonal variations are strongly pronounced in the principal components for the dominant modes across all models. Spatially, the dominant EOFs focus on the seasonal variations of the Indian Ocean current system and the variations of the Kuroshio current, which helps to focus the initial analysis of Swarm data (Finlay et al., 2026).

The next, and most important result of this thesis, is the derivation of the adjoint method to calculate the OIMF 4-D sensitivity kernels with respect to electrical conductivity (resistivity) and flow velocity. The inverse problem for the OIMF was formulated and then expanded upon the derivation of the adjoint problem from Maksimov and Velímský (2017) with the addition of the internal forcing and inclusion of 4-D climatology of the ocean velocities and electrical conductivities. The adjoint sensitivity kernels for the respective model parameters are obtained, implemented, and then presented on a simplified OIMF model with lower spatial resolution and shorter time span. A brief analysis of these kernels shows the greatest sensitivity in depth around 100 metres and in the areas of the ACC and Gulf stream. In addition to those two areas, the sensitivity kernel for the ocean velocities also shows noticeable values in the Indian ocean and the Kuroshio current and, in general, has greater sensitivity than the kernel for electrical conductivity.

The implementation of the sensitivity kernels is an important step towards future data assimilation of OIMF into ocean models. Preliminary analysis of the kernels implies that there is the possibility to recover some information on deeper parts of ocean dynamics. To get a better picture of the problem, more sophisticated and detailed analysis is needed. The issue of electrical conductivity kernel should also be approached, as there is yet no direct connection to the temperature and salinity. This leads to the non-uniqueness of the 4-D climatologies of temperature and salinity based on the electrical conductivity, which is problematic for the classic inverse problem. This ambiguity can be resolved only by the prior information from the ocean model. The use of depth-integrated quantities, such as ocean conductivity content or ocean conductivity transport, discussed in Trossman et al. (2024), should also be explored, as they can provide an alternative approach to the assimilation problem with reduced dimensionality.

Bibliography

Alken, Patrick et al., 2021. International geomagnetic reference field: The thirteenth generation. *Earth, Planets and Space*. Vol. 73, no. 1, p. 49.

Apel, John R, 2013. *Principles of ocean physics*. Vol. 38. Elsevier.

Boutin, Jacqueline et al., 2024. *ESA Sea Surface Salinity Climate Change Initiative: Weekly and monthly sea surface salinity products, v04.41, for 2010 to 2022*. NERC EDS Centre for Environmental Data Analysis. Available from doi: 10.5285/F2CA631F29A24C47A7E98654DDF2C7D9.

Butterworth, Stephen et al., 1930. On the theory of filter amplifiers. *Wireless Engineer*. Vol. 7, no. 6, pp. 536–541.

CMEMS., 2024. *Global Ocean Ensemble Physics Reanalysis*. Available from doi: 10.48670/moi-00024.

Dawson, Andrew, 2016. eofs: A library for EOF analysis of meteorological, oceanographic, and climate data. *Journal of Open Research Software*. Vol. 4, no. 1.

Desportes, C. et al., 2023. *Quality information document for GLOBAL REANALYSIS PHY 001 031*. Tech. rep. E.U. Copernicus Marine Service.

Einšpigel, D.; Martinec, Z., 2017. Time-domain modeling of global ocean tides generated by the full lunisolar potential. *Ocean Dynamics*. Vol. 67, no. 2, pp. 165–189.

Fichtner, Andreas, 2010. *Full seismic waveform modelling and inversion*. Springer Science & Business Media.

Finlay, Christopher C. et al., 2020. The CHAOS-7 geomagnetic field model and observed changes in the South Atlantic Anomaly. *Earth, Planets and Space*. Vol. 72, no. 1, p. 156.

Finlay, Christopher C. et al., 2024. Satellite monitoring of long period ocean-induced magnetic field variations. *Philosophical Transactions of the Royal Society A: Mathematical, Physical and Engineering Sciences*. Vol. 382, no. 2286, p. 20240077. issn 1364-503X. Available from doi: 10.1098/rsta.2024.0077.

Finlay, Christopher C. et al., 2026. Satellite observations of annual variations in the ocean-induced magnetic field from the tropical oceans. *JGR: Oceans*.

Forget, GAEL et al., 2015. ECCO version 4: An integrated framework for non-linear inverse modeling and global ocean state estimation. *Geoscientific Model Development*. Vol. 8, no. 10, pp. 3071–3104.

Fullea, J et al., 2021. WINTERC-G: mapping the upper mantle thermochemical heterogeneity from coupled geophysical–petrological inversion of seismic waveforms, heat flow, surface elevation and gravity satellite data. *Geophysical Journal International*. Vol. 226, no. 1, pp. 146–191.

Grayver, Alexander et al., 2024. Magnetic signals from oceanic tides: new satellite observations and applications. *Philosophical Transactions A*. Vol. 382, no. 2286, p. 20240078.

Grayver, Alexander V, 2021. Global 3-D electrical conductivity model of the world ocean and marine sediments. *Geochemistry, Geophysics, Geosystems*. Vol. 22, no. 9, e2021GC009950.

Grayver, Alexander V et al., 2017. Joint inversion of satellite-detected tidal and magnetospheric signals constrains electrical conductivity and water content of the upper mantle and transition zone. *Geophysical research letters*. Vol. 44, no. 12, pp. 6074–6081.

Grüne, Carla, 2026. *Inverse modelling of ocean-induced magnetic fields*. Inverse modelling of ocean-induced magnetic fields. Master of Science thesis (MSc.)–Technical University of Denmark, Division of Geomagnetism and Geospace, 2026.

Hannachi, A. et al., 2007. Empirical orthogonal functions and related techniques in atmospheric science: A review. *International Journal of Climatology*. Vol. 27, no. 9, pp. 1119–1152. Available from doi: https://doi.org/10.1002/joc.1499.

Ioc, Scor et al., 2010. The international thermodynamic equation of seawater–2010: Calculation and use of thermodynamic properties. *Intergovernmental Oceanographic Commission, UNESCO Manuals and Guides No*. Vol. 56, no. 203, p. 196.

Lellouche, J-M et al., 2013. Evaluation of global monitoring and forecasting systems at Mercator Océan. *Ocean Science*. Vol. 9, no. 1, pp. 57–81.

Lorenz, Edward N et al., 1956. *Empirical orthogonal functions and statistical weather prediction*. Vol. 1. Massachusetts Institute of Technology, Department of Meteorology Cambridge.

Madec, Gurvan et al., 2026. *NEMO Ocean Engine Reference Manual*. Zenodo. Version v5.0.1. Available from doi: 10.5281/zenodo.19206664.

Maksimov, M.A.; Velímský, J., 2017. Fast calculations of the gradient and the Hessian in the time-domain global electromagnetic induction inverse problem. *Geophysical Journal International*. Vol. 210, no. 1, pp. 270–283. issn 0956-540X. Available from doi: 10.1093/gji/ggx167.

Martin, Matthew J et al., 2024. Data assimilation schemes for ocean forecasting: state of the art. *State of the Planet Discussions*. Vol. 2024, pp. 1–16.

Martinec, Z. et al., 2021. A new integrated geophysical-petrological global 3-D model of upper-mantle electrical conductivity validated by the Swarm M 2 tidal magnetic field. *Geophysical Journal International*. Vol. 226, no. 2, pp. 742–763.

Menemenlis, Dimitris et al., 2005. Using Green's functions to calibrate an ocean general circulation model. *Monthly weather review*. Vol. 133, no. 5, pp. 1224–1240.

Menemenlis, Dimitris et al., 2008. ECCO2: High resolution global ocean and sea ice data synthesis. *Mercator Ocean Quarterly Newsletter*. Vol. 31, no. October, pp. 13–21.

Millero, Frank J, 2010. History of the equation of state of seawater. *Oceanography*. Vol. 23, no. 3, pp. 18–33.

Millero, Frank J et al., 2008. The composition of Standard Seawater and the definition of the Reference-Composition Salinity Scale. *Deep Sea Research Part I: Oceanographic Research Papers*. Vol. 55, no. 1, pp. 50–72.

Pearson, Karl, 1901. LIII. On lines and planes of closest fit to systems of points in space. *The London, Edinburgh, and Dublin Philosophical Magazine and Journal of Science*. Vol. 2, no. 11, pp. 559–572. Available from doi: 10.1080/14786440109462720.

Šachl, Libor et al., 2019. Modelling of electromagnetic signatures of global ocean circulation: physical approximations and numerical issues. *Earth, Planets and Space*. Vol. 71, no. 1, p. 58.

Savitzky, Abraham; Golay, Marcel JE, 1964. Smoothing and differentiation of data by simplified least squares procedures. *Analytical chemistry*. Vol. 36, no. 8, pp. 1627–1639.

Siedler, Gerold et al., 2013. *Ocean circulation and climate: a 21st century perspective*. Vol. 103. Academic Press.

Storto, Andrea et al., 2016. Evaluation of the CMCC eddy-permitting global ocean physical reanalysis system (C-GLORS, 1982–2012) and its assimilation components. *Quarterly Journal of the Royal Meteorological Society*. Vol. 142, no. 695, pp. 738–758.

Tarantola, Albert, 2005. *Inverse problem theory and methods for model parameter estimation*. SIAM.

Trossman, David S et al., 2024. Physical oceanographic factors controlling the ocean circulation-induced magnetic field. *Philosophical Transactions A*. Vol. 382, no. 2286, p. 20240076.

Tyler, Robert H et al., 2003. Satellite observations of magnetic fields due to ocean tidal flow. *Science*. Vol. 299, no. 5604, pp. 239–241.

Ucekajová, Veronika, 2025. *Magnetic field in oceans: Parametric study and visualisation*. Magnetic field in oceans: Parametric study and visualisation. Bakalářská práce (Bc.)–Univerzita Karlova. Matematicko-fyzikální fakulta, 2025.

Varshalovich, D. A. (Dmitrii Aleksandrovich), 1989. *Quantum theory of angular momentum : Irreducible tensors, spherical harmonics, vector coupling coefficients 3 nj symbols*. Quantum theory of angular momentum : Irreducible tensors, spherical harmonics, vector coupling coefficients 3 nj symbols. Singapore ; World Scientific Pub. isbn 981-4415-49-9.

Velímský, Jakub, 2013. Determination of three-dimensional distribution of electrical conductivity in the Earth's mantle from Swarm satellite data: Time-domain approach. *Earth, Planets and Space*. Vol. 65, no. 11, pp. 1239–1246.

Velímský, Jakub, 2025. Chapter Two - Electromagnetic induction in the Earth's mantle and oceans: A spherical-harmonic approach. In: Schmelzbach, Cedric et al. (eds.). *Electromagnetic Methods: Theory and Applications*. Elsevier. Vol. 66, pp. 23–67. Advances in Geophysics. issn 0065-2687. Available from doi: https://doi.org/10.1016/bs.agph.2025.06.004.

Velímský, Jakub et al., 2019. The global toroidal magnetic field generated in the Earth's oceans. *Earth and Planetary Science Letters*. Vol. 509, pp. 47–54.

Von Schuckmann, Karina et al., 2016. The copernicus marine environment monitoring service ocean state report. *Journal of Operational Oceanography*. Vol. 9, no. sup2, s235–s320.

Zuo, Hao et al., 2017. A generic ensemble generation scheme for data assimilation and ocean analysis. *ECMWF Technical Memoranda*.

List of Figures

1.1 Snapshot of Sea Surface Salinity from 15-12-2024. Generated using EU Copernicus Marine Service Information; 10.48670/moi-00051 . 7
1.2 A simple scheme of the Global Conveyor Belt. Red indicates warm water and blue indicates cold water. Figure by Brisbane, CC BY-SA 3.0, via Wikimedia Commons. 9
1.3 A simplified, not to scale, cartoon depicting major near-Earth electrical current systems that contribute to Earth's magnetic field. Taken from Finlay et al. (2024). 10

3.1 Fraction of total variance described by each mode. Shown for the SH degree range of 1 - 240, 1 - 60, 1 - 30, 1 - 19, and 19 - 30. . . . 21
3.2 PCs of all used SH degree ranges. 23
3.3 Lowes-Mauersberger power spectrum for unfiltered signal and bandpass- filtered signal at selected periods. 24
3.4 Fraction of total variance described by each mode. 25
3.5 EOFs for the first group of bands. 26
3.6 EOFs for the second group of bands. 27
3.7 Fraction of total variance described by each mode, ocean runs. . . 28
3.8 First modes of runs with different ocean models. 29
3.9 Second modes of runs with different ocean models. 30
3.10 Fraction of total variance described by each mode, main field runs. 31
3.11 First modes of runs with different main field models. 32
3.12 Second modes of runs with different main field models. 33
3.13 Fraction of total variance described by each mode, comparison of lateral resolution. 33
3.14 First modes of runs with different lateral resolution. 34
3.15 Second modes of runs with different lateral resolution. 34
3.16 First five PCs comparing run 6 and run 9 36
3.17 Fraction of total variance described by each mode, mantle runs. . 37
3.18 First modes of runs with different mantle models. 37
3.19 Second modes of runs with different mantle models. 38

4.1 Original Gauss coefficients and their filtered variant, $j = 1$ and $m = 0$. 44
4.2 Chosen locations to showcase figures at the specific geographical coordinates. 45
4.3 Depth-time plot of sensitivity kernel $\mathcal{K}_\rho$ at various geographical points. 46
4.4 Time average of the sensitivity kernel $\mathcal{K}_\rho$ at depth 102.31 m. . . 47
4.5 Latitude-time plot of sensitivity kernel $\mathcal{K}_\rho$ at depth 102.31 m at various longitudes. 48
4.6 Longitude-time plot of sensitivity kernel $\mathcal{K}_\rho$ at depth 102.31 m at various latitudes. 49
4.7 Depth-time plot of sensitivity kernel $\mathcal{K}_\mathbf{v}$ at various geographical points, ϑ component. 50

4.8 Depth-time plot of sensitivity kernel $\mathcal{K}_{\mathbf{v}}$ at various geographical points, φ component. 51
4.9 Time average of the sensitivity kernel $\mathcal{K}_{\mathbf{v}}$ at depth 102.31 m. . . . 52
4.10 Latitude-time plot of sensitivity kernel $\mathcal{K}_{\mathbf{v}}$ at various longitudes, first part, left column is ϑ component and right column is φ component. 53
4.11 Latitude-time plot of sensitivity kernel $\mathcal{K}_{\mathbf{v}}$ at various longitudes, second part, left column is ϑ component and right column is φ component. 54
4.12 Longitude-time plot of sensitivity kernel $\mathcal{K}_{\mathbf{v}}$ at various latitudes, left column is ϑ component and right column is φ component. . . 55

List of Tables

1.1 Overview of characteristics of various geomagnetic fields. 11

2.1 Run configurations: Ocean Model, Sediments, Mantle, and Main Field. All model parameteres are described in their respective subsections. 13
2.2 Run configurations: numerical parameters and time spans. . . . 15

3.1 Cross-correlation between PCs of coefficients with full range of degrees (1 - 240) and PCs of coefficients with various ranges of degrees. Used modes are numbered in the first column and SH degree ranges are in the first row. Comparing the overall variances of other ranges with the range of 1 - 240: (1 - 60) has 78% of the original total variance, (1 - 30) has 60%, (1 - 19) has 48%, and (19 - 30) has only 12%. 21
3.2 Cross-correlation between EOFs of coefficients with no bandpass applied and EOFs of coefficients with various bands. Used modes are numbered in the first column and used bands are in the first row. Comparing the overall variances of other bands with no band: band [0, 30] days has 38% of original total variance, band [30, 1800] has 59%, and [1800, 5400] has only 6%. 22
3.3 Cross-correlation between EOFs of coefficients with no bandpass applied and EOFs of coefficients with various bands. Used modes are numbered in the first column and used bands are in the first row. Comparing the overall variances of other bands with no band: band [30, 120] has 15%, band [120, 240] has 9%, band [240, 540] has 17% and [540, 1800] has 7%. 24

List of Abbreviations

Abbreviation	Full name
EMI	electromagnetic induction
OIMF	ocean-induced magnetic field
TIMF	tidal-induced magnetic field
SSS	sea surface salinity
SST	sea surface temperature
SSH	sea surface height
ACC	Antarctic circumpolar current
AMOC	Atlantic meridional overturning circulation
SfOD	Swarm for Ocean Dynamics
CMEMS	Copernicus Marine Environment Monitoring Service
NEMO	Nucles for European Modelling of the Ocean
ECCO	Estimating the Circulation and Climate of the Ocean
IGRF13	13th International Geomagnetic Reference Field
SSS-CCI	Sea Surface Salinity Climate Change Initiative
PCA	principal component analysis
PC	principal component
EOF	empirical orthogonal function
SVD	singular value decomposition

A Attachments

A.1 Spherical harmonic functions

In this appendix, the real, fully normalised spherical harmonic scalar and vector functions are defined, analogous to their complex counterparts in Varshalovich, 1989.

The scalar spherical harmonic function is defined as

$$Y_{jm}(\Omega) = \begin{cases} (-1)^m\sqrt{2}\sqrt{\frac{2j+1}{4\pi}\frac{(j-m)!}{(j+m)!}}P_j^m(\cos\vartheta)\cos(m\varphi) & ,\ m>0 \\ \sqrt{\frac{2j+1}{4\pi}}P_j^0(\cos\vartheta) & ,\ m=0 \\ (-1)^m\sqrt{2}\sqrt{\frac{2j+1}{4\pi}\frac{(j-|m|)!}{(j+|m|)!}}P_j^{|m|}(\cos\vartheta)\sin(|m|\varphi) & ,\ m<0 \end{cases} \tag{A.1}$$

where j is the degree, m is the order, $|m|<j$, $\Omega=(\vartheta,\varphi)$ and $P_j^m(\cos\vartheta)$ are the associated Legendre polynomials

$$P_j^m(\cos\vartheta) = (-\sin\vartheta)^m\frac{d^m}{(d\cos\vartheta)^m}P_j(\cos\vartheta). \tag{A.2}$$

The functions $Y_{jm}(\Omega)$ are orthonormal in a unit sphere

$$\int_\Omega Y_{jm}(\Omega)Y_{j'm'}(\Omega)d\Omega = \delta_{jj'}\delta_{mm'}. \tag{A.3}$$

With the radial unit vector $\mathbf{e}_r$ and the angular gradient operator ∇_Ω, the following vectors are constructed,

$$\mathbf{S}_{jm}^{(-1)}(\Omega) = Y_{jm}(\Omega)\mathbf{e}_r, \tag{A.4}$$

$$\mathbf{S}_{jm}^{(0)}(\Omega) = \mathbf{e}_r\times\nabla_\Omega Y_{jm}(\Omega), \tag{A.5}$$

$$\mathbf{S}_{jm}^{(1)}(\Omega) = \nabla_\Omega Y_{jm}(\Omega). \tag{A.6}$$

They, respectively, describe the vertical poloidal-scaloidal, the toroidal, and horizontal poloidal-scaloidal components of a vector field and satisfy relations

$$\mathbf{e}_r\times\mathbf{S}_{jm}^{(-1)}(\Omega) = \mathbf{0}, \tag{A.7}$$

$$\mathbf{e}_r\times\mathbf{S}_{jm}^{(0)}(\Omega) = -\mathbf{S}_{jm}^{(1)}(\Omega), \tag{A.8}$$

$$\mathbf{e}_r\times\mathbf{S}_{jm}^{(1)}(\Omega) = \mathbf{S}_{jm}^{(0)}(\Omega). \tag{A.9}$$

These vectors are orthogonal on a unit sphere,

$$\int_\Omega \mathbf{S}_{jm}^{(\lambda)}(\Omega)\mathbf{S}_{j'm'}^{(\lambda')}(\Omega)d\Omega = \delta_{jj'}\delta_{mm'}\delta_{\lambda\lambda'}\left[\delta_{-1\lambda}+j(j+1)(1-\delta_{-1\lambda})\right]. \tag{A.10}$$

Spherical harmonic functions are often used for the decomposition of scalar or vector fields. The real valued scalar field $f(\mathbf{r},t)$ is decomposed with scalar spherical harmonic functions,

$$f(\mathbf{r},t) = \sum_{j=0}^{\infty}\sum_{m=-j}^{j} f_{jm}(r,t)Y_{jm}(\Omega), \tag{A.11}$$

and the real valued vector field $\mathbf{F}(\mathbf{r},t)$ is decomposed with vector spherical harmonic functions,

$$\mathbf{F}(\mathbf{r},t)=\sum_{j=0}^{\infty}\sum_{m=-j}^{j}\sum_{\lambda=-1}^{1}F_{jm}^{(\lambda)}(r,t)\mathbf{S}_{jm}^{(\lambda)}(\Omega) \tag{A.12}$$

The spherical harmonic functions interact with vector operators. For an arbitrary, sufficiently smooth function $f(r)$ holds:

Gradient operator:

$$\nabla[f(r)Y_{jm}(\Omega)]=\frac{df(r)}{dr}\mathbf{S}_{jm}^{(-1)}+\frac{f(r)}{r}\mathbf{S}_{jm}^{(1)}. \tag{A.13}$$

Divergence operator:

$$\nabla\cdot[f(r)\mathbf{S}_{jm}^{(-1)}(\Omega)]=\left(\frac{d}{dr}+\frac{2}{r}\right)f(r)Y_{jm}(\Omega) \tag{A.14}$$

$$\nabla\cdot[f(r)\mathbf{S}_{jm}^{(0)}(\Omega)]=0 \tag{A.15}$$

$$\nabla\cdot[f(r)\mathbf{S}_{jm}^{(1)}(\Omega)]=-j(j+1)\frac{f(r)}{r}Y_{jm}(\Omega) \tag{A.16}$$

Rotation operator:

$$\nabla\times[f(r)\mathbf{S}_{jm}^{(-1)}(\Omega)]=-\frac{f(r)}{r}\mathbf{S}_{jm}^{(-1)}(\Omega) \tag{A.17}$$

$$\nabla\times[f(r)\mathbf{S}_{jm}^{(0)}(\Omega)]=-j(j+1)\frac{f(r)}{r}\mathbf{S}_{jm}^{(-1)}(\Omega)-\left(\frac{d}{dr}+\frac{2}{r}\right)f(r)\mathbf{S}_{jm}^{(1)}(\Omega) \tag{A.18}$$

$$\nabla\times[f(r)\mathbf{S}_{jm}^{(1)}(\Omega)]=\left(\frac{d}{dr}+\frac{2}{r}\right)\mathbf{S}_{jm}^{(0)}(\Omega) \tag{A.19}$$

$$\tag{A.20}$$

A.2 Adjoint problem

The following relations from Maksimov and Velímský (2017) are used in the derivation:

- relation between time and adjoint time

$$\frac{\partial(\cdot)}{\partial\hat{t}}=-\frac{\partial(\cdot)}{\partial t} \tag{A.21}$$

- corollary of the divergence theorem

$$\int_G\mathbf{g}\cdot(\nabla\times\mathbf{f})dV=\int_G\mathbf{f}\cdot(\nabla\times\mathbf{g})dV+\int_{\partial G}(\mathbf{f}\times\mathbf{g})\cdot\mathbf{e}_r dS \tag{A.22}$$

- combination of Ampere's law and Ohm's law, introducing the electric field $\mathbf{E}$,

$$\rho(\nabla\times\mathbf{B})=\mu_0(\mathbf{E}+\mathbf{v}\times\mathbf{B}_C) \tag{A.23}$$

- Lorentz force

$$\mathbf{F}_L = \mathbf{v} \times \mathbf{B}_C \tag{A.24}$$

- boundary condition in the spherical harmonic expansion

$$B_{jm}^{(0)}(a,t) = 0 \tag{A.25}$$

$$B_{jm}^{(-1)}(a,t) = -\left[jG_{jm}^{(e)}(t) - (j+1)G_{jm}^{(i)}(t)\right] \tag{A.26}$$

$$B_{jm}^{(1)}(a,t) = -\left[G_{jm}^{(e)}(t) + G_{jm}^{(i)}(t)\right] \tag{A.27}$$

Vector fields $\mathbf{B}, \mathbf{E}, \mathbf{F}_L$ have their adjoint variant, denoted by the addition of the hat symbol to the variable. They satisfy the adjoint Maxwell equations, obtained by replacing t with $\hat{t}$ in the time derivatives. Spherical harmonic decompositions and mentioned relations also holds for adjoint variants.

Derivation of the adjoint problem

The first step of the derivation is to apply operator $D_{\mathbf{m}}$ in equation (2.1), multiplying it by $\hat{\mathbf{B}}$, and integrating over G and T, which gives us the following integral

$$\mathcal{I} = \int_0^{t_1} \int_G \hat{\mathbf{B}} \cdot D_{\mathbf{m}} \left(\frac{\partial \mathbf{B}}{\partial t} + \frac{1}{\mu_0} \nabla \times (\rho \nabla \times \mathbf{B}) - \nabla \times \mathbf{F}_L \right) dV dt = 0, \tag{A.28}$$

$$\mathcal{I} = \mathcal{I}_1 + \mathcal{I}_2 + \mathcal{I}_3 = 0, \tag{A.29}$$

where

$$\mathcal{I}_1 = \int_0^{t_1} \int_G \hat{\mathbf{B}} \cdot D_{\mathbf{m}} \frac{\partial \mathbf{B}}{\partial t} dV dt, \tag{A.30}$$

$$\mathcal{I}_2 = \frac{1}{\mu_0} \int_0^{t_1} \int_G \hat{\mathbf{B}} \cdot D_{\mathbf{m}} \left(\nabla \times (\rho \nabla \times \mathbf{B}) \right) dV dt, \tag{A.31}$$

$$\mathcal{I}_3 = -\int_0^{t_1} \int_G \hat{\mathbf{B}} \cdot D_{\mathbf{m}} \left(\nabla \times \mathbf{F}_L \right) dV dt. \tag{A.32}$$

The aim of this derivation is to get an integral expression in the form of

$$\int_0^{t_1} \int_G D_{\mathbf{m}} \mathbf{B} \cdot [\cdots] \, dV dt = 0. \tag{A.33}$$

Starting with the first term $\mathcal{I}_1$, using integration by parts, and then applying relation (A.21)

$$\begin{aligned} \mathcal{I}_1 &= \left[\int_G \hat{\mathbf{B}}(\hat{t}) D_{\mathbf{m}} \mathbf{B}(t) dV \right]_{t=0}^{t=t_1} - \int_0^{t_1} \int_G \frac{\partial \hat{\mathbf{B}}}{\partial t} \cdot D_{\mathbf{m}} \mathbf{B} dV dt \\ &= \left[\int_G \hat{\mathbf{B}}(\hat{t}) D_{\mathbf{m}} \mathbf{B}(t) dV \right]_{t=0}^{t=t_1} + \int_0^{t_1} \int_G \frac{\partial \hat{\mathbf{B}}}{\partial \hat{t}} \cdot D_{\mathbf{m}} \mathbf{B} dV dt, \end{aligned} \tag{A.34}$$

where setting the initial condition $\hat{\mathbf{B}}(t_1) = \hat{\mathbf{B}}(\hat{0}) = \mathbf{0}$ and assuming that the initial condition of the forward problem is parameter independent $D_{\mathbf{m}} \mathbf{B}(\mathbf{r}, 0) = D_{\mathbf{m}} \mathbf{B}_0(\mathbf{r}) = \mathbf{0}$, (A.34) simplifies to

$$\mathcal{I}_1 = \int_0^{t_1} \int_G \hat{\mathbf{B}} \cdot \frac{\partial D_{\mathbf{m}} \mathbf{B}}{\partial t} dV dt = \int_0^{t_1} \int_G \frac{\partial \hat{\mathbf{B}}}{\partial \hat{t}} \cdot D_{\mathbf{m}} \mathbf{B} dV dt. \tag{A.35}$$

Let us continue with the second term $\mathcal{I}_2$. Firstly, we apply (A.22) with (A.23) on the integral term of the surface and apply $D_{\mathbf{m}}$ on the integral with $\rho\nabla\times\mathbf{B}$

$$\begin{aligned}\mathcal{I}_2 = \mathcal{I}_\rho + \mathcal{I}_{2a} + \mathcal{I}_{2b} &= \frac{1}{\mu_0}\int_0^{t_1}\int_G D_{\mathbf{m}_\alpha}\rho\nabla\times\hat{\mathbf{B}}\cdot\nabla\times\mathbf{B}dVdt \\ &+ \frac{1}{\mu_0}\int_0^{t_1}\int_G \rho\nabla\times\hat{\mathbf{B}}\cdot D_{\mathbf{m}}\left(\nabla\times\mathbf{B}\right)dVdt \\ &+ \int_0^{t_1}\int_{\partial G}\left[D_{\mathbf{m}}\left(\mathbf{F}_L+\mathbf{E}\right)\times\hat{\mathbf{B}}\right]\cdot\mathbf{e}_r dSdt,\end{aligned} \tag{A.36}$$

The vector identity is then applied on $\mathcal{I}_{2a}$ with adjoint variant of (A.23) on the surface integral

$$\begin{aligned}\mathcal{I}_{2a} = \mathcal{I}_{2'} + \mathcal{I}_{2a'} &= \frac{1}{\mu_0}\int_0^{t_1}\int_G \nabla\times(\rho\nabla\times\hat{\mathbf{B}})\cdot D_{\mathbf{m}}\mathbf{B}dVdt \\ &+ \int_0^{t_1}\int_{\partial G}\left[D_{\mathbf{m}}\mathbf{B}\times(\hat{\mathbf{F}}_L+\hat{\mathbf{E}})\right]\cdot\mathbf{e}_r dSdt.\end{aligned} \tag{A.37}$$

Rewriting the surface integrals $\mathcal{I}_{2c}$ and $\mathcal{I}_{2b''}$ so that the electric fields $\mathbf{E},\hat{\mathbf{E}}$ and the Lorentz force $\mathbf{F}_L,\hat{\mathbf{F}}_L$ are separated

$$\begin{aligned}\mathcal{I}_{2b}+\mathcal{I}_{2a'} &= \int_0^{t_1}\int_{\partial G}\left[D_{\mathbf{m}}\mathbf{B}\times\hat{\mathbf{E}} + D_{\mathbf{m}}\mathbf{E}\times\hat{\mathbf{B}}\right]\cdot\mathbf{e}_r dSdt \\ &+ \int_0^{t_1}\int_{\partial G}\left[D_{\mathbf{m}}\mathbf{B}\times\hat{\mathbf{F}}_L + D_{\mathbf{m}}\mathbf{F}_L\times\hat{\mathbf{B}}\right]\cdot\mathbf{e}_r dSdt = \mathcal{I}_E+\mathcal{I}_L.\end{aligned} \tag{A.38}$$

Applying decomposition (A.12) and using the property of spherical harmonics (A.7)-(A.9), the surface integral $\mathcal{I}_E$ can be rewritten as

$$\begin{aligned}\mathcal{I}_E &= \int_0^{t_1}\int_{\partial G}\left[D_{\mathbf{m}}\mathbf{B}\times\hat{\mathbf{E}} + D_{\mathbf{m}}\mathbf{E}\times\hat{\mathbf{B}}\right]\cdot\mathbf{e}_r dSdt \\ &= a^2\sum_{jm} j(j+1)\int_0^{t_1}\Big[\hat{B}^{(0)}_{jm}(a,\hat{t})D_{\mathbf{m}}E^{(1)}_{jm}(a,t) - \hat{B}^{(1)}_{jm}(a,\hat{t})D_{\mathbf{m}}E^{(0)}_{jm}(a,t) \\ &\quad - \hat{E}^{(1)}_{jm}(a,\hat{t})D_{\mathbf{m}}B^{(0)}_{jm}(a,t) + \hat{E}^{(0)}_{jm}(a,\hat{t})D_{\mathbf{m}}B^{(1)}_{jm}(a,t)\Big]dt.\end{aligned} \tag{A.39}$$

As a result of the boundary condition, the toroidal magnetic field is zero at surface

$$B^{(0)}_{jm}(a,t) = 0 \implies D_{\mathbf{m}}B^{(0)}_{jm}(a,t) = 0, \tag{A.40}$$

which also holds for the adjoint magnetic field $\hat{\mathbf{B}}$, surface integral $\mathcal{I}_E$ is now

$$\mathcal{I}_E = a^2\sum_{jm} j(j+1)\int_0^{t_1}\left[-\hat{B}^{(1)}_{jm}(a,\hat{t})D_{\mathbf{m}}E^{(0)}_{jm}(a,t) + \hat{E}^{(0)}_{jm}(a,\hat{t})D_{\mathbf{m}}B^{(1)}_{jm}(a,t)\right]dt. \tag{A.41}$$

Radial component of Faraday's law, expressed in spherical harmonic expansion,

$$\frac{j(j+1)}{r}E^{(0)}_{jm}(r,t) = \frac{\partial B^{(-1)}_{jm}(r,t)}{\partial t}, \tag{A.42}$$

which again holds for the adjoint variants, can be substituted into (A.41) and then integrating by parts in time leads to

$$\begin{aligned}\mathcal{I}_E &= a^3 \sum_{jm} \int_0^{t_1} \left[-\hat{B}_{jm}^{(1)}(a,\hat{t}) D_{\mathbf{m}} \frac{\partial B_{jm}^{(-1)}(a,t)}{\partial t} + \frac{\partial \hat{B}_{jm}^{(-1)}(a,\hat{t})}{\partial \hat{t}} D_{\mathbf{m}} B_{jm}^{(1)}(a,t) \right] dt \\ &= a^3 \sum_{jm} \int_0^{t_1} \left[-\frac{\partial \hat{B}_{jm}^{(1)}(a,\hat{t})}{\partial \hat{t}} D_{\mathbf{m}} B_{jm}^{(-1)}(a,t) + \frac{\partial \hat{B}_{jm}^{(-1)}(a,\hat{t})}{\partial \hat{t}} D_{\mathbf{m}} B_{jm}^{(1)}(a,t) \right] dt \\ &\quad - a^3 \sum_{jm} \left[\hat{B}_{jm}^{(1)}(a,\hat{t}) D_{\mathbf{m}} B_{jm}^{(-1)}(a,t) \right]_{t=0}^{t=t_1},\end{aligned} \tag{A.43}$$

where the last term equals zero, due to the initial condition and parameter independence. Following the boundary conditions (A.26)-(A.27) and taking into account that the external Gauss coefficients are parameter-independent

$$D_{\mathbf{m}} G_{jm}^{(e)}(t) = 0, \tag{A.44}$$

the surface integral $\mathcal{I}_E$ can be written in the final form as

$$\begin{aligned}\mathcal{I}_E &= a^3 \sum_{jm} \int_0^{t_1} \left[-\left(\frac{\partial \hat{G}_{jm}^{(e)}}{\partial \hat{t}} + \frac{\partial \hat{G}_{jm}^{(i)}}{\partial \hat{t}} \right) \left(j D_{\mathbf{m}} G_{jm}^{(e)}(t) - (j+1) D_{\mathbf{m}} G_{jm}^{(i)}(t) \right) \right. \\ &\quad \left. + \left(j \frac{\partial \hat{G}_{jm}^{(e)}}{\partial \hat{t}} - (j+1) \frac{\partial \hat{G}_{jm}^{(i)}}{\partial \hat{t}} \right) \left(D_{\mathbf{m}} G_{jm}^{(e)}(t) + D_{\mathbf{m}} G_{jm}^{(i)}(t) \right) \right] dt \\ &= a^3 \sum_{jm} \int_0^{t_1} (2j+1) \frac{\partial \hat{G}_{jm}^{(e)}}{\partial \hat{t}} D_{\mathbf{m}} G_{jm}^{(i)}(t) dt.\end{aligned} \tag{A.45}$$

For the final term $\mathcal{I}_3$, (A.22) is applied

$$\mathcal{I}_3 = -\int_0^{t_1} \int_G \nabla \times \hat{\mathbf{B}} \cdot D_{\mathbf{m}} \mathbf{F}_L dV dt - \int_0^{t_1} \int_{\partial G} \left[D_{\mathbf{m}} \mathbf{F}_L \times \hat{\mathbf{B}} \right] \cdot \mathbf{e}_r dS dt, \tag{A.46}$$

combining with the surface integral $\mathcal{I}_L$

$$\begin{aligned}\mathcal{I}_3 + \mathcal{I}_L &= -\int_0^{t_1} \int_G \nabla \times \hat{\mathbf{B}} \cdot D_{\mathbf{m}} \mathbf{F}_L dV dt - \int_0^{t_1} \int_{\partial G} \left[D_{\mathbf{m}} \mathbf{F}_L \times \hat{\mathbf{B}} \right] \cdot \mathbf{e}_r dS dt \\ &\quad + \int_0^{t_1} \int_{\partial G} \left[D_{\mathbf{m}} \mathbf{B} \times \hat{\mathbf{F}}_L + D_{\mathbf{m}} \mathbf{F}_L \times \hat{\mathbf{B}} \right] \cdot \mathbf{e}_r dS dt \\ &= -\int_0^{t_1} \int_G \nabla \times \hat{\mathbf{B}} \cdot D_{\mathbf{m}} \mathbf{F}_L dV dt + \int_0^{t_1} \int_{\partial G} \left[D_{\mathbf{m}} \mathbf{B} \times \hat{\mathbf{F}}_L \right] \cdot \mathbf{e}_r dS dt = \mathcal{I}_v,\end{aligned} \tag{A.47}$$

setting the adjoint Lorentz force $\hat{\mathbf{F}}_L = \mathbf{0}$, we arrive at

$$\mathcal{I}_v = -\int_0^{t_1} \int_G \nabla \times \hat{\mathbf{B}} \cdot D_{\mathbf{m}} \mathbf{F}_L dV dt = \int_0^{t_1} \int_G D_{\mathbf{m}_\beta} \mathbf{v} \cdot \left[(\nabla \times \hat{\mathbf{B}}) \times \mathbf{B}_C \right] dV dt, \tag{A.48}$$

where $\mathbf{F}_L$ was substituted with (A.24) and the vectors were reorganised.

Returning to the original integral expression

$$\begin{aligned}\mathcal{I} &= \mathcal{I}_1 + \mathcal{I}_{2'} + \mathcal{I}_\rho + \mathcal{I}_v + \mathcal{I}_E \\ &= \int_0^{t_1}\int_G \left[\frac{\partial \hat{\mathbf{B}}}{\partial \hat{t}} + \frac{1}{\mu_0}\nabla\times\left(\rho\nabla\times\hat{\mathbf{B}}\right)\right]\cdot D_{\mathbf{m}}\mathbf{B}dVdt \\ &\quad + \int_0^{t_1}\int_G \left[\frac{1}{\mu_0}D_{\mathbf{m}_\alpha}\rho\nabla\times\hat{\mathbf{B}}\cdot\nabla\times\mathbf{B} + D_{\mathbf{m}_\beta}\mathbf{v}\cdot\left((\nabla\times\hat{\mathbf{B}})\times\mathbf{B}_C\right)\right]dVdt \\ &\quad + a^3\sum_{jm}\int_0^{t_1}(2j+1)\frac{\partial \hat{G}^{(e)}_{jm}}{\partial \hat{t}}D_{\mathbf{m}}G^{(i)}_{jm}(t)dt.\end{aligned} \tag{A.49}$$

As $\mathcal{I}=0$, it can be added to misfit gradient (4.21)

$$\begin{aligned}D_{\mathbf{m}}\chi^2 &= D_{\mathbf{m}}\chi^2 + \frac{1}{4\pi a^3}\mathcal{I} \\ &= \frac{1}{4\pi a^3}\int_0^{t_1}\int_G \left[\frac{1}{\mu_0}D_{\mathbf{m}_\alpha}\rho\nabla\times\hat{\mathbf{B}}\cdot\nabla\times\mathbf{B} + D_{\mathbf{m}_\beta}\mathbf{v}\cdot\left((\nabla\times\hat{\mathbf{B}})\times\mathbf{B}_C\right)\right]dVdt \\ &\quad + \frac{1}{4\pi a^3}\int_0^{t_1}\int_G \left[\frac{\partial \hat{\mathbf{B}}}{\partial \hat{t}} + \frac{1}{\mu_0}\nabla\times\left(\rho\nabla\times\hat{\mathbf{B}}\right)\right]\cdot D_{\mathbf{m}}\mathbf{B}dVdt \\ &\quad + \sum_{jm}\frac{2j+1}{4\pi}\int_0^{t_1}\left[\frac{j+1}{t_1}\frac{G^{(i)}_{jm}(t)-G^{(i,obs)}_{jm}(t)}{(\delta^{(i)}_{jm})^2} + \frac{\partial \hat{G}^{(e)}_{jm}}{\partial \hat{t}}\right]D_{\mathbf{m}}G^{(i)}_{jm}(t)dt.\end{aligned} \tag{A.50}$$

By solving equations

$$\frac{\partial \hat{\mathbf{B}}}{\partial \hat{t}} + \frac{1}{\mu_0}\nabla\times\left(\rho\nabla\times\hat{\mathbf{B}}\right) = \mathbf{0}, \tag{A.51}$$

with initial condition $\hat{\mathbf{B}}(t_1) = \hat{\mathbf{B}}(\hat{0}) = \mathbf{0}$, and

$$\begin{aligned}\frac{\partial \hat{G}^{(e)}_{jm}}{\partial \hat{t}} &= -\frac{j+1}{t_1}\frac{G^{(i)}_{jm}(t)-G^{(i,obs)}_{jm}(t)}{(\delta^{(i)}_{jm})^2} \\ \implies \hat{G}^{(e)}_{jm} &= -\frac{j+1}{t_1}\int_{\hat{0}}^{\hat{t}}\frac{G^{(i)}_{jm}(\mathbf{m};t_1-\hat{\tau})-G^{(i,obs)}_{jm}(\mathbf{m};t_1-\hat{\tau})}{\left[\delta^i_{jm}(t_1-\hat{\tau})\right]^2}d\hat{\tau},\end{aligned} \tag{A.52}$$

the computation of parameter gradients of $\mathbf{B}$ and $G^{(i)}_{jm}(t)$ can be bypassed entirely. Equation (A.51) is the adjoint problem with only external forcing expressed in equation (A.52). The solution of the adjoint problem is then used to compute the misfit gradient, which is expressed as

$$\begin{aligned}D_{\mathbf{m}}\chi^2 = \frac{1}{4\pi a^3}\int_0^{t_1}\int_G \Bigg[&\frac{1}{\mu_0}D_{\mathbf{m}_\alpha}\rho\nabla\times\hat{\mathbf{B}}\cdot\nabla\times\mathbf{B} \\ &+ D_{\mathbf{m}_\beta}\mathbf{v}\cdot\left((\nabla\times\hat{\mathbf{B}})\times\mathbf{B}_C\right)\Bigg]dVdt,\end{aligned} \tag{A.53}$$

where $\nabla\times\hat{\mathbf{B}}\cdot\nabla\times\mathbf{B}$ and $(\nabla\times\hat{\mathbf{B}})\times\mathbf{B}_C$ are, respectively, adjoint sensitivity kernels for electrical resistivity and ocean velocities. These sensitivity kernels are

scaled

$$\mathcal{K}_\rho = \frac{1}{4\pi a^3 \mu_0} \left(\nabla \times \hat{\mathbf{B}}(\mathbf{r}, \hat{t})\right) \cdot \left(\nabla \times \mathbf{B}(\mathbf{r}, t)\right), \tag{A.54}$$

$$\mathcal{K}_\mathbf{v} = \frac{1}{4\pi a^3} \left(\nabla \times \hat{\mathbf{B}}(\mathbf{r}, \hat{t})\right) \times \mathbf{B}_C(\mathbf{r}, t), \tag{A.55}$$

and thus, we arrive at the final form of misfit gradient

$$D_\mathbf{m}\chi^2(\mathbf{m}) = \int_0^{t_1} \int_G [D_{\mathbf{m}_\alpha}\rho \; \mathcal{K}_\rho + (D_{\mathbf{m}_\beta}\mathbf{v}) \cdot \mathcal{K}_\mathbf{v}] dV dt. \tag{A.56}$$